NASA Contractor Report 182135

Development of a 75-Watt 60-GHz Traveling-Wave Tube for Intersatellite Communications

A. L. Rousseau, I. Tammaru, and J. P. Vaszari
Electron Dynamics Division
Hughes Aircraft Company
Torrance, CA 90509-2999

September 1988

Prepared for
Lewis Research Center
Under Contract NAS3-23351

National Aeronautics and
Space Administration

Lewis Research Center
Cleveland, Ohio 44135
AC 216 433-4000

TABLE OF CONTENTS

LIST OF ILLUSTRATIONS

LIST OF ILLUSTRATIONS (CONTINUED)

LIST OF ILLUSTRATIONS (CONTINUED)

LIST OF ILLUSTRATIONS (CONTINUED)

1.0 SUMMARY

This program covers the initial design and development of a 75 watt, 60 GHz traveling-wave tube for intersatellite communications to meet the requirements of NAS3-23351. The objective frequency band was 59 to 64 GHz, with a minimum tube gain of 35 dB. The objective overall efficiency at saturation was 40 percent.

The tube, designated the 961H, used a coupled-cavity interaction circuit with periodic permanent magnet beam focusing to minimize the weight. For efficiency enhancement, it incorporated a four-stage depressed collector capable of radiation cooling in space. The electron gun had a low-temperature (type-M) cathode and an isolated anode.

Two tubes were built and tested; one feasibility model with a single-stage collector and one experimental model that incorporated the multistage collector. The RF performance of these tubes was in basic agreement with the electrical design calculations, which demonstrated that a V-band tube using a coupled-cavity interaction circuit could be built at this peak power level with broad bandwidth.

There was a problem with an oscillation at the upper cutoff frequency of the slot mode, which prevented operation at the design cathode voltage. On future tubes, the circuit coupling slot should be modified to shift the frequency at the slot mode to a range where it cannot interact at the desired operating voltage.

The multistage depressed collector functioned fairly well. However, it was not fully characterized because the circuit was damaged in test before the evaluation was completed. Some modifications to the collector electrode configurations and the use of electrode material with low secondary emission yield should be considered in the future.

2.0 INTRODUCTION

The purpose of the contract effort described in this report was to design, build, and test a high power, millimeter-wave, traveling-wave tube in accordance with the requirements of NAS3-23351 for a 75 watt CW, V-band, intersatellite space communication tube. The principal objective specifications and nominal operating parameters are summarized in Table I.

These objectives of high output power and broad bandwidth constitute a considerable development challenge for a tube in this frequency range. To meet these goals, a coupled-cavity slow-wave structure was chosen because of its thermal ruggedness and demonstrated capability to achieve the required power, bandwidth, and efficiency.

To achieve the overall efficiency of 40 percent, a velocity taper at the output of the RF circuit is used to enhance the beam-circuit interaction in conjunction with a four-stage depressed collector to recover energy from the spent beam.

The electron beam is generated by a convergent flow electron gun designed to operate at approximately 20 kV. It has an isolated anode capable of switching the beam on and off and providing an ion trap. It uses a low-temperature, type M, impregnated cathode operating at a current density of 2.0 amperes per square centimeter to satisfy the long life requirement.

Beam focusing is accomplished with a periodic permanent magnet focusing structure using samarium cobalt magnets and an integrally brazed pole piece assembly.

In the course of the program, two tubes were built and tested; a feasibility model with a single-stage collector and an experimental model with the same electrical design that incorporated the multistage depressed collector (MDC).

TABLE I

OBJECTIVE TWT SPECIFICATIONS

RF Characteristics	
Power Output at Saturation	75 watts
Frequency	59 to 64 GHz
Gain at Saturation	35 dB (minimum)
Duty Cycle	CW
Overall Efficiency	40% at saturation
Electrical Characteristics	
Cathode Voltage	-20 kV (maximum)
Cathode Current	0.070 A
Body Voltage	Ground
Body Current	0.003 A
Collector Voltages	5 stages (maximum)
Anode Voltage	+200 V
Anode Current	0.001 A
Filament Voltage	6.5 V nominal
Filament Current	0.5 A nominal
Ion-Pump Voltage	3.0 ±0.3 kV
Ion-Pump Current	<10 μA
Mechanical Characteristics	
Focusing	Periodic Permanent Magnets
Cooling	Conduction and radiation cooled collector
Weight	15 pounds

The experimental TWT was packaged for conduction cooling the tube body and radiation cooling the MDC. Test results on the two TWTs were very encouraging, in that they demonstrated the feasibility of a 75 watt, broad bandwidth space TWT at V-band. Saturated power output of 75 watts was demonstrated over 5.0 GHz bandwidth, and beam focusing capability of 97 percent without RF and 96 percent with saturated RF verified the viability of a high reliability space TWT design. In addition, an overall efficiency of greater than 30 percent was achieved.

A photograph of the final packaged experimental TWT with radiation cooled MDC is shown in Figure 1.

The following sections describe the parameter trade-offs, design details, and performance results of the 961H traveling-wave tube.

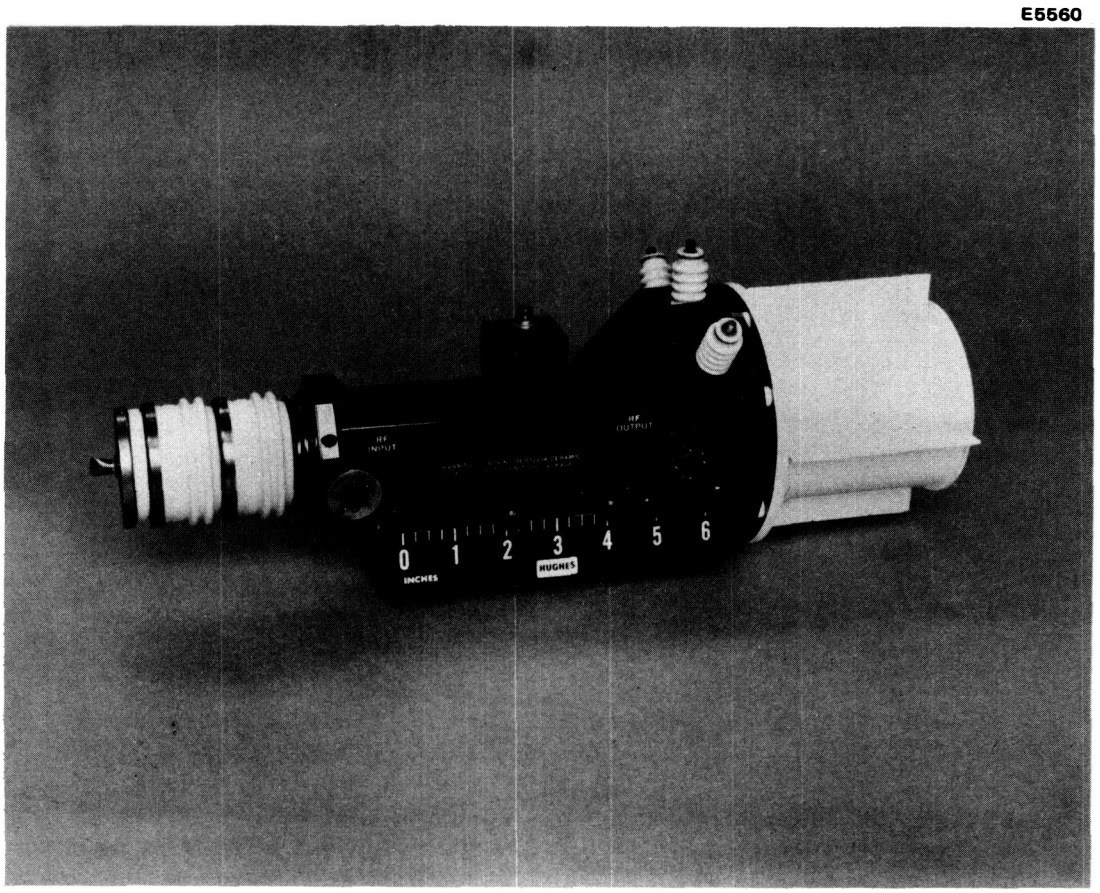

Figure 1 The packaged 961H experimental model.

3.0 TWT DESIGN

3.1 ELECTRICAL DESIGN

Since high efficiency tube performance was a major objective, the beam parameters and circuit characteristics were selected to achieve a high basic interaction efficiency. For the present wideband design, a basic efficiency of approximately 6 percent was anticipated. To raise the overall efficiency to 40 percent, a very efficient multistage collector was clearly required, as well as excellent beam focusing.

The design approach included using: (1) the maximum magnetic field available with samarium cobalt magnets in a PPM structure, to achieve high interaction impedance with a small beam hole (but compatible with good beam focusing); (2) a two-step phase velocity taper at the end of the output circuit section for enhanced conversion efficiency of beam power to RF output power; and (3) a four-stage depressed collector for efficient recovery of the kinetic power in the spent electron beam.

3.1.1 Parameters of the Focused Electron Beam

Good focusing of an electron beam requires adequate field strength, for sufficient confinement force. In PPM focusing, there is also a limitation on the length of the magnetic field period, for beam focusing stability. Greater magnetic field can be obtained with a longer period, but the period is constrained for stability; therefore, the optimum design is determined by the relationship between the obtainable field and the period.

To produce a high focusing field, a small hole size in the iron pole pieces is desired. In the present device, with the focusing structure entirely external to the RF circuit, a preliminary pole piece hole of 0.533 cm (0.210 inches) and a somewhat larger magnet hole size were selected. The resulting available rms magnetic field is plotted in Figure 2 as a function of the period of

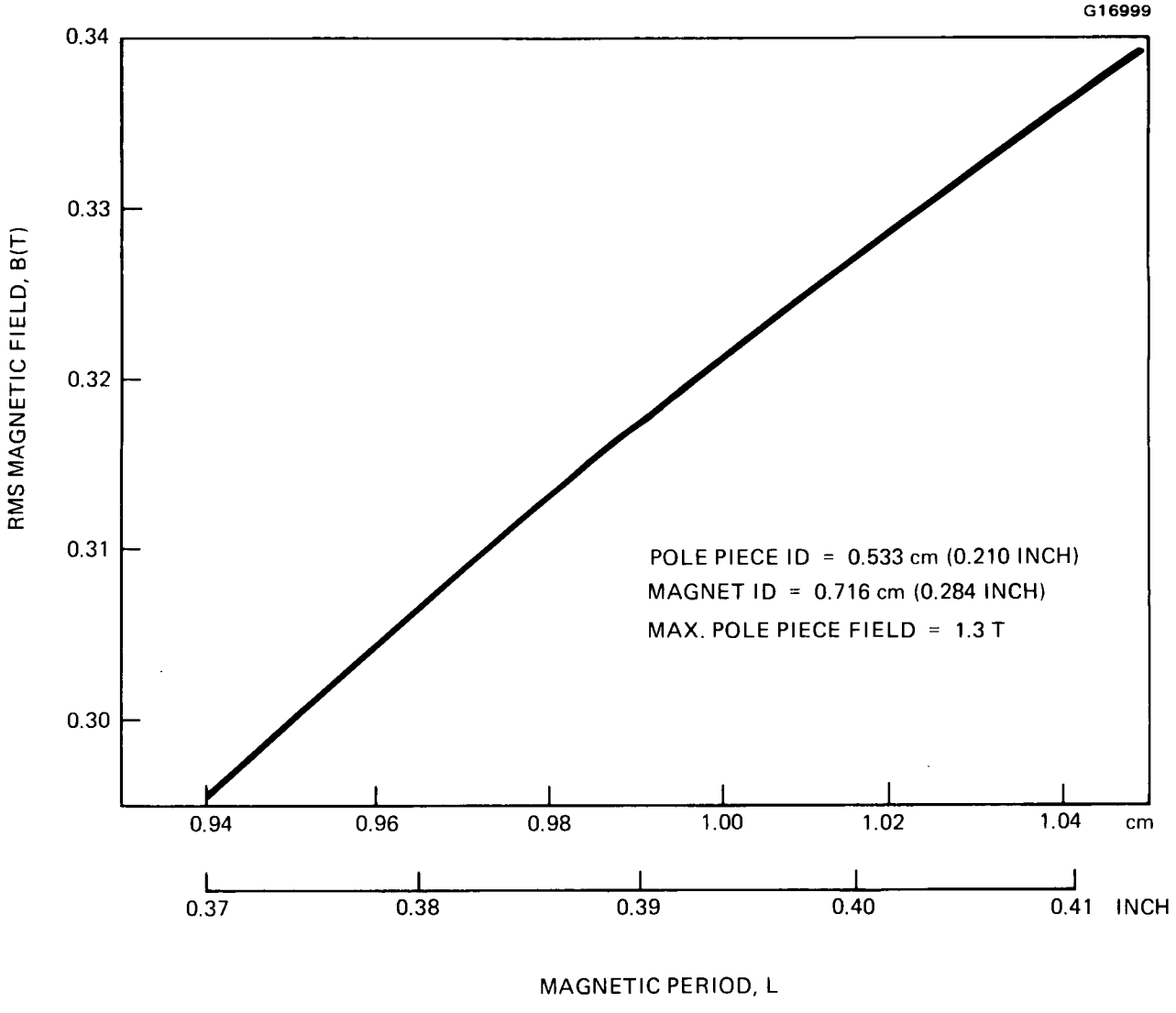

Figure 2 Magnetic field versus magnetic period in a PPM stack with samarium cobalt magnets.

the PPM structure, using samarium cobalt magnets. The following conditions were assumed:

1. The maximum field in the pole piece was 1.3 Tesla.

2. The gap-to-period ratio was approximately one-third for maximum rms field. This ratio also results in an essentially pure sinusoidal field variation along the axis, so that the peak and rms fields are related by $\sqrt{2}$. In the initial design configuration, the ferrules on the pole pieces were so short that eliminating them altogether had little effect. For simplicity, the final design had ferruleless pole pieces.

3. The pole pieces were smaller than the magnets ("undercut") by 15 percent. The undercutting enhances the field on the axis by reducing the flux leakage at the pole piece outer rim.

The small circuit dimensions at 60 GHz require a small diameter, low perveance electron beam. Such a beam is accurately described by the Herrmann optical theory,[1] which includes thermal velocity effects. Transverse thermal velocity components are produced at electron emission from the hot cathode and enhanced by beam compression.

In the Herrmann theory, the magnetic field, B, required to focus an electron beam carrying a current I_o and traveling with an axial velocity u_o is given by

$$B^2 = B_b^2 + \frac{8kT_c}{m\eta^2}\left(\frac{r_c^2}{r_o^4}\right) + \left(\frac{B_c r_c^2}{r_o^2}\right)^2 \qquad (1)$$

where

$$B_b^2 = \frac{2I_o}{\pi\varepsilon_o \eta u_o} \left(\frac{1}{r_o^2}\right)$$

$$\eta = \frac{e}{m}$$

Here e and m are the electronic charge and mass respectively, ε_o is the permittivity of free space, and k is the Boltzmann constant. The beam size is described in terms of a certain statistical rms beam radius r_o defined by Herrmann. Specifically,

$$r_o^2 = r_e^2 + 2\sigma^2$$

where r_e is the radial position of an electron emitted from the edge of the cathode with no transverse velocity, and σ is the radial position of an electron emitted from the center of the cathode with a thermal transverse velocity of $\sqrt{kT_c/m}$.

The beam starting conditions are specified by the cathode temperature T_c (in degrees Kelvin), the cathode (disk) radius r_c, and the axial field at the cathode, B_c. For a PPM system the field magnitude B in Eq. (1) is to be identified with the root-mean-square value.

It is seen that the required focusing field goes up with increased cathode size, increased cathode flux, and higher cathode temperature (as well as with reduced beam size).

In a PPM focusing field, the dynamical stability of the electron beam involves the relation between the oscillation wavelength of the radial motion in the beam and the period of the magnetic field. With a highly thermal low perveance beam, an appropriate oscillation wavelength is that associated with the small-amplitude ripple in r_o given by the angular frequency[1]

$$\omega_R = \omega_c \sqrt{1 - \tfrac{1}{2}(B_b/B)^2} \qquad (2)$$

where

$\omega_c = \eta B$ = the cyclotron frequency.

The scallop wavelength is therefore

$$\lambda_s = \frac{u_o}{(\omega_R/2\pi)} = \frac{2\pi u_o}{\eta B\sqrt{1 - \tfrac{1}{2}(B_b/B)^2}} \qquad (3)$$

If λ_s is large in relation to the magnetic field period L, the beam will effectively experience an average constant focusing field of magnitude B. As λ_s becomes more comparable to L, the electron motion is more affected by the local changes in the field.

When λ_s equals L, an unstable beam generally results. To provide good focusing it is therefore necessary to ensure some minimum value of the ratio λ_s/L. Based on prior experience with low perveance thermal electron beams, this ratio was chosen as 1.1 for the present TWT.

The following conditions summarize the assumptions made in defining the beam design in the Herrmann theory:

1. The cathode loading was chosen at 2 A/cm^2 for long life.

2. With a type M cathode material, the cathode operating temperature, T_c, was approximately 1300^oK.

3. The magnetic field at the cathode, B_c, was zero.

4. The ratio of scallop wavelength to magnetic period, λ_s/L, was taken to be 1.1 minimum for stability, as discussed above.

The last condition, in conjunction with the relation between the obtainable field and the magnetic period (Figure 2), establishes a unique focusing design and beam size, for a given beam with current I_o and voltage V_o.

The selection of beam voltage and current requires an estimate of the basic efficiency of the tube. This is related to the fundamental interaction strength given by the Pierce's growth parameter, C, defined by

$$C = \left(\frac{K\ I_o}{4\ V_o} \right)^{1/3}$$

where K is the interaction impedance. The interaction impedance, in turn, depends on the design voltage V_o and the beam hole diameter, 2a, expressed in normalized form through the radial propagation parameter γa.

Although a smaller beam hole gives higher interaction impedance, the beam-to-hole radius ratio was maintained small to ensure excellent beam transmission for effective collector performance. In terms of the theoretical diameter that would transmit 99.5 percent of the focused dc beam, $2r_{99.5}$, the beam filling factor was chosen as

$$r_{99.5}/a \approx 0.85$$

Equivalently, in terms of the radius that contains 95 percent of the current, r_{95}, and the Herrmann radius r_0, the beam filling factors are

$$r_{95}/a \approx 0.64$$
$$r_0/a \approx 0.37$$

The final choice of voltage and current was based on an iterative process. An upper voltage limit of 20 kV was imposed by the specification. This value was generally in the optimum range for high interaction strength. A nominal value of 19.7 kV was therefore selected. The current (and beam hole) were then adjusted until the required output power was obtained by large signal calculations. This process involved the circuit design, which is described further in the next section.

Table II summarizes the final beam design parameters based on the assumptions described. A magnetic field of 0.307 tesla rms was used. It was obtained with a magnetic field period of 0.976 cm (0.384 inch). The dimensions of the final magnetic stack are detailed in Figure 3. The pole piece size is slightly larger than in Figure 2.

Figure 18 in Section 3.1.3 shows the variation of the statistical radii in the optical model as a function of the distance from the cathode, in a PPM design where the r_o radius is fairly flat.

3.1.2 Circuit Design

With high efficiency a primary objective, a conventional cylindrical cavity configuration with reentrant ferrules was the preferred choice because of its high interaction impedance. Furthermore, this approach had low risk, since this type of circuit had been successfully used in several MMW TWTs at Hughes, up to 95 GHz.

A second special requirement for the tube was wideband performance. The ultimate objective was operation over the frequency range from 59 to 64 GHz. This requirement of 5.0 GHz bandwidth with high efficiency was challenging for a V-band TWT. Thus, a two-tube approach, with one tube covering the range 59 to 61.5 GHz and the second tube covering 61.5 to 64 GHz, was considered for the feasibility demonstration.

The design bandwidth was limited by the need for tube stability when no extra loss was added to the circuit to prevent oscillation at the cavity resonance frequency. As the passband is increased to achieve broadband performance, the phase velocity at the upper cutoff (the cavity resonance frequency) approaches the electron velocity, until at some point the tube becomes unstable. To ensure an adequate margin of stability, a cold bandwidth of approximately 35 percent was selected on the basis of prior experience with other MMW TWTs.

The circuit was further designed with a phase shift per cavity at midband of at least 1.45 radians. This value is somewhat higher than typically used in

TABLE II
BEAM DESIGN PARAMETERS

Cathode Voltage, V_k	19.7 kV, nominal
Cathode Current, I_k	70 mA
Beam Perveance, P	0.0253×10^{-6} A/V$^{3/2}$
Cathode Diameter, $2r_c$	0.1057 cm (0.0416 inch)
Cathode Temperature, T_c	1300 K
Focusing Field, B_o	0.307 T, rms
Field at Cathode, B_c	0
Beam Diameter, $2r_o$	0.0198 cm (0.0078 inch)
Area Compression, $(r_c/r_{95})^2$	38
Magnetic Period, L	0.975 cm (0.384 inch)
Scallop Wavelength, λ_s	1.083 cm (0.426 inch)
Stability Parameter, λ_s/L	1.11

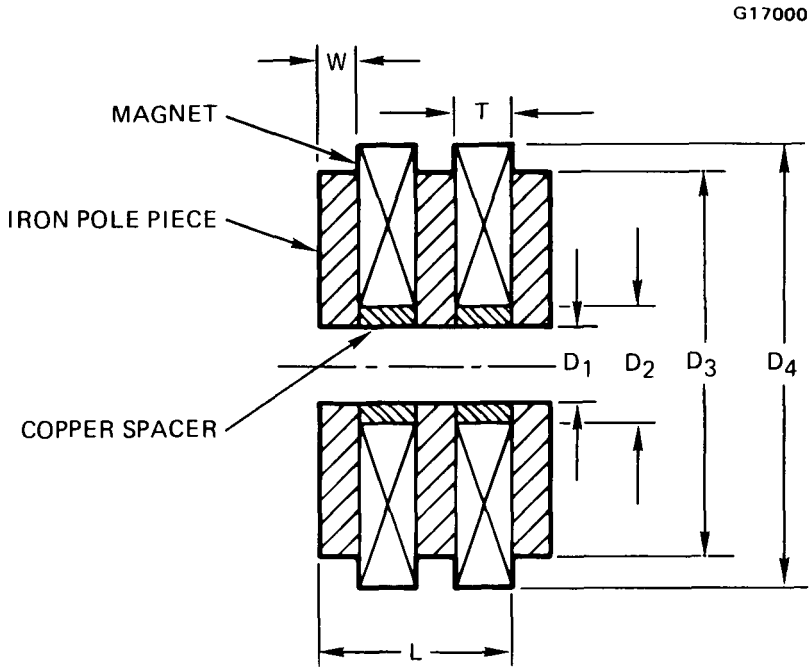

POLE PIECE ID, D_1	0.541 cm (0.213 INCH)
MAGNET ID, D_2	0.714 cm (0.281 INCH)
POLE PIECE, OD, D_3	2.700 cm (1.063 INCH)
MAGNET OD, D_4	3.175 cm (1.250 INCH)
POLE PIECE THICKNESS, W	0.178 cm (0.070 INCH)
MAGNET THICKNESS, T	0.310 cm (0.122 INCH)
MAGNETIC PERIOD, L	0.976 cm (0.384 INCH)

Figure 3 Dimensions of PPM focusing array.

high-efficiency TWTs (for high impedance), but it has the advantage of less phase velocity dispersion for improved bandwidth performance.

The design precedure was an iterative process. Given a value for the beam current, with a cathode voltage of 19.7 kV, the beam hole size was determined from the available focusing field, as described in Section 3.1.1. The assumed cold bandwidth and phase shift per cavity then allowed a calculation of the tube performance, both at small-signal and large-signal operation. The design parameters were modified until the best overall RF performance was obtained. Although the specified gain at saturation was 35 dB minimum, the circuit was designed for a gain of 50 dB to permit convenient testing with commercially available RF sources at V band.

Initially, a beam current of 60 mA was assumed in a beam hole with a diameter of 0.0533 cm (0.021 inches). This hole size corresponded to a radial propagation parameter γa of 1.25 at midband. For a uniform three-section circuit centered at 61.5 GHz with a phase shift of 1.45π, the small signal gain variation was close to 10 dB over a 4.0 GHz bandwidth. Although a two-step velocity taper gave adequate output power of 84 W at midband, a 5.0 GHz bandwidth could not be achieved with this design. A brief investigation of a circuit with the phase shift increased to 1.5π, which had lower gain per cavity and efficiency due to smaller interaction impedance, showed no promise of improved bandwidth.

The major effort was then concentrated on optimizing the performance over a 3 GHz band. Several velocity taper combinations were evaluated. The beam current was also increased, first to 65 mA with a beam hole diameter of 0.0546 cm (0.0215 inches) and then to 70 mA with a beam hole of 0.0549 cm (0.022 inches). Finally, the center frequency was raised to 62.75 GHz (the midband of the upper half of the total 59 to 64 GHz range), retaining a phase shift value of 1.45π radians per cavity.

Table III lists the basic interaction parameters of the final design. The calculated performance of the best design is displayed in Figures 4 and 5. Curves of output power versus RF drive power are plotted in Figure 4 for several frequencies covering a 5.0 GHz range centered at 62.75 GHz, while

TABLE III
CAVITY AND RF INTERACTION PARAMETERS

Cathode Voltage, V_k	19.7 kV nominal
Cathode Current, I_k	70 mA
Beam Perveance, P	0.025×10^{-6} A/$V^{3/2}$
Center Frequency, fo	62.75 GHz
Cold Bandwidth, B_c	35 %
Cavity Period, L_c	0.0922 cm (0.0363 inch)
Beam Hole Diameter, 2a	0.0559 cm (0.0220 inch)
Beam Filling Factor, r_o/a	0.36
At Center Frequency:	
Phase Shift/Cavity, βL_c	1.45 π radians
Pierce Impedance, K	8.18 ohm
Radial Parameter, γa	1.33
Loss/Cavity, L_{cav}	0.037 dB

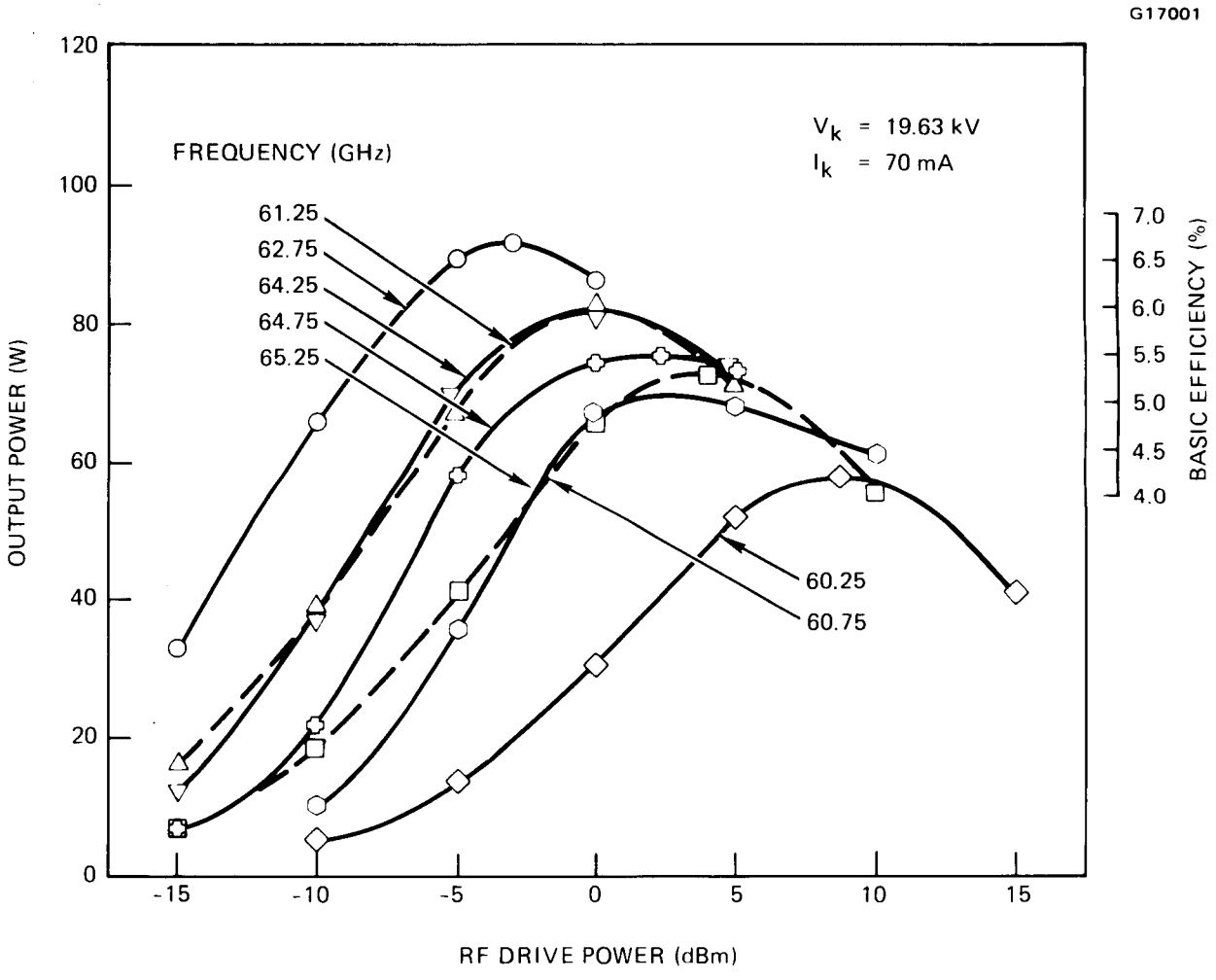

Figure 4 Calculated output power versus RF drive at several frequencies over a 5 GHz band centered at 62.75 GHz.

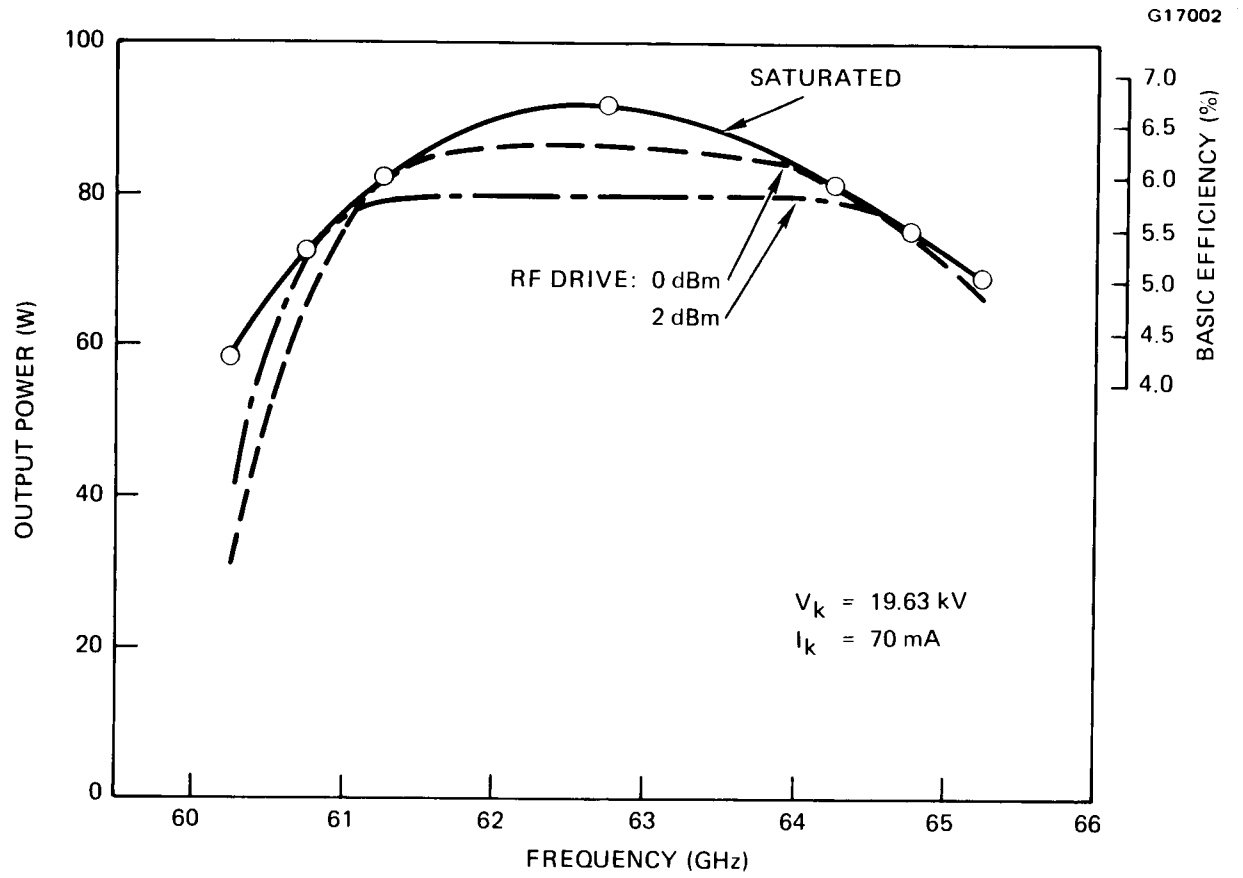

(a)

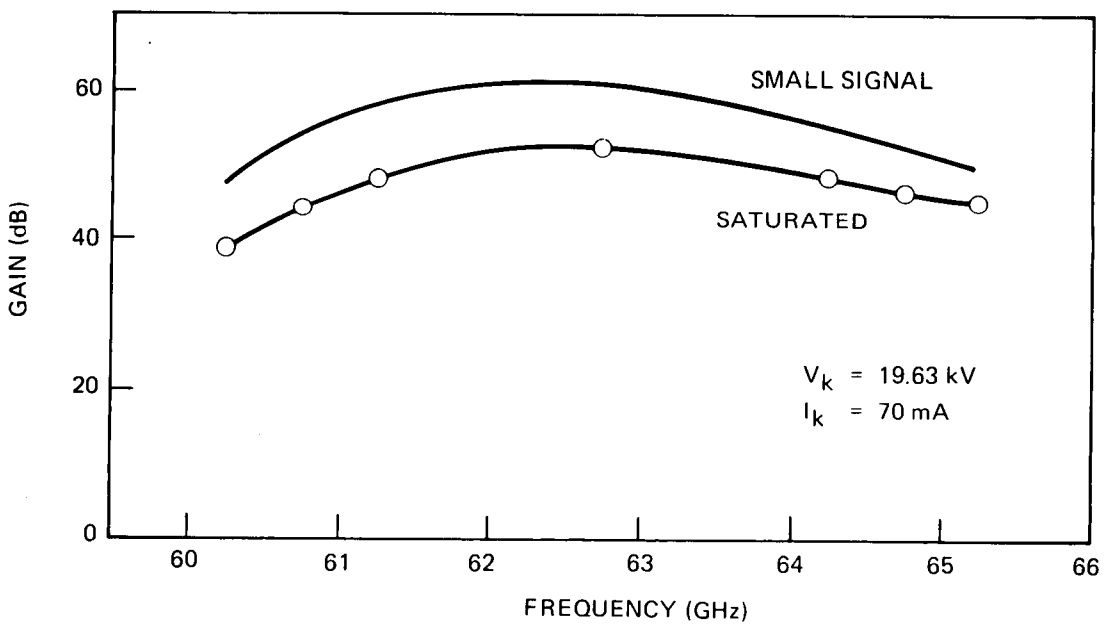

(b)

Figure 5 Calculated output power, and saturated and small signal gain versus frequency.

the saturated output power versus frequency is shown in Figure 5a. The output power at two fixed drive levels has also been plotted. An expected power loss of 0.2 dB in the output coupler and window has been included. A minimum of 75 W is obtained over approximately 3.5 GHz at a basic efficiency of 5.5 percent, while the peak output power is 92 W corresponding to 6.7 percent efficiency. Figure 5b exhibits the saturated and small-signal gain over a 5.0 GHz range. The RF circuit had a total of 169 cavities, including couplers and termination cavities, distributed over three sections. Toward the end of the output section, the phase velocity (cavity period) was reduced in two steps to 98 and 96 percent of the original value.

Figure 6 shows the frequency-versus-phase (ω-β) characteristics of the final V-band circuit. It was actually measured with scaled cavity parts at X-band. The required cavity configuration was determined by iteratively adjusting the coupling hole angle and cavity gap in the X-band parts. The final cold bandwidth was 34.9 percent. Over the operating frequency range, the ω-β curve was essentially indistinguishable from the one assumed in the design analysis. Figure 7 shows the variation of Pierce's interaction impedance, phase shift per cavity, and phase velocity with frequency. The experimental impedance data were consistent with the values used in the analysis.

Slot mode stability and cavity redesign

The two TWTs that were built and tested both oscillated when operated with a cathode voltage near the design value of -19.7 kV. However, the TWTs were stable at some lower and higher values. The RF circuits of the tubes were of identical design, although the output section of the first TWT had a bad mismatch.

Both tubes also exhibited an anomalous power hole at about 65 GHz. Figure 8 shows the RF performance of the second TWT at two values of the cathode voltage, 19.3 kV and 20.3 kV. At the lower operating voltage, the performance has shifted up in frequency (to a center frequency of 66 GHz),

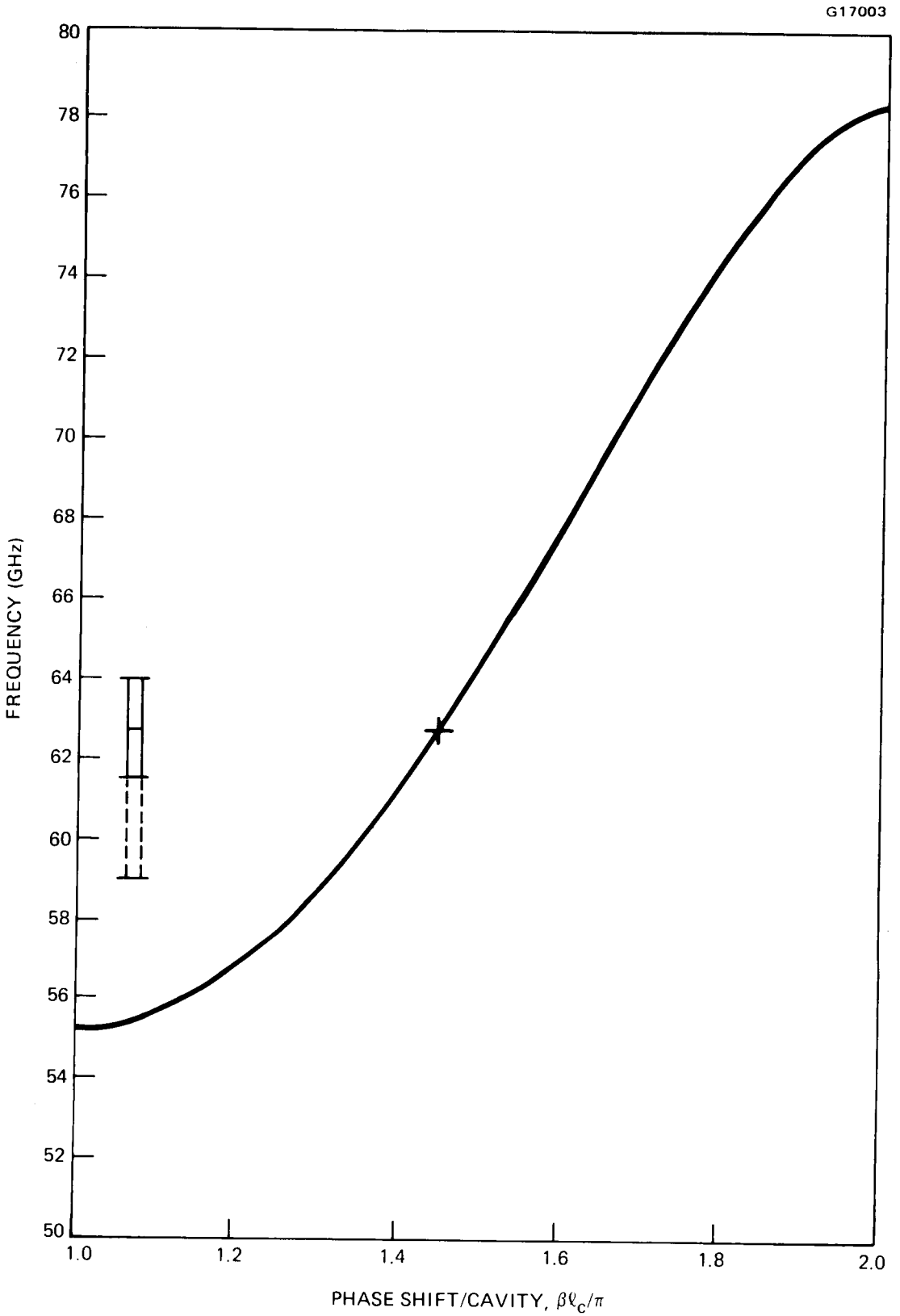

Figure 6 The ω-β curve of the 961H, designed to operate over the upper half of the total 59 to 64 GHz range.

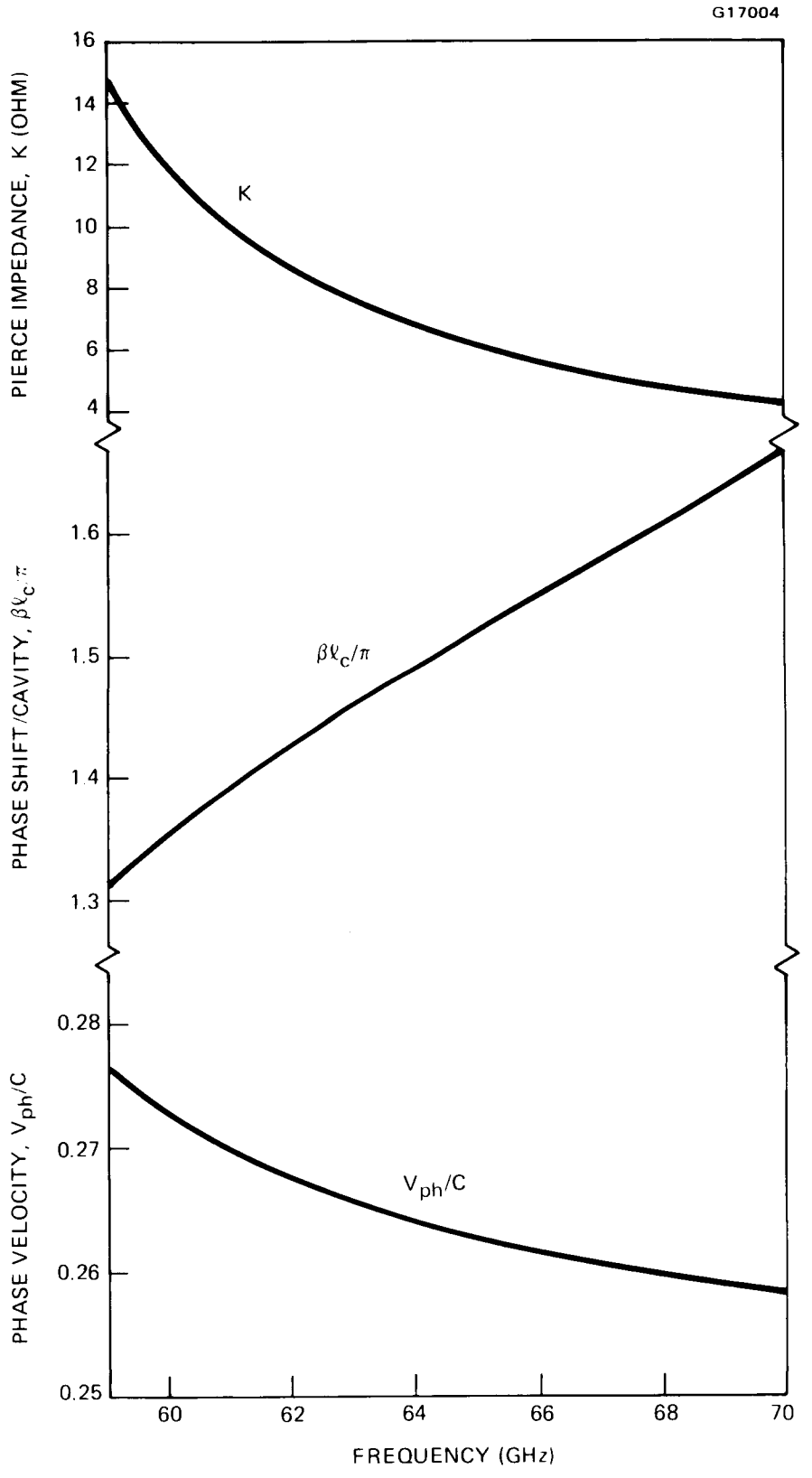

Figure 7 Pierce impedance, phase shift, and phase velocity versus frequency.

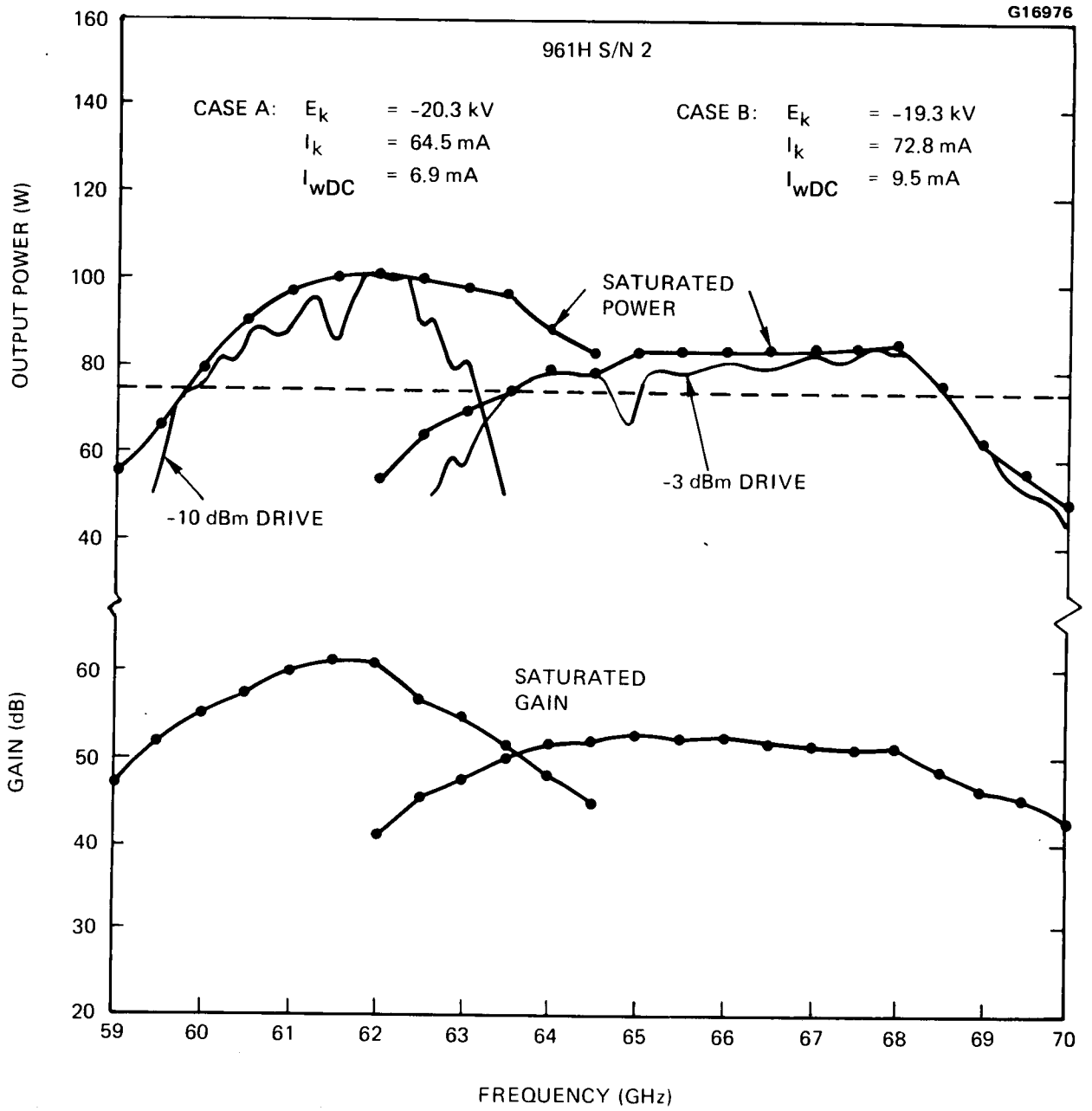

Figure 8 RF performance of 961H S/N 2.

the bandwidth is wider (a full 5 GHz), and the gain and saturated output power are generally less. With constant drive, the power has a sharp dip just below 65 GHz.*

The reason for both the instability and the anomaly at 65 GHz is evident from the frequency-versus-phase (ω-β) curves and line of constant phase velocity ("voltage line") plotted in Figure 9. The upper cutoff of the slot mode, which is a high impedance point, lies almost exactly (and accidentally) on the voltage line passing through the design point, which is indicated by a cross. The design point defines the phase shift per cavity at center frequency. In the 961H, which was intended to operate over the upper half of the total 5.0 GHz band (i.e., the range of 61.5 to 64 GHz), the center design frequency, 62.75 GHz, was placed at a phase shift per caivty of 1.45 π radians.

Hence, at the nominal design voltage of 19.7 kV, the tube oscillated at the upper cutoff of the slot mode (130 GHz). As the voltage was changed away from this value in either direction, the voltage line moved away from the high impedance point until the oscillation could not sustain itself. The tube would then perform normally, except possibly when the cutoff frequency was induced by harmonic interaction, i.e., when the tube was operated at 65 GHz.

The mechanism is the excitation on the electron beam of harmonic current components because of nonlinear effects at large-signal levels. (At low RF drive, the gain curve showed no clear-cut anomalous behavior. See Figure 52 in Section 4.) If an upper passband provides amplification of the harmonic signal component, the beam modulation is changed, disturbing the growth of the signal at the fundamental frequency.

---

*The anomalous behavior is better illustrated in Figures 53, 56, 57 and 58 where the swept output power is plotted for several drive levels. Although a power dip also appears at 61.5 GHz with 20.3 kV cathode voltage, it is of a different nature, as may be seen in Figure 55. Note that in all these figures, the calibration lines drawn in Figure 58 are implicitly understood.

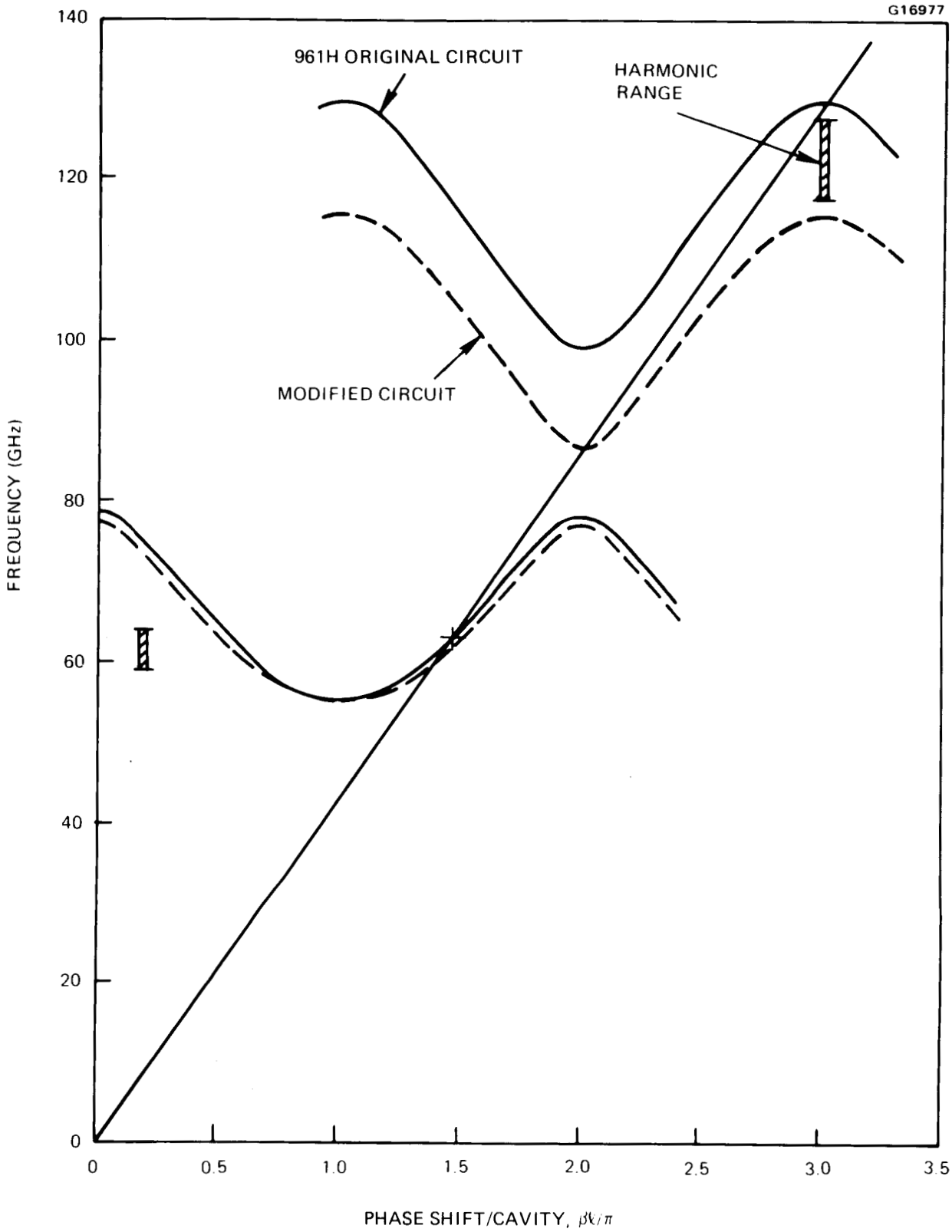

Figure 9 961H passband characteristics.

The cure for both problems is to shift the slot mode down in frequency, such that the entire harmonic operating frequency range is above the upper cutoff. A modified circuit was designed to successfully accomplish the shift. The resulting $\omega-\beta$ characteristics, which were actually measured with scaled X-band parts, are also plotted in Figure 9. The modification consisted principally of narrowing the radial width of the coupling slot and decreasing the slot angle (from 144° to 136°). The V-band dimensions for both circuits are detailed in Figure 10.

On the modified circuit, additional objectives were to shift the center operating frequency back to 61.5 GHz, increase the phase shift to 1.47 π, and raise the operating voltage to 19.7 kV. This required an increase in the cavity period and the cavity diameter. The measured circuit had a phase shift of 1.448π at 61.5 GHz and a somewhat smaller cold bandwidth (33.7 percent compared to the original 34.9 percent). By increasing the coupling hole angle from 136° to 138°, the bandwidth will increase to about 35.0 percent and the phase shift at 61.5 GHz will become approximately 1.47π. The slot mode will also shift down somewhat. The voltage line through the new design point will now be a little lower, crossing the 3π phase shift line at 125.5 GHz. This is still well above the upper cutoff of the slot mode at 115 GHz.

The data demonstrate that the slot mode oscillation can be readily eliminated, even in designs with a larger phase shift per cavity. It is worth noting that oscillation at the lower cutoff of the slot mode will not occur, even if this cutoff happens to be on the voltage line. This is because the interaction impedance at the lower cutoff is zero due to vanishing electric field on the axis.

3.1.3 Electron Gun and Magnetic Entrance Conditions

The model 262B electron gun was designed for use on the 961H traveling-wave tube and integrated into its magnetic focusing system. The focusing system utilizes periodic permanent magnets to produce a sinusoidal, axial field with peak strength of 0.43 tesla, the minimum field strength required. In order to focus with this magnitude of magnetic field, a carefully designed pole piece

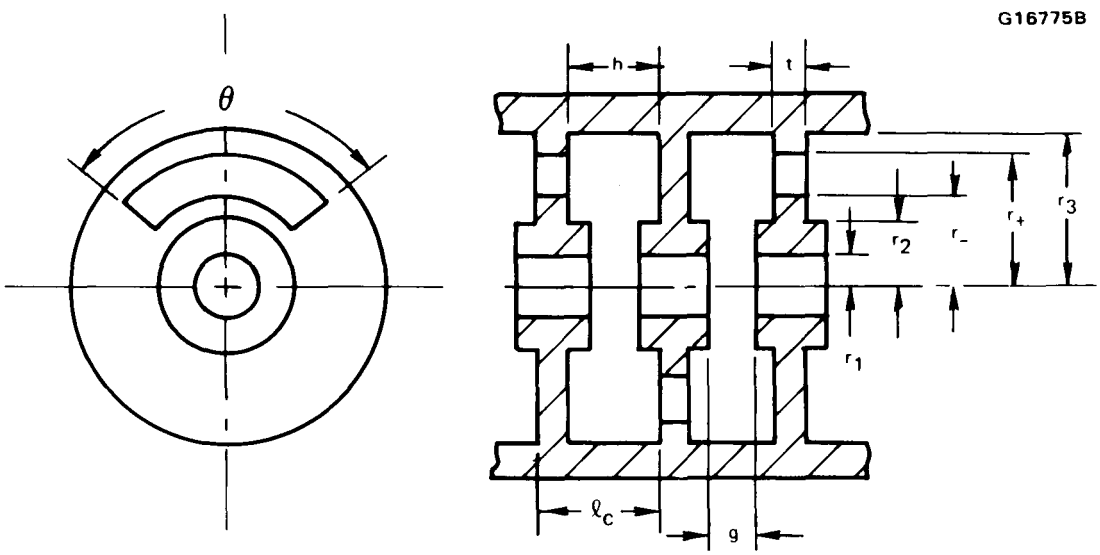

DIMENSION	ORIGINAL DESIGN	MODIFIED DESIGN
$2r_1$ – cm (IN.)	0.0559 (0.0220)	0.0559 (0.0220)
$2r_2$ – cm (IN.)	0.0834 (0.0340)	0.0834 (0.0340)
$2r_3$ – cm (IN.)	0.2134 (0.0840)	0.2205 (0.0868)
$2r_-$ – cm (IN.)	0.1016 (0.0400)	0.1407 (0.0554)
$2r_+$ – cm (IN.)	0.2134 (0.0840)	0.2205 (0.0868)
θ – rad (^{o})	2.513 (144^o)	2.374 (136^o)
ℓ_c – cm (IN.)	0.0922 (0.0363)	0.0950 (0.0374)
h – cm (IN.)	0.0706 (0.0278)	0.0734 (0.0289)
t – cm (IN.)	0.0216 (0.0085)	0.0216 (0.0085)
g – cm (IN.)	0.0290 (0.0114)	0.0300 (0.0118)

Figure 10 Original and modified cavity design.

and magnetic gun shields were employed to optimize the beam launch conditions by minimizing magnetic flux in the cathode region of the gun. Determining the appropriate magnetic field and designing magnetic elements to realize that field proved to be two of the most important tasks of the gun design and gun integration effort.

3.1.3.1 Electron Optics Design - Typically, the electron optics design procedure, which determines appropriate electron gun electrode shapes, is an iterative process in which the ideal electrodes are synthesized, analyzed, and refined to give practical shapes. The electrode synthesis process yields only an approximate starting point for the design. In this instance, the required gun characteristics were quite similar to those of an existing gun. As a result, we used the existing gun as a starting point for the new design rather than synthesizing entirely new electrode shapes.

The fundamental distinguishing performance characteristics of an electron gun are its area compression (for a given accelerating voltage, the ratio of the cathode area to the cross-sectional area of the beam at its electrostatic minimum) and its perveance (the ratio of the beam current to the accelerating voltage raised to the three-halves power). These characteristics of a gun remain unchanged as the size of the gun is scaled to achieve a desired beam size, so it is convenient to catalog guns by these two characteristics.

The 961H tube requires a 0.070 amp, 19.6 kV electron beam confined within a 0.0475 cm diameter so that essentially all beam current is contained within 85 percent of the beam hole diameter. To ensure the long life consistent with this tube's intended application, current density at the cathode of the electron gun is limited to 2 amps/cm^2. These requirements dictate an electron gun having a perveance of 0.0255×10^{-6} $A/V^{3/2}$ and an area compression of 38:1.

Similar electron guns produced at EDD are tabulated in Table IV. Of these guns, model 242B has characteristics most similar to those required for the 961H tube, so this gun was chosen as the basis for the new design, the model 262B electron gun. The 242B electrode shapes were scaled by a factor of 1.2381 to create a preliminary gun design with the desired perveance and area

TABLE IV

SIMILAR ELECTRON GUNS MANUFACTURED AT EDD

Gun Model	Microperveance	Area Compression	Tube
197B	0.037	21:1	284H
223B	0.030	45:1	942H
227B	0.033	18.5:1	914H
229B	0.030	18.5:1	915H
242B	0.0266	24:1	960H

compression and the cathode size needed to meet the 2 A/cm^2 cathode loading constraint dictated by life requirements. This preliminary model was analyzed using the Herrmannsfeldt electron trajectory tracing computer program. The electrode shapes were then modified and reevaluated. This process was repeated until a gun producing a beam of the desired perveance and electrostatic beam size was realized.

For beams of relatively low perveance, the thermal velocities imparted to electrons at the cathode become very important in determining beam size because the space charge forces in the beam are relatively weak. The 262B gun produces a very low perveance beam. As a consequence, thermal velocities must be considered in designing the gun. The Herrmannsfeldt code assumes a nonthermal beam, so compensation for this must be made in the design process. Figure 11 shows the effect of thermal velocities by plotting the theoretical expected beam size for the 262B electron gun as a function of beam voltage as determined from the Herrmann optical theory. The increase in beam size that results from thermals is inversely proportional to the square root of the accelerating voltage, so the beam size for an infinite accelerating voltage is equal to that of a non-thermal beam. The predicted thermal component of beam radius at the operating voltage of 19.6 kV is 0.014 cm. Figure 12 shows a plot of nonthermal beam trajectories for the final 262B electrode configuration, as produced by the Herrmannsfeldt code. The nonthermal beam radius for this design is 0.0084 cm, 0.0013 cm smaller than the design goal of 0.0097 cm. The

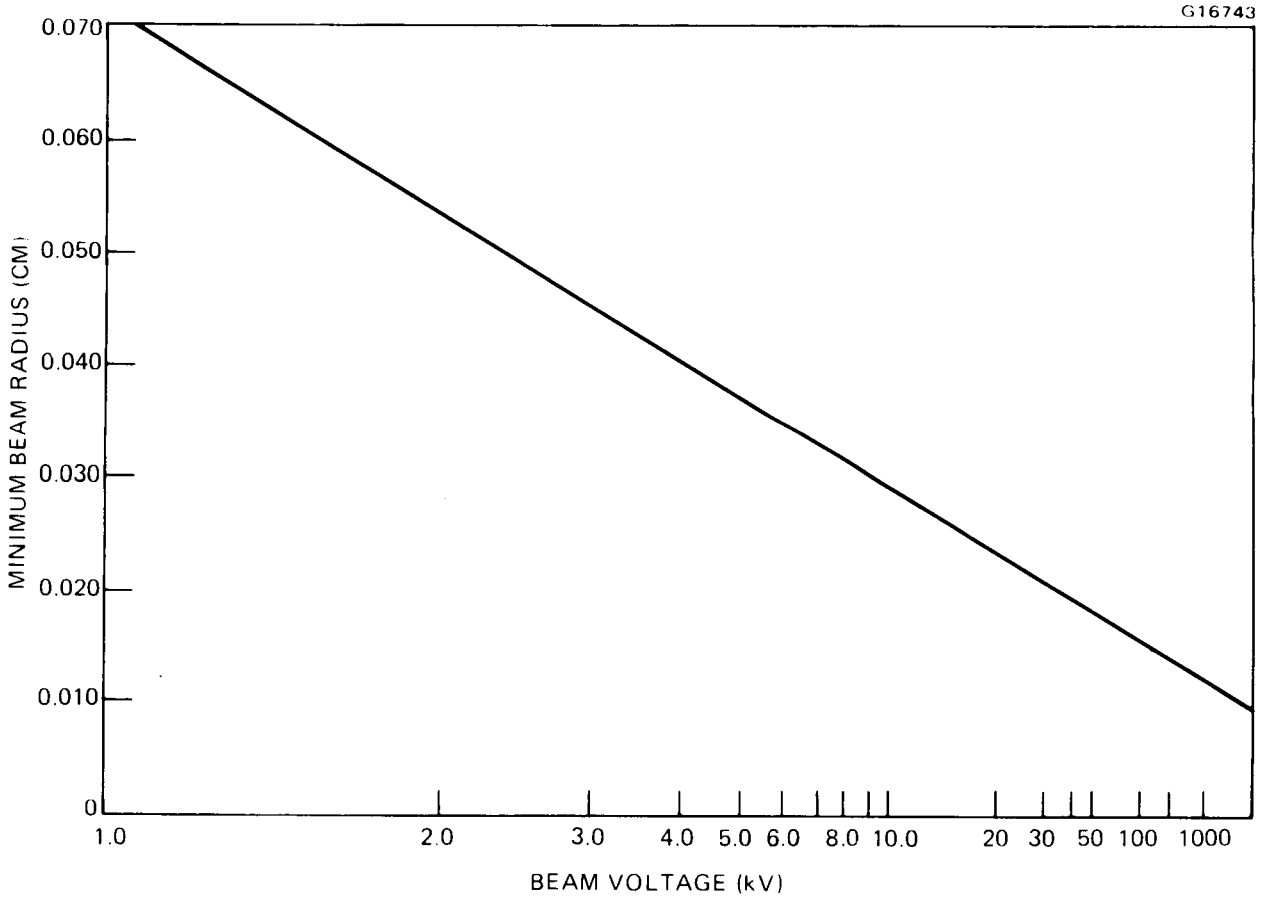

Figure 11 Predicted beam size of 262B electron gun as a function of beam voltage.

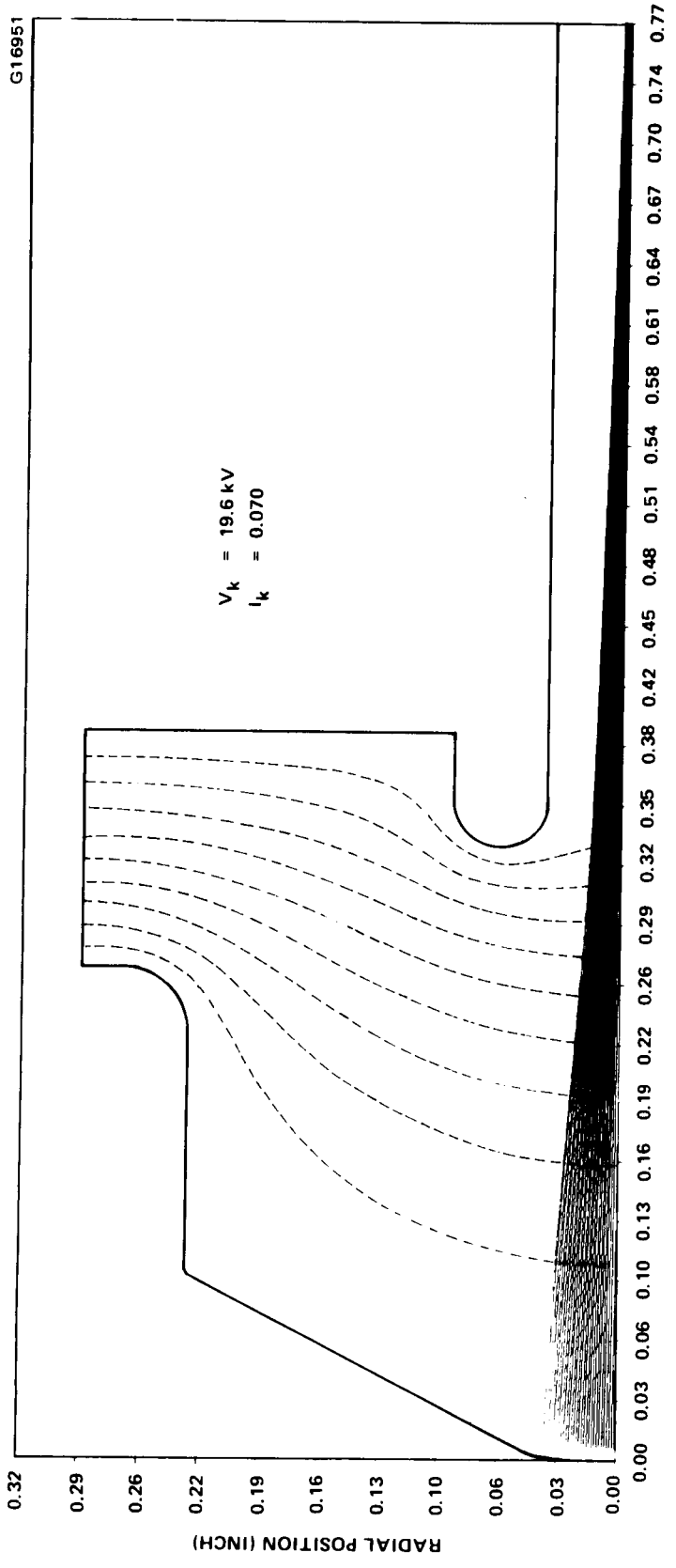

Figure 12 Predicted electrostatic electron trajectories of 262B electron gun.

perveance of this model was correct, however, and we decided to proceed since the 0.013 cm discrepancy was well within the design technique's limits of accuracy.

3.1.3.2 Magnetic Entrance Conditions - The magnitude of magnetic field required to focus an electron beam is a function of the accelerating voltage, the beam current density, the transverse velocity content in the beam, and the magnetic flux threading the cathode. The accelerating voltage and beam current are fixed by the tube requirements, and the transverse velocity content of the beam is minimized using the coolest cathode available and paying close attention to beam quality. When the cathode flux is zero, the beam is said to be Brillouin focused and the focusing field strength required is minimized.

The field strength available for the 961H tube was limited by practical considerations to 0.435 tesla, which was the field required to achieve Brillouin focusing. As a consequence, it was extremely important to minimize flux on the cathode. Measurements of representative magnetic circuits were made to determine what magnetic structure was necessary to minimize the cathode flux.

Initially, we had hoped that the gun pole piece alone would serve to shield the cathode from the focusing field and a number of pole piece configurations were measured. Figure 13 shows the critical dimensions of a pole piece, and Figure 14 shows the magnetic field measured with one of the pole piece designs. The flux in the region of the cathode was on the order of 0.004 tesla or more for these configurations. The most effective method for reducing the cathode flux when a pole piece was used alone was to increase the outside diameter of the pole piece which became much larger than desirable.

To more effectively shield the cathode, the anode and its support cylinder were made of iron. This configuration was tested and the magnetic field was reduced to a near zero level at the cathode, but a large peak occurred just inside the gun. A cylindrical magnetic shield was then added to the pole piece, as shown schematically in Figure 15, which reduced this peak. Figure 16 shows the measured field for the final design. The field build-up with the gun is shown in Figure 17.

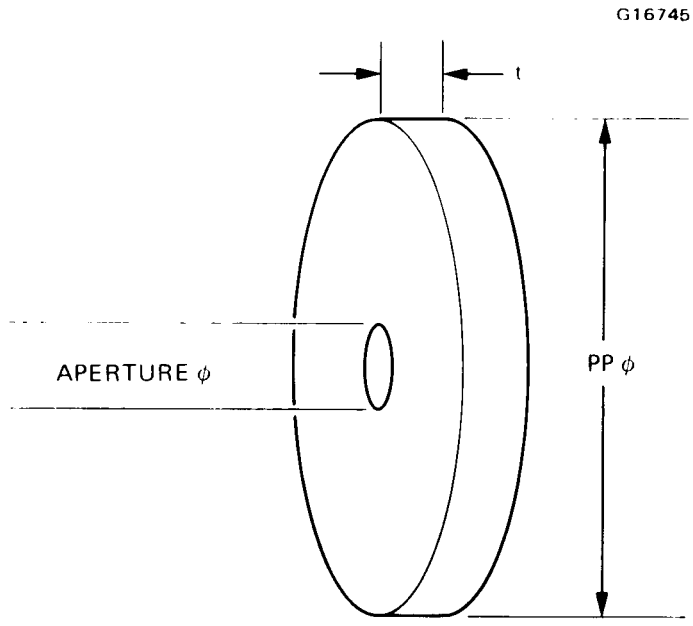

Figure 13 Critical dimensions of pole piece.

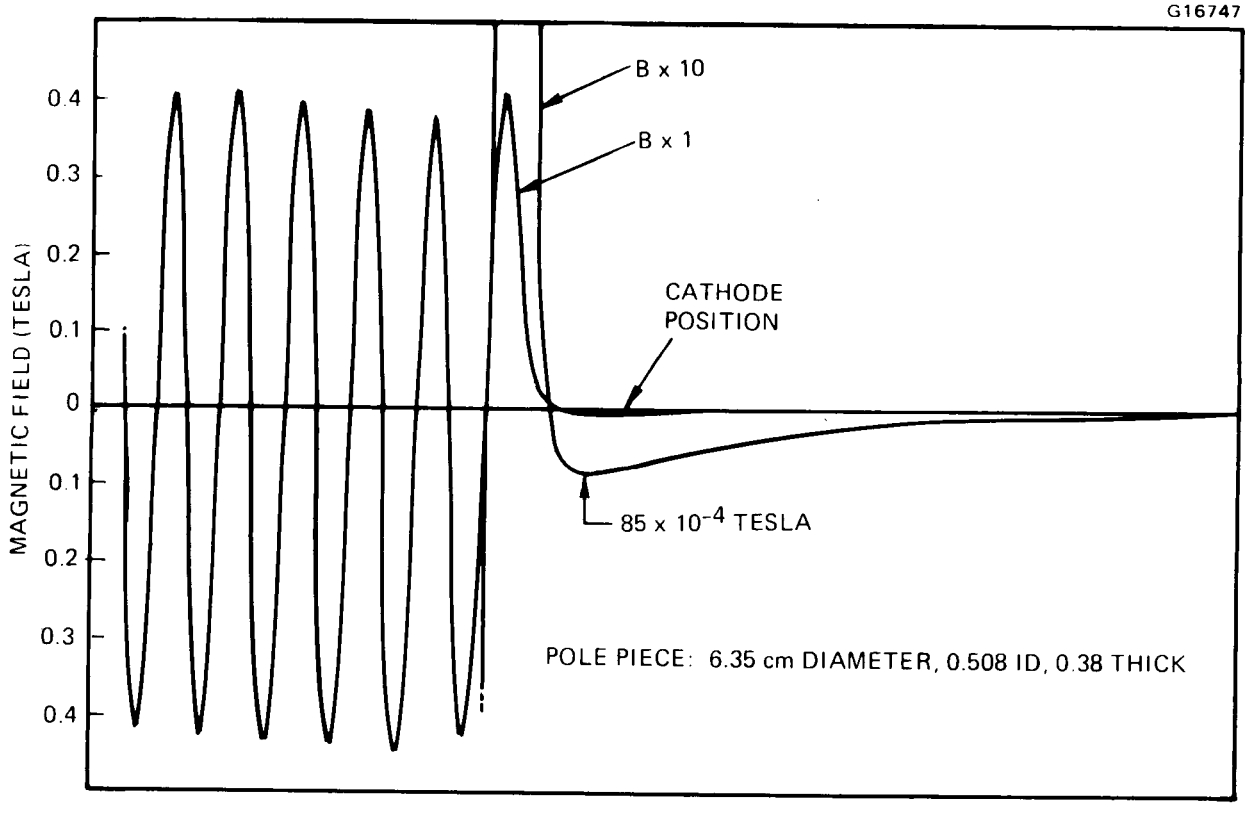

Figure 14 Magnetic field along the axis and in the gun area of the 961H tube.

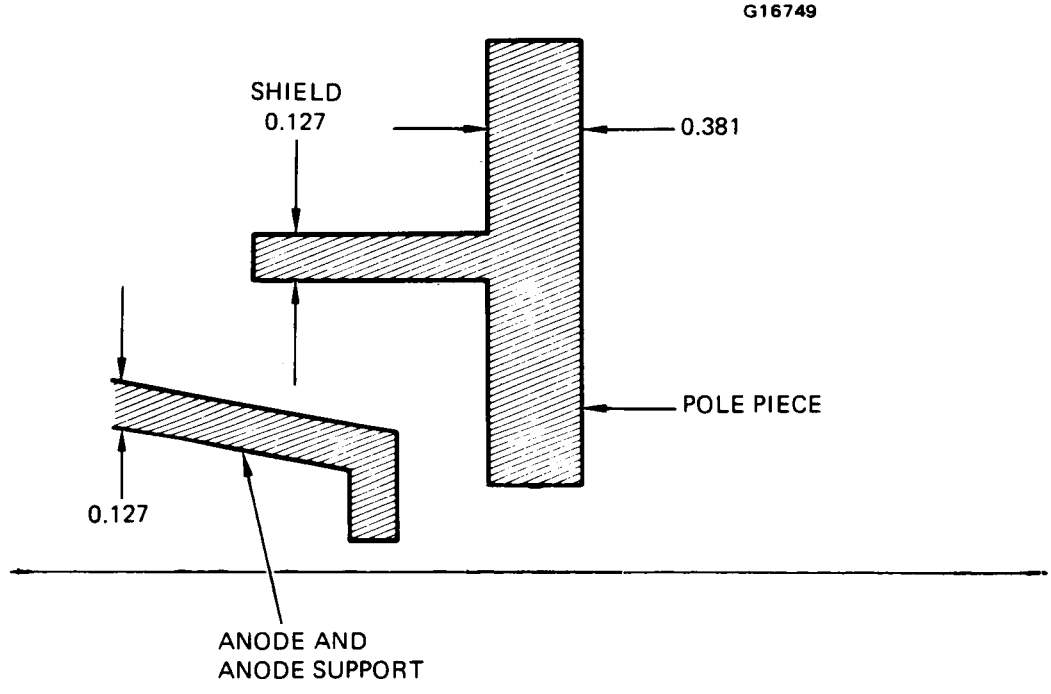

Figure 15 Electron gun magnetic flux shields.

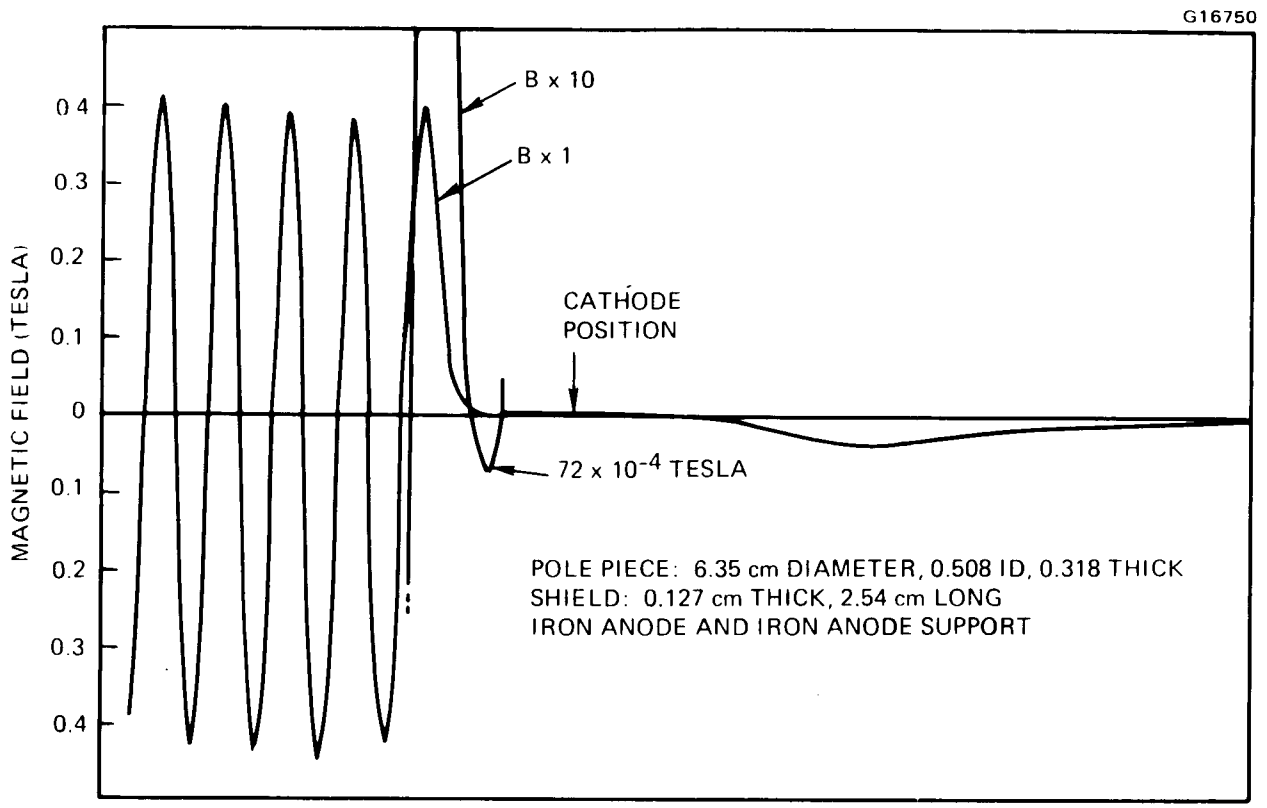

Figure 16 Measured magnetic field with shield and an iron anode and iron anode support cylinder.

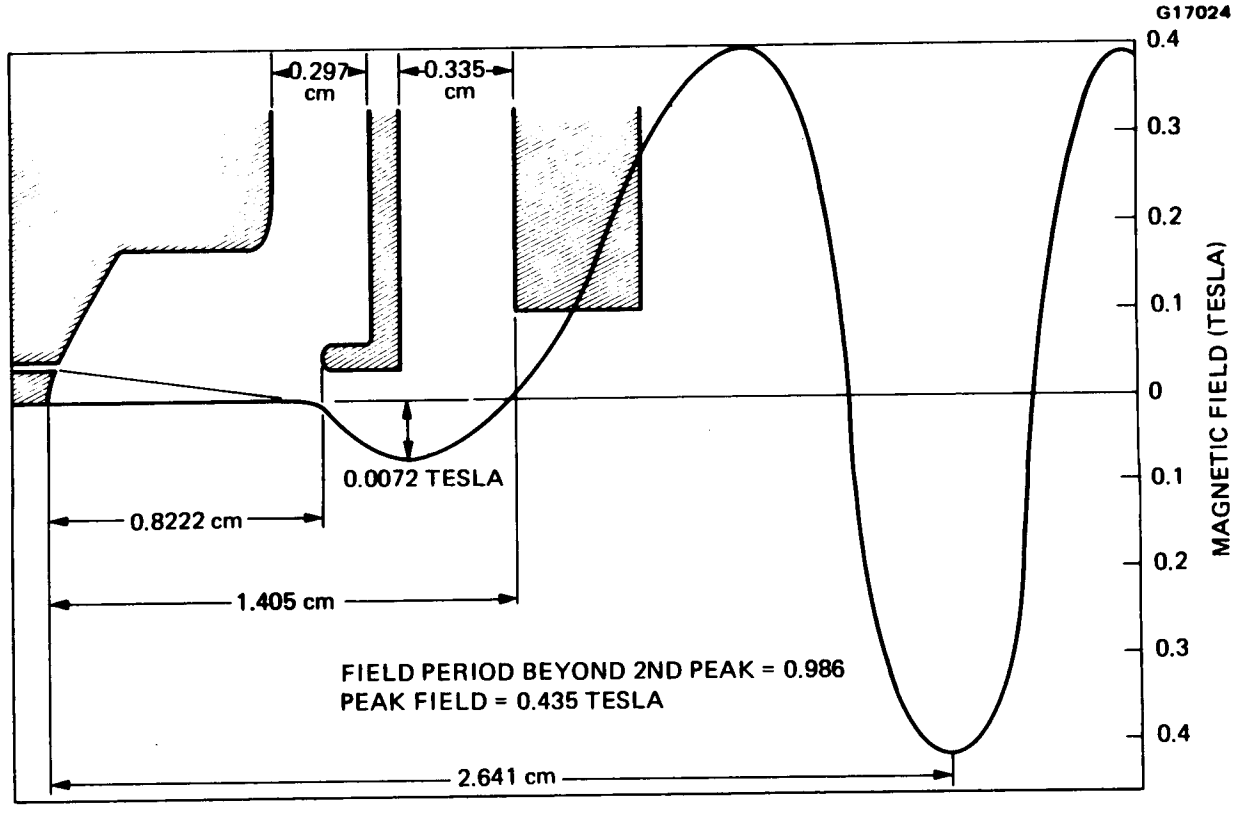

Figure 17 Electron optics design with magnetic field build-up.

Based on these measurements of the field in the gun region, a 6.35 cm diameter pole piece with a 0.508 cm diameter opening and a 2.54 cm long, 0.127 cm thick cylinder were chosen for the final design of the magnetic structure. This final pole piece design was then used as input in the Amboss thermal beam analysis code. Figure 18 shows a plot of the thermal beam radii as a function of distance from the cathode when focused with the final magnetic field design. Optimum focusing occurred with the gun positioned such that the first 0.435 tesla peak of the magnet occurred 2.09 cm from the center of the cathode. The beam profile plots depict the beam radius in five different ways. The plots shows the radii containing 99.5 and 95 percent of the beam current, the radii at which current density falls to 1/10 and to 1/20 of its peak value for a given distance from the cathode, and r_o, which is primarily of theoretical importance. As shown, the 262B electron gun focuses well into the 961H magnetic field to produce a beam satisfying the requirements.

3.1.3.3 Electron Gun Testing - A single 262B electron gun was tested on the beam analyzer and subsequently used on the feasibility tube tested. The beam radius was measured on the beam analyzer as a function of axial position and accelerating voltage for voltages ranging from 3.0 to 10.0 kV. Measurements at greater accelerating voltages could not be accomplished because of the high power density in the beam, but the beam size at higher operating voltage were evaluated by extrapolation. The beam size was 0.0056 cm less than the design value, but the gun focused and performed very well on the tube.

Figure 19 shows the measured beam current as a function of cathode temperature for an accelerating voltage of 10.0 kV. This curve indicates that the cathode was well activated during the test and that the gun exhibited the correct perveance. Figure 20 shows the measured beam radius as a function of beam voltage. The points fall on a straight line on the curve, indicating good agreement with the thermal theory. Extrapolation of the measured beam radius to 19.6 kV shows a beam size of 0.0160 cm at the operating voltage. The design value was 0.0244 cm. The minimum beam radius occurred 1.78 cm from the cathode, which is in good agreement with the predicted value.

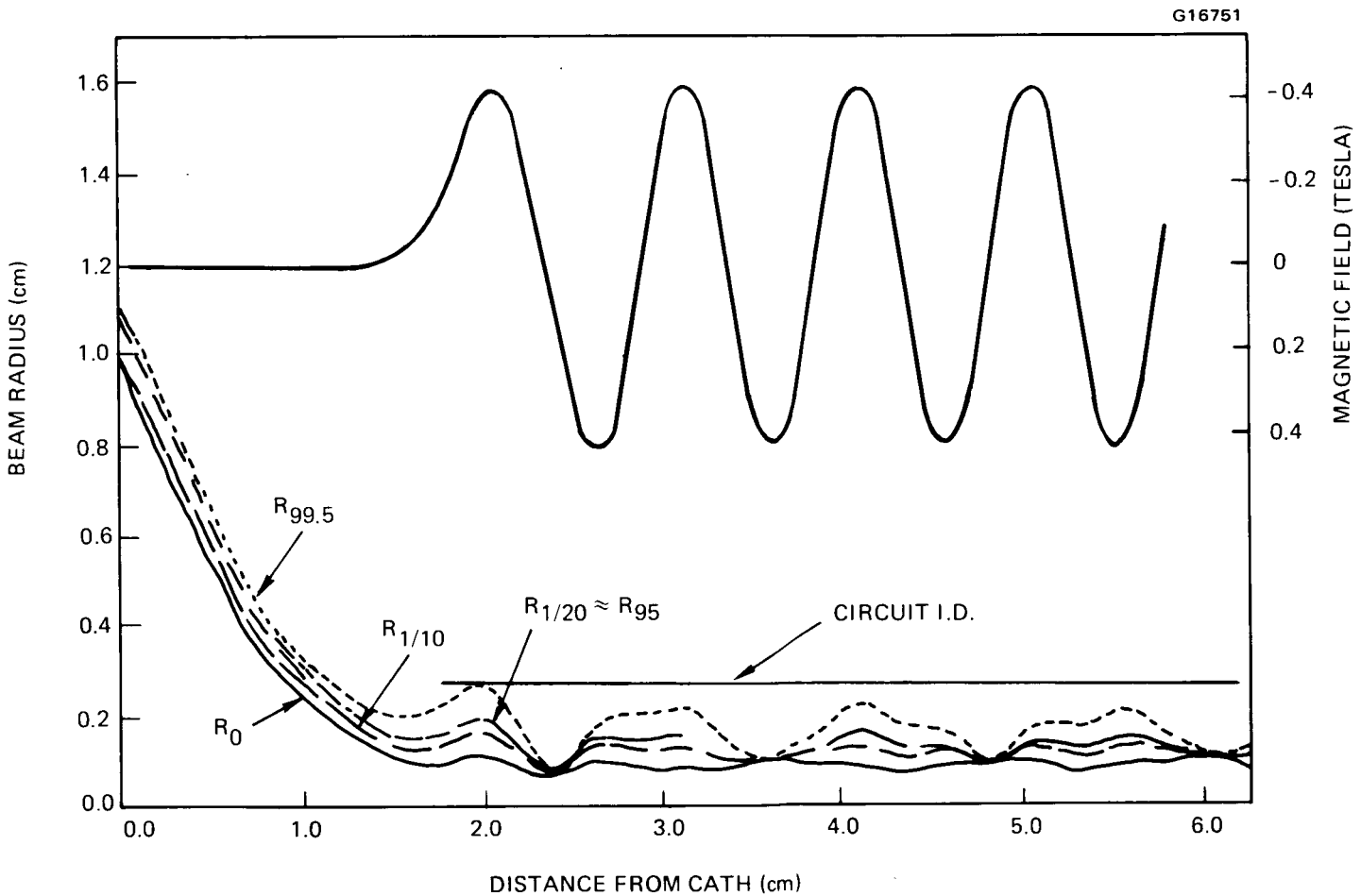

Figure 18 Computed beam profile for 961H isolated anode electron gun in magnetic field structure.

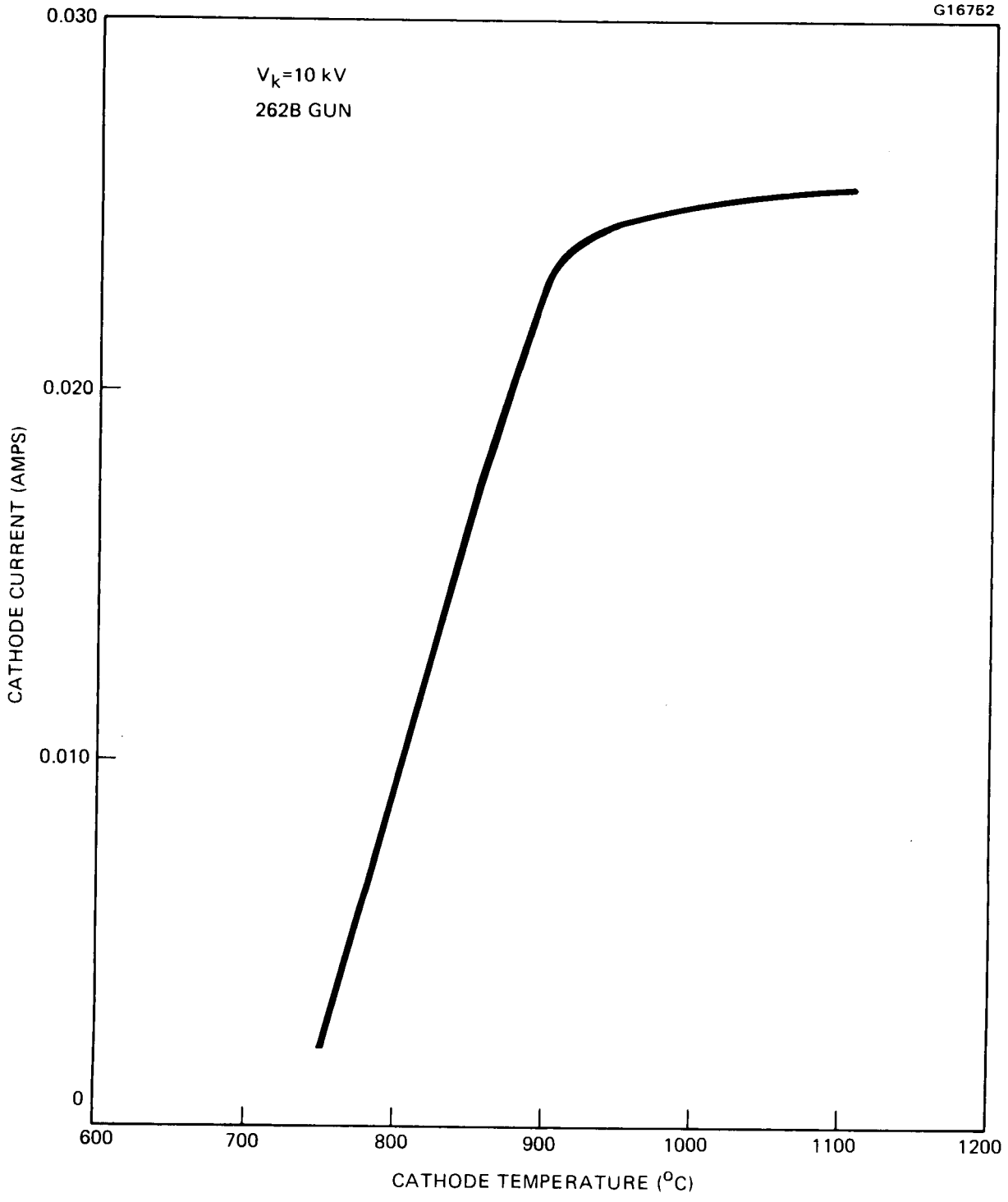

Figure 19 Measured beam current as a function of cathode temperature.

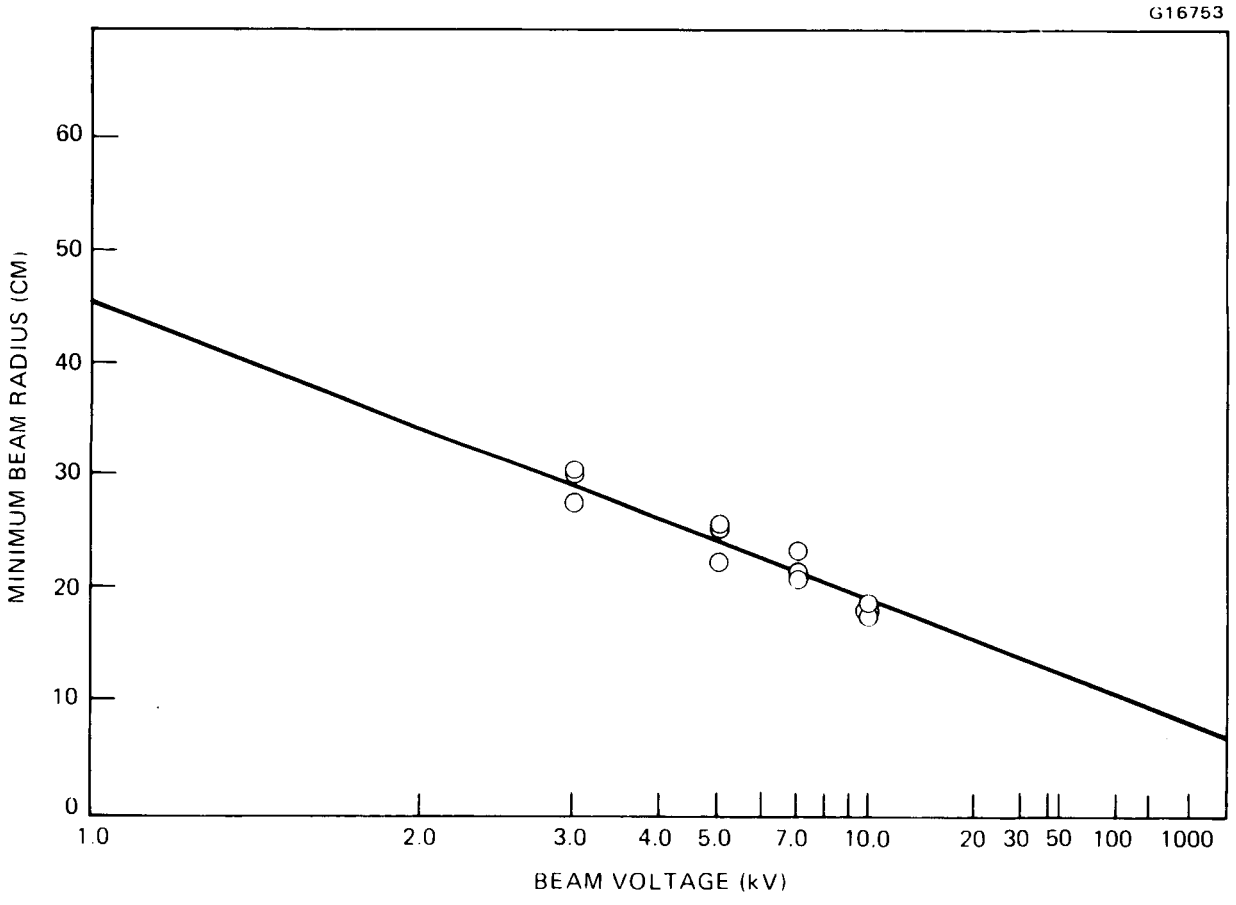

Figure 20 Measured beam radius as a function of beam voltage.

The difference between the measured and predicted value of the minimum beam radius may well be accounted for by the measurement and analysis technique. The beam size is found by passing an aperture through the beam at a given axial position, measuring current density as a function of radial position, and then determining the radius at which current density falls to 1/20th of its maximum value for the given axial position. This measurement is repeated all along the beam until the position with the minimum radius is determined. The radius measured, $r_{1/20}$, does not correspond directly with the radius containing 99.5 percent of the beam current, which was the radius referenced in the design of the gun. Without integrating the current density curves, the exact relationship between the two measures of radius cannot be determined exactly, but generally $r_{1/20}$ contains less than 99.5 of the current. The excellent performance of the gun on the tube suggests that the agreement between practice and theory is quite good.

3.1.4 Multistage Collector Design

The multistage collector had four depressed stages. The starting point for its design was the characteristics of the spent electron beam; principally the electron energy distribution.

Figure 21 shows the calculated spent beam energy distributions at 61.25, 62.75, and 64.25 GHz, obtained during the original design analysis with the one-dimensional coupled-cavity large signal interaction program. The curves are the integrated energy distributions at saturation for the corresponding frequency cases plotted in Figure 4. Characteristically, the knee of the energy distribution at the high frequency end is lowest, even though the basic efficiency (5.93 percent) is less than at midband and the low frequency end (6.69 and 6.01 percent, respectively). The lowest knee, in this case occuring at 80 percent at the dc voltage, determines the maximum depression of the first stage, to avoid a body current increase due to electron turnaround. On the basis of the energy distributions, the nominal depression voltages were selected at approximately 78, 82, 87, and 93 percent of the cathode voltage.

Additional information about the electron trajectories entering the collector was obtained with the Detweiler continuous interaction program, which uses a

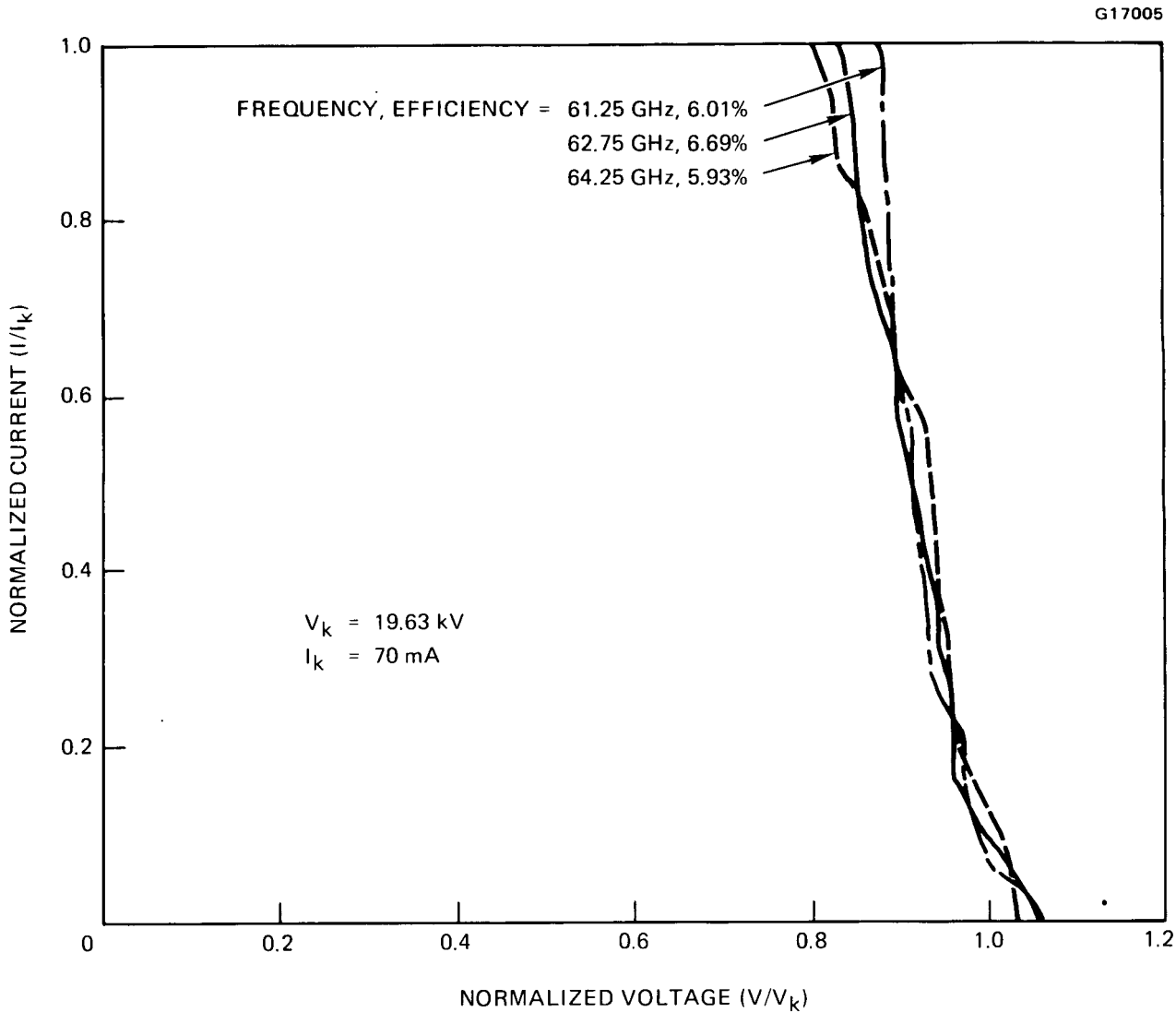

Figure 21 Calculated integrated spent beam energy distributions at three frequencies over a 3 GHz band at saturation.

deformable disk representation of the electron beam.[3] The calculation takes into account the axial and radial electric forces associated with the propagating RF wave and those due to the space charge in the bunched beam,[4] as well as the magnetic forces of the PPM focusing field. Because the interaction in a cavity is weak at MMW frequencies, a continuous wave interaction model describes the amplification process very adequately. In effect, an equivalent average interaction over a cavity is being calculated, by using the Pierce impedance of the dominant interacting space harmonic. In contrast to PPM-focused TWTs at lower frequencies, where a magnetic cell is formed at each RF cavity, at millimeter-waves a single magnetic cell extends over several cavities (approximately five in the 961H). The magnetic field is thus relatively constant over an RF cavity. In the absence of rapid spatial variation of the magnetic field, little accuracy is lost in calculating the electron trajectories by averaging the comparatively weak RF forces over a cavity period.

Some data of interest concerning the 32 disks that were used to represent an RF wavelength of the electron beam are listed in Table V. The trajectory angles in the spent beam were less than 4 degrees.

TABLE V

ELECTRON DISK DATA OF THE SPENT BEAM

Parameter	Maximum	Average	Std. Deviation
Disk Radii:			
r (cm)	0.0208	0.0101	0.0061
r (inch)	0.0082	0.0040	0.0024
Disk Edge Trajectories:			
Slope, dr/dz	+0.068 -0.062	-0.002	0.039
Angle (degrees)	+3.92 -3.55	-0.13	2.25

With a well-controlled, low perveance beam, there was little advantage in preconditioning it by expansion and recollimation in a refocusing section prior to injection into the collector. However, the mechanical design of the radiation-cooled collector required a space for the electrical feedthroughs between the output coupler and the collector pole piece. Consequently, there was a 2.5-cm drift section (with a 2.5-mm tunnel) following the output coupler. This section was focused by the same type of PPM array that focused the circuit. Since there had to be a drift region, it would have been better to take advantage of it, by using it as a refocusing region and designing the collector accordingly. The timing of events during the 961H development made this impractical, however.

The collector electrode design was performed by trajectory calculations with the Herrmannsfeldt program.[5] Appropriate input trajectories for the Herrmansfeldt program can be obtained from the Detweiler disk representation of the spent beam in several ways. One method is to divide each disk into several radial rings, typically four or five (including a central disk), and represent each ring with a single current-carrying trajectory. The rings can be constructed to have equal currents, in which case the radial widths will decrease with increasing ring radius, or they can be constructed to have equal radial widths, with the current per ring increasing with radius. Although equal current rings make a quantitative analysis of the collector performance easier, equal radial widths provide a more detailed description of the trajectories close to the axis. These trajectories, if they also have low and intermediate energies, are the ones that are least efficiently collected in any multistage collector with rotational symmetry. The trajectory angles are assigned consistent with the Detweiler laminar beam model; i.e., the angle is that of the disk edge electron (obtained from the Detweiler program) reduced in proportion to the distance from the axis.

Using the method just described, the Herrmannsfeldt trajectories at the collector entrance can be generated for each of the 32 disks in the Detweiler spent beam. With the computing speed and resources that are currently available, a Herrmannsfeldt run with, say, 160 trajectories is by no means excessively large or expensive. However, a more efficient approach is to first establish the electric potential distribution within the collector (in the presence of space charge) by using a beam with a reduced number of energy groups. In the present case, eight energy groups were used, with each energy group containing five trajectories. The energies were chosen so that two groups would turn around between each successive pair of stages, while the last two groups had more than enough energy to enter the last stage. The currents in the groups were adjusted so that the corresponding energy distribution conformed as closely as possible to that calculated with the one-dimensional large signal program. In particular, the total power in the spent beam, which is given by the area under the energy distribution curve, was adjusted to be the same. In effect, the 32 disks were combined into eight "super disks", with radii and edge trajectory slopes representative of the original disks in the corresponding energy range.

Given an electrode configuration and operating voltages, an initial run was thus made to establish the potential distribution in the collector in the presence of space charge, by injecting a beam derived from the eight super disks. The resulting self-consistent potential distribution, obtained after several iterations, was then frozen. Subsequently, the multiple trajectories derived for each of the 32 disks in the original spent beam model were traced out and selectively plotted in several graphs. This method of analysis was very efficient, because each trajectory now had to be traced out only once through the collector region. The several iterations necessary to obtain a self-consistent potential in the presence of a large number of trajectories were avoided. At the same time, the validity of the results was not compromised, since the potential distribution is relatively independent of the detailed trajectory representation of the spent beam.

Trajectory calculations were made for several four-stage designs, with a bucket as the last stage, and for a five-stage collector, with a spike at cathode potential as the extra stage. Several spike positions were evaluated; in all these cases, there were always some trajectories close to the axis, which were reflected back through the aperture of the fourth stage by the spike.

Figure 22 shows the calculated electron trajectories in the final four-stage design, where the last stage is a bucket with a thin vane (0.25 mm thick) across its aperture. The purpose of the vane was to modify the equipotential surfaces (and thus the force fields) at the aperture, to prevent turnaround electrons from being reflected back toward the axis. The vane could not actually be modeled, since it lacked cylindrical symmetry, but to some extent its effect was included by enforcing an equipotential at its front edge as shown. The aperture of the first stage was small in relation to the collector size, but still more than five times larger than the beam hole diameter. This was done to minimize the probability of electrons escaping from the depressed collector back to body potential; such return current is particularly undesirable when the collector is strongly depressed. In the computer run, each of the 32 disks were represented by four trajectories, while only half of the trajectories have been plotted in the figure.

The trajectories for the dc beam, and the corresponding potential distribution, are presented in Figure 23. The beam is here composed of three groups, with maximum trajectory slopes of the edge electrons of $dr/dz = \pm 0.015$ and zero.

On the basis of the trajectory calculations, with four charge rings per disk, the estimated collector efficiency was typically 95 percent. The performance was corrected for emission of low energy secondaries, with an emission coefficient of unity, and included the effect of vane interception. To account for the effect of high energy (elastically scattered) secondaries, it was conservatively assumed that 2 percent of all the current entering the last bucket stage returned to the second stage.

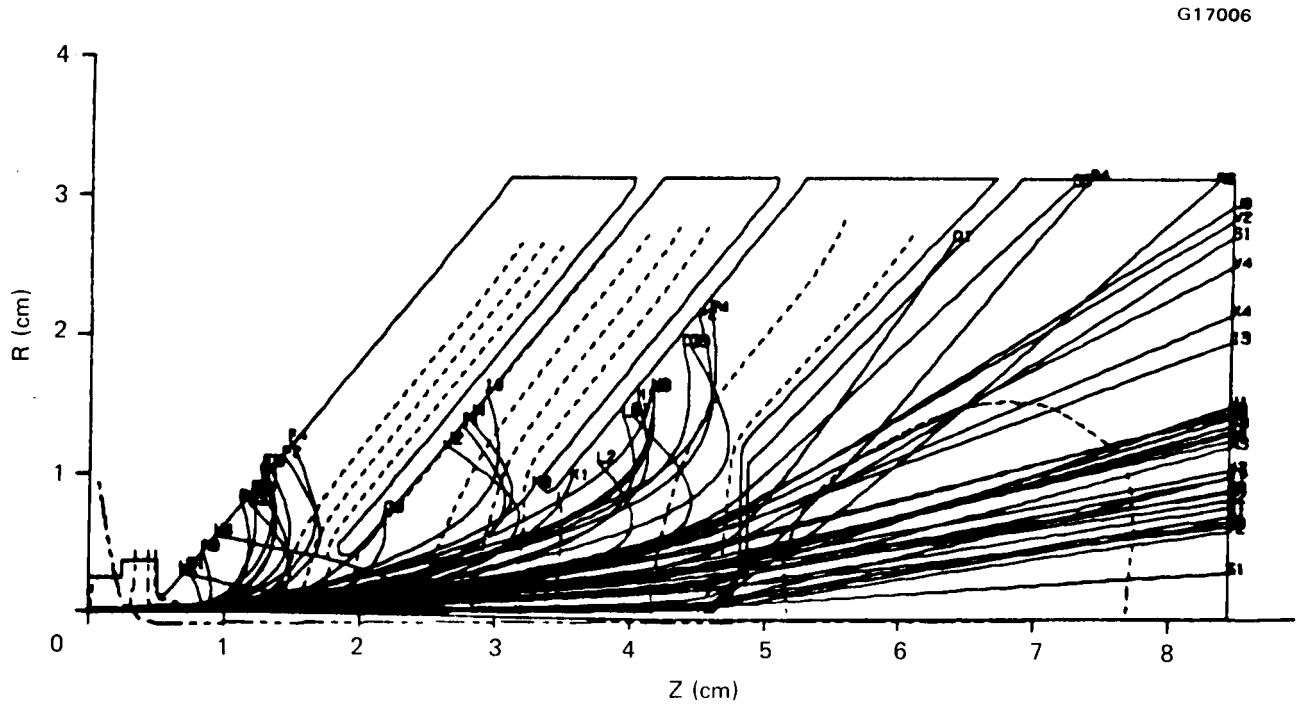

Figure 22 Electron trajectories in the 961H four-stage depressed collector at RF saturation.

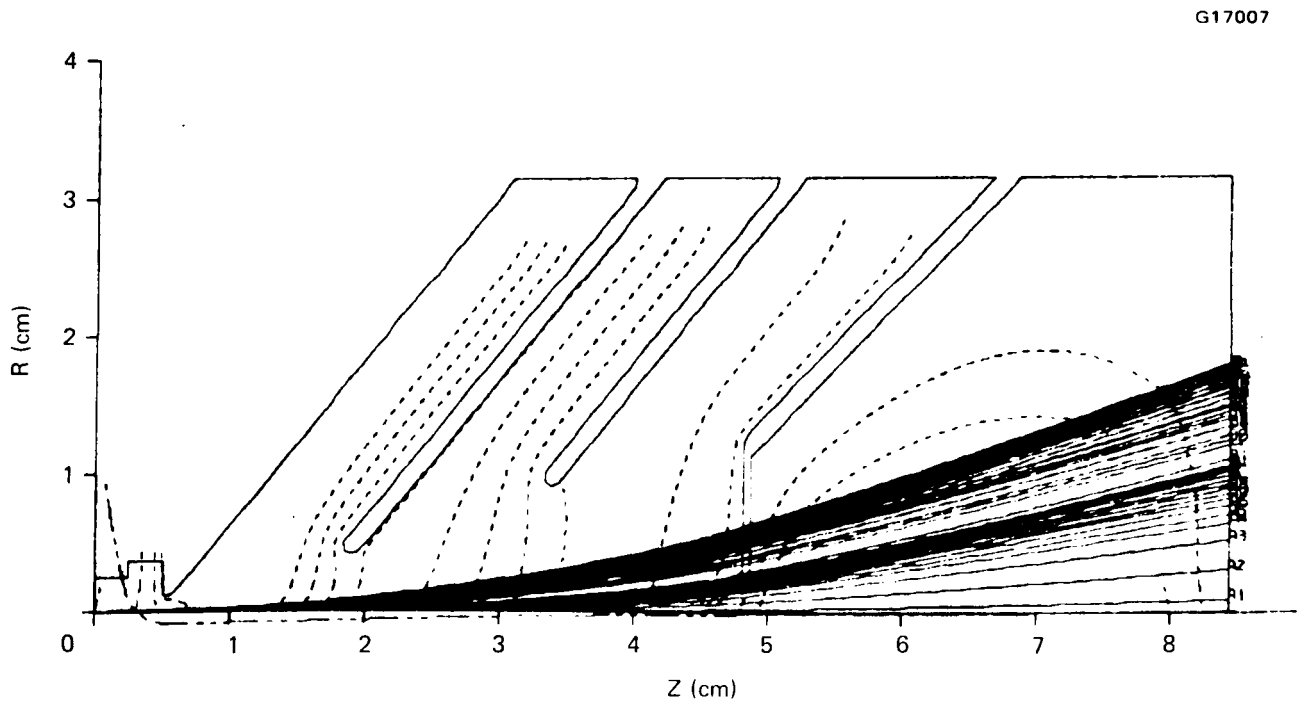

Figure 23 Electron trajectories in the 961H four-stage depressed collector with no RF drive.

The overall efficiency, η, depends primarily on three performance parameters for a given type of TWT: (1) the basic efficiency, η_o, (2) the beam transmission to the collector with RF drive but without depression, X_{RF}, and (3) the efficiency of the depressed collector, η_c. Since collector efficiency is the fraction of the kinetic beam power recovered by the collector, it is necessary to evaluate the power in the spent beam.

For the 961H, the spent beam power was calculated by subtracting the following quantities from the dc beam power:

1. The RF output power.

2. The intercepted beam power. We may separate the intercepted current (without collector depresseion) into two parts: the interception with no RF drive, $I_{\omega dc}$, and the increase due to RF drive, $\Delta I_{\omega RF}$. It is customary to assume that the part $I_{\omega dc}$ is intercepted at full beam voltage even with RF drive, while the part $\Delta I_{\omega RF}$ is intercepted at somewhat reduced voltage, such as at a fraction $(1 - \eta_o)$ of the dc voltage. Since in the 961H, the body current without depression only increased a small amount with RF drive (from 2.2 mA dc to 2.4 mA with RF in one tube with a good gun), and since the basic efficiency was small, the full dc beam voltage could be assigned to the total intercepted current without loss of accuracy.

3. The total dissipated RF power. It is composed of the ohmic surface losses in the RF circuit, the power absorbed in the terminations, and the power lost in the output coupler and window. Our past experience with V-band TWTs indicates that the coupler and window loss is approximately 0.2 dB, or a fraction 0.045 of the RF output power. The remaining components are computed with our large signal code. Typically, the total circuit dissipation at saturation is predicted to be about 20 percent of the RF output power at midband and the low frequency end of the band, while increasing to 25 percent toward the high frequency.

With these assumptions (and ignoring the negligible RF drive power in the energy balance), the overall efficiency is

$$\eta = \frac{\eta_o}{1 - \eta_c (X_{RF} - 1.245\ \eta_o)} \tag{4}$$

Solving for the collector efficiency gives

$$\eta_c = \frac{1 - \eta_o/\eta}{X_{RF} - 1.245\ \eta_o} \tag{5}$$

These expressions hold at midband and the low frequency end. At the high frequency end, the factor 1.245 should be replaced by 1.295 to account for the increased dissipation power.

Figure 24 shows the overall efficiency as a function of collector efficiency for basic efficiencies of 6.0 and 6.5 percent and RF beam transmission values of 97 and 98 percent, while Figure 25 is a plot of the collector efficiency which is necessary for achieving an overall efficiency of 40 percent. With 6.0 percent basic efficiency and 97 percent transmission, the required collector efficiency is 95 percent. If heater power (2.8 W in the 961H) is included, the required value is about a quarter of a percentage point higher; in equation (5), the term $P_{heater}/P_{dc\ beam}$ should then be added to the numerator.

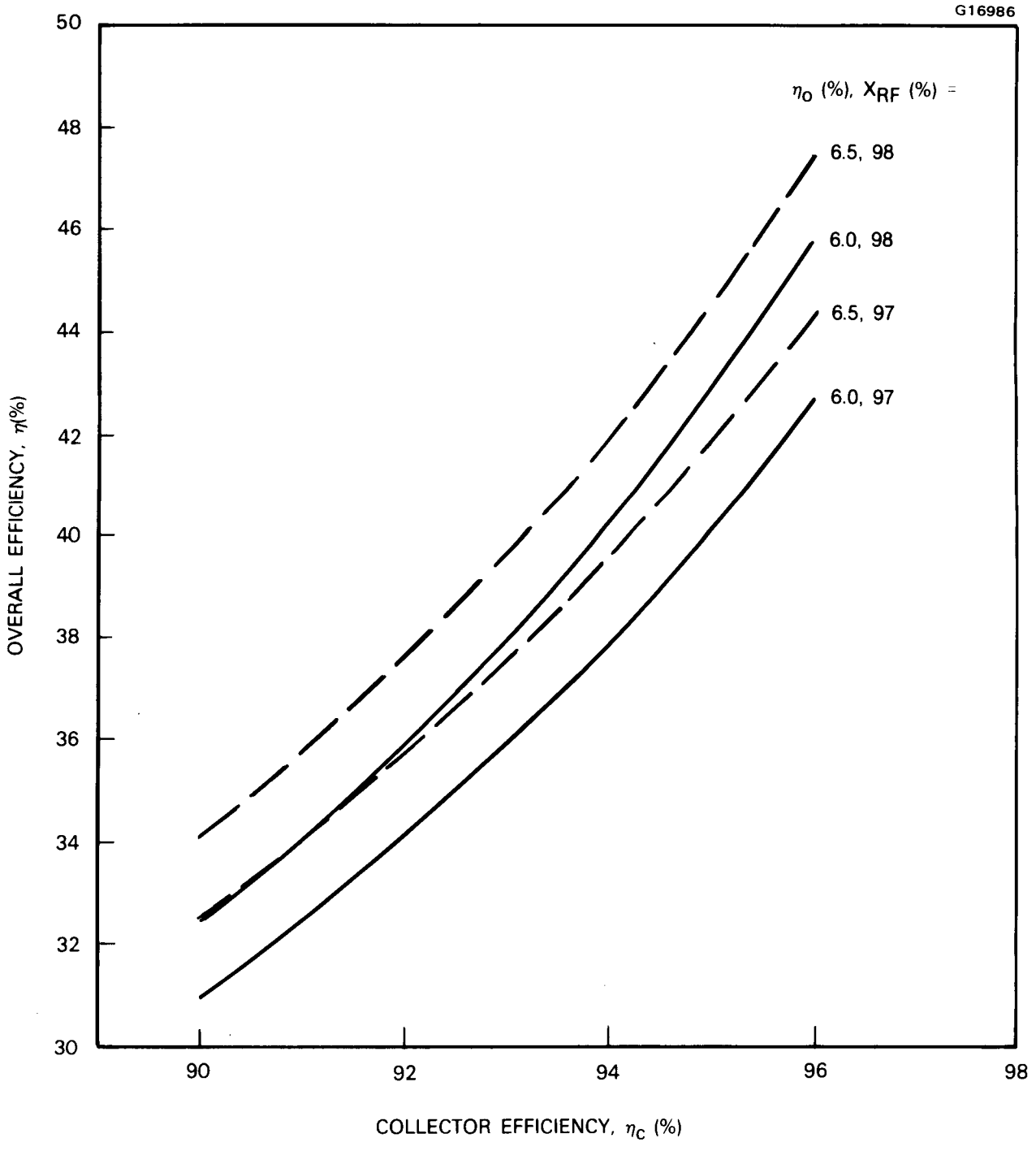

Figure 24 Overall efficiency as a function of basic efficiency, beam transmission, and collector efficiency.

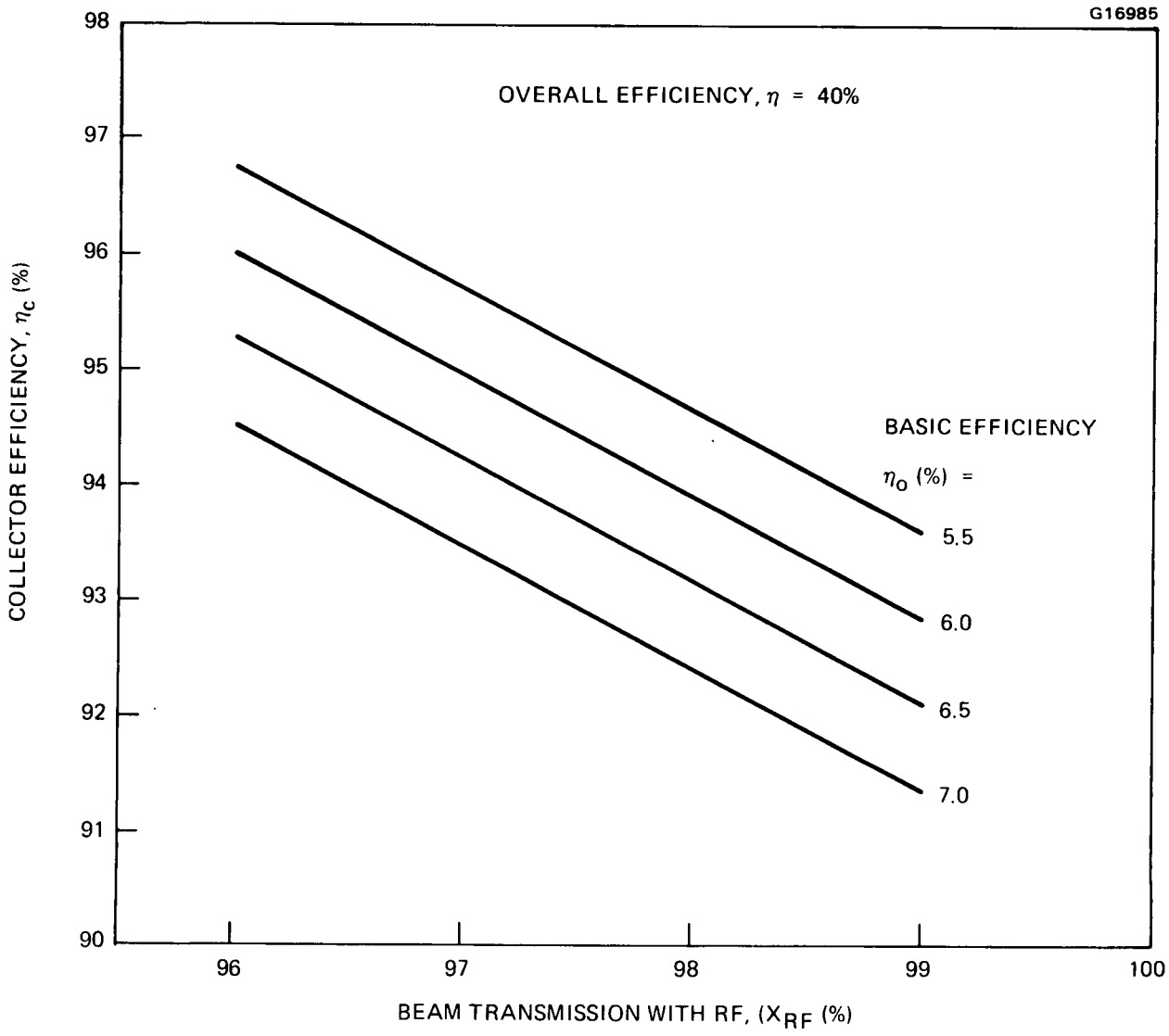

Figure 25 Collector efficiency required to achieve an overall efficiency of 40 percent.

3.2 MECHANICAL DESIGN

Mechanically, the vacuum envelope of the tube consists of three major components; the RF interaction circuit, the multistage collector, and the electron gun. The circuit portion includes the pole pieces for locating the focusing magnets, as well as the waveguide transformers and vacuum windows. An external baseplate supports the tube and completes the tube package. These elements are described in more detail in the following sections.

3.2.1 RF Circuit

The RF circuit consists of 169 individual copper circuit cavities, including the internal sever termination and waveguide matching cavities. The total interaction circuit is broken down into three separate sections that are terminated internally for stability. A drawing of a typical 961H circuit cavity is shown in Figure 26. After the individual parts have been adjusted in the matching procedure, they are cleaned and joined together by diffusion bonding. During this process, the parts are assembled on a firing fixture. Alignment of the circuit section is maintained by two sapphire rods at the tooling arcs at the edges of the circuit cavities.

After the circuit section is diffusion bonded, it is brazed to the matching waveguide transformer and pole piece. Figure 27 is a drawing of the final assembly of the output circuit section. The waveguide match is made through the four-step impedance transformer. The waveguide vacuum window will later be brazed to the flange of the end of the waveguide transformer section. Beyond the transformer at the output end of the tube (the experimental model) is a drift section with a series of pole pieces. This section was included to provide room to clear the high-voltage terminals from the multistage collector. At the beginning of the output circuit section, it is terminated in an internal termination.

A drawing at the termination assembly is shown in Figure 28. The termination itself consists of a conically tapered lossy ceramic whose dimensions are

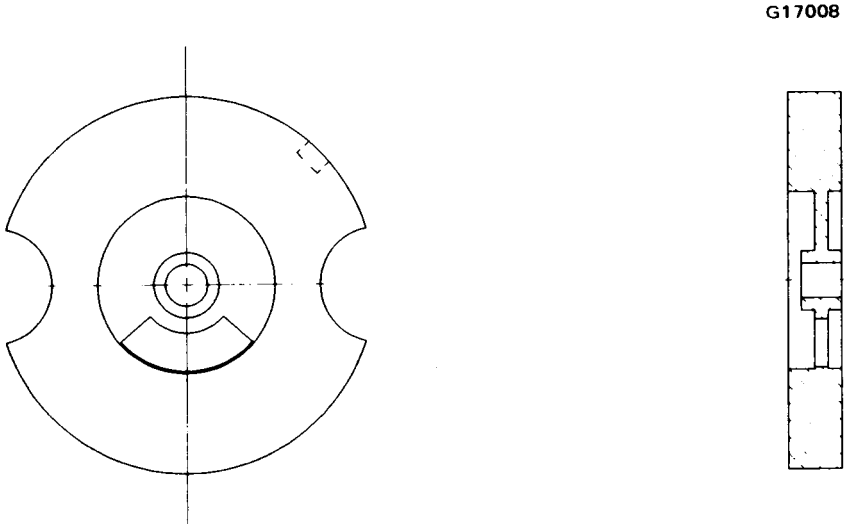

Figure 26 Typical 961H circuit section.

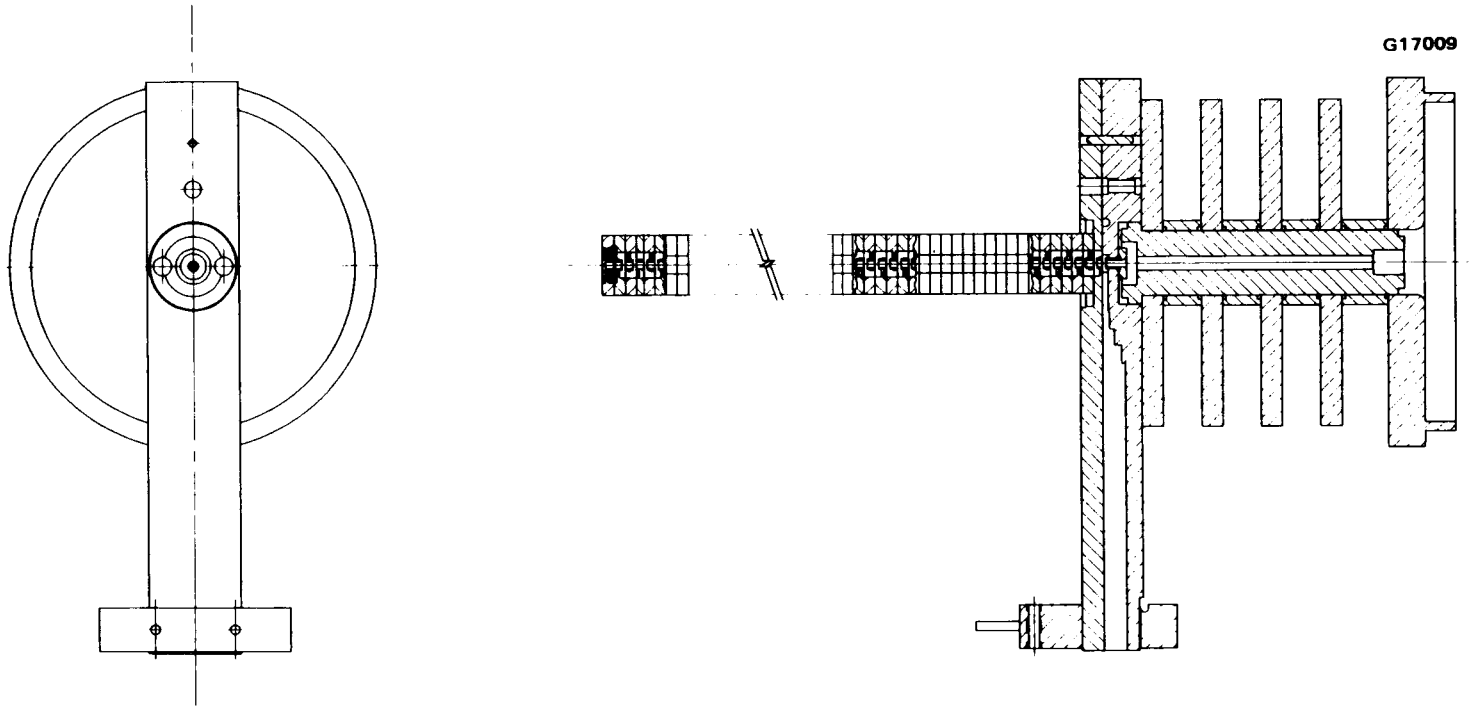

Figure 27 Output circuit transformer and pole piece subassembly for the 961H.

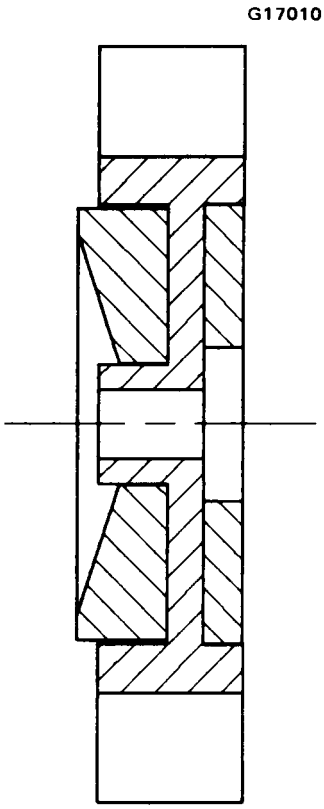

Figure 28 Internal sever termination subassembly for the 961H.

determined empirically to provide a good circuit match at the V-band operating frequencies. A representative circuit section match is shown in Figure 29. As shown, the circuits matched well with less than 20 percent reflection.

The input and center circuit sections are assembled the same way as the output section. The input pole piece configuration is different than that of the output. The center section is terminated internally at both ends.

The separate circuit sections are brazed into the pole piece and sheath assembly, which completes the vacuum envelope of the circuit by brazing the sheath at each end to the waveguide transformer. Figure 30 shows the circuit assembly mounted within its brazing fixture, along with the multistage collector and collector face assembly (which will be discussed later).

The periodic permanent magnet focusing structure is an integral part of the RF circuit and serves to complete the vacuum envelope as described above. The structure also provides alignment and mechanical support to the whole circuit assembly. The sheath and pole piece assembly, shown in Figure 31 consists of a precision thin wall stainless steel tubing on which alternating iron pole pieces and copper spacers are stacked and brazed. Then, after the brazing process, the inner diameter of the tubing is honed to ensure a straight, precision alignment for the circuit sections. The extensions on the pole pieces near the input and output of the circuit are copper cooling fins.

The waveguide vacuum window, shown in Figure 32, consists of a half-wavelength beryllia ceramic block. Circular matching irises are incorporated to adjust the match of the window to the required frequency band.

Figure 33 shows the final brazed circuit body assembly with the windows installed. Completion of the vacuum envelope of the tube is accomplished by welding the circuit body braze assembly to the collector and electron gun assemblies. Final stacked brazed VSWR match characteristics were very good, less than 20 percent reflection as shown in Figure 34.

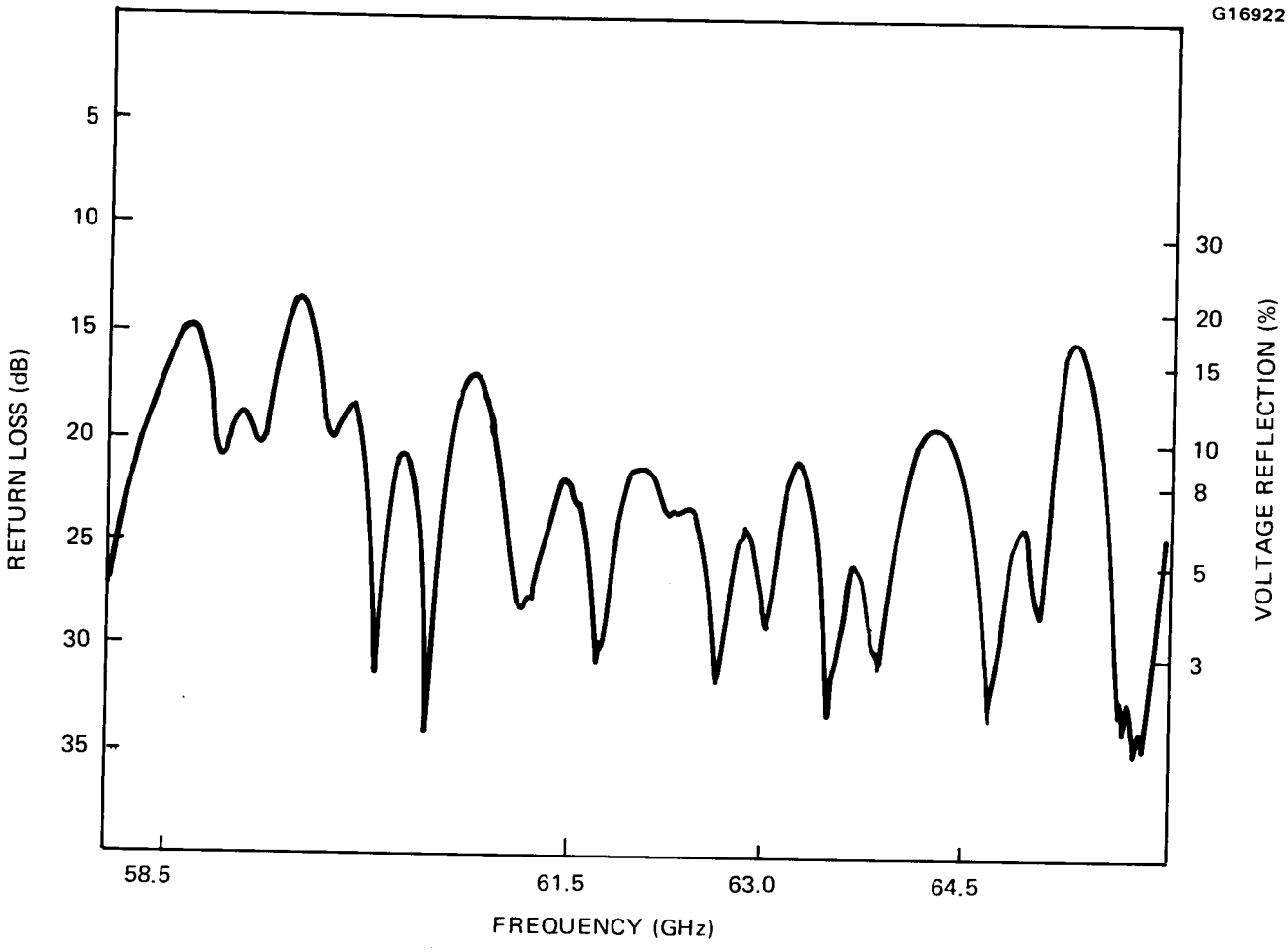

Figure 29 VSWR match of input circuit into termination after diffusion bond of S/N 2.

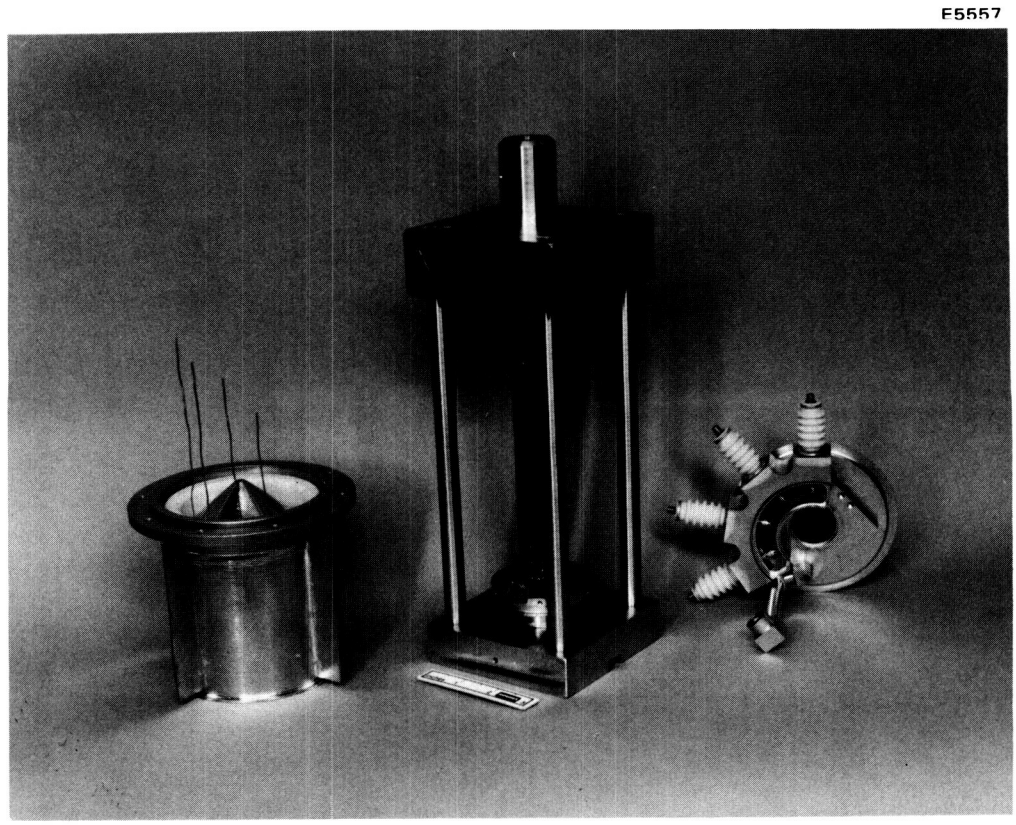

Figure 30 Photograph of 961H circuit assembly in the brazing fixture with the collector and collector faceplate assemblies.

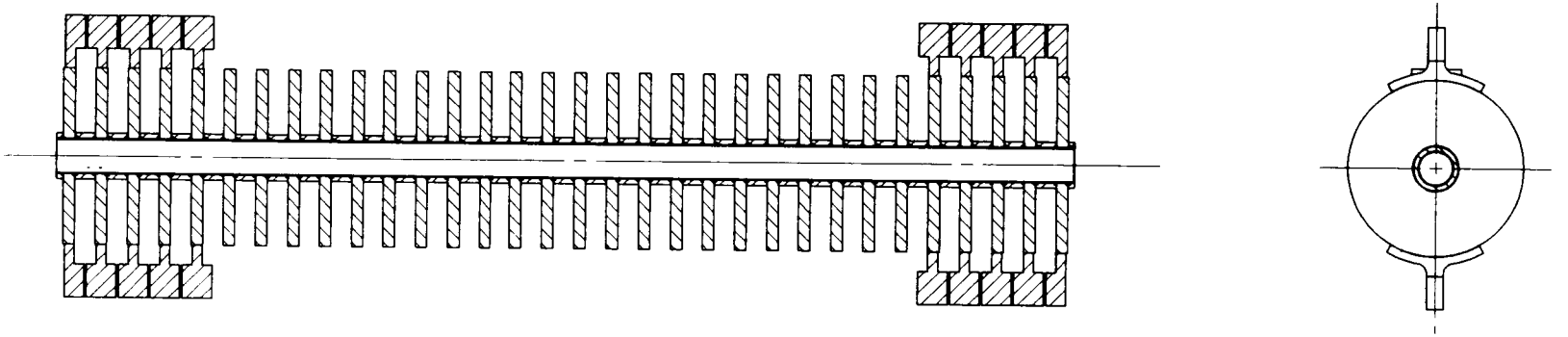

Figure 31 Pole piece and sheath assembly for the 961H.

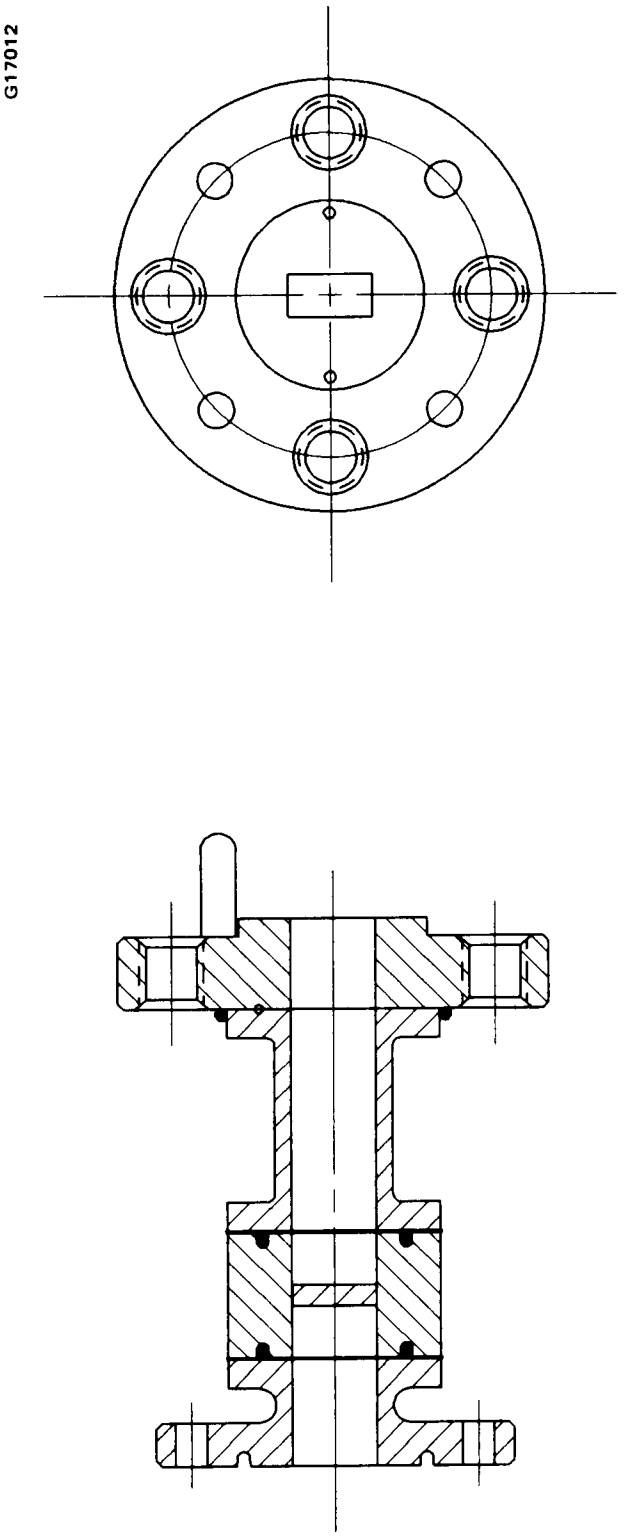

Figure 32 Waveguide vacuum window for the 961H.

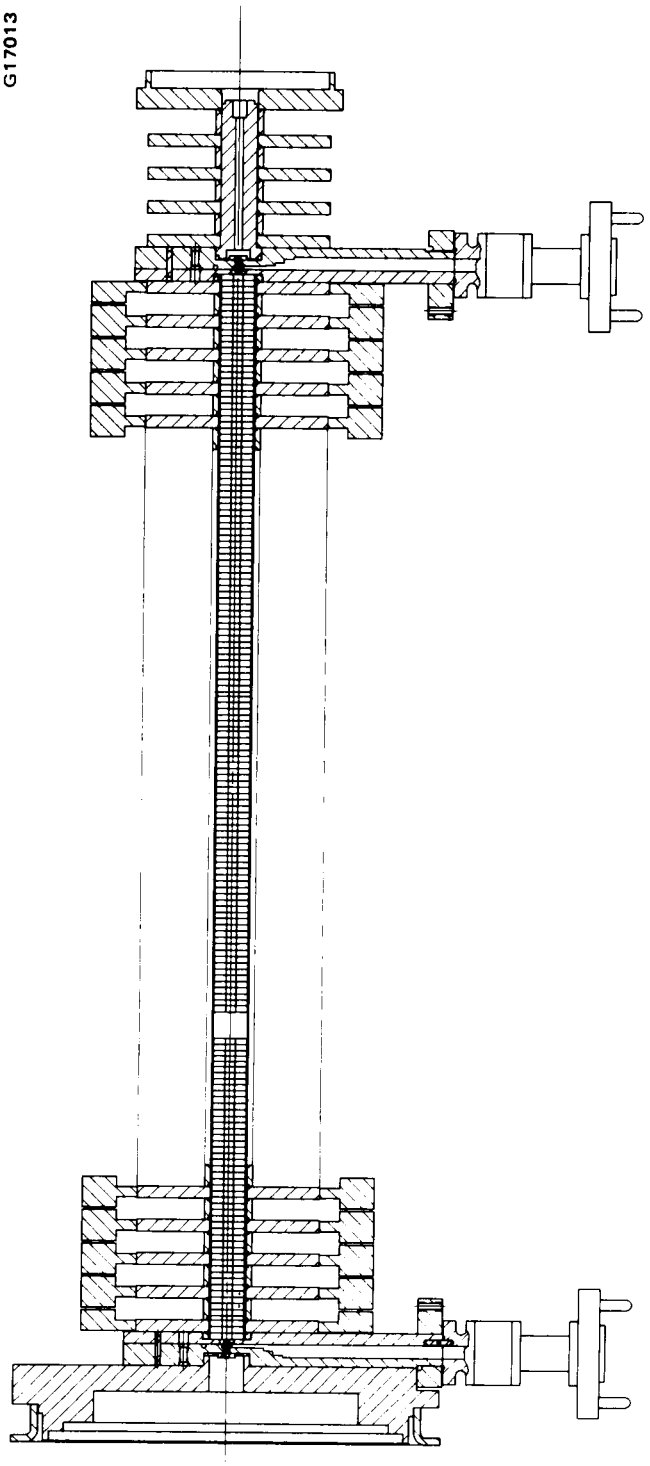

Figure 33 Body and window assembly.

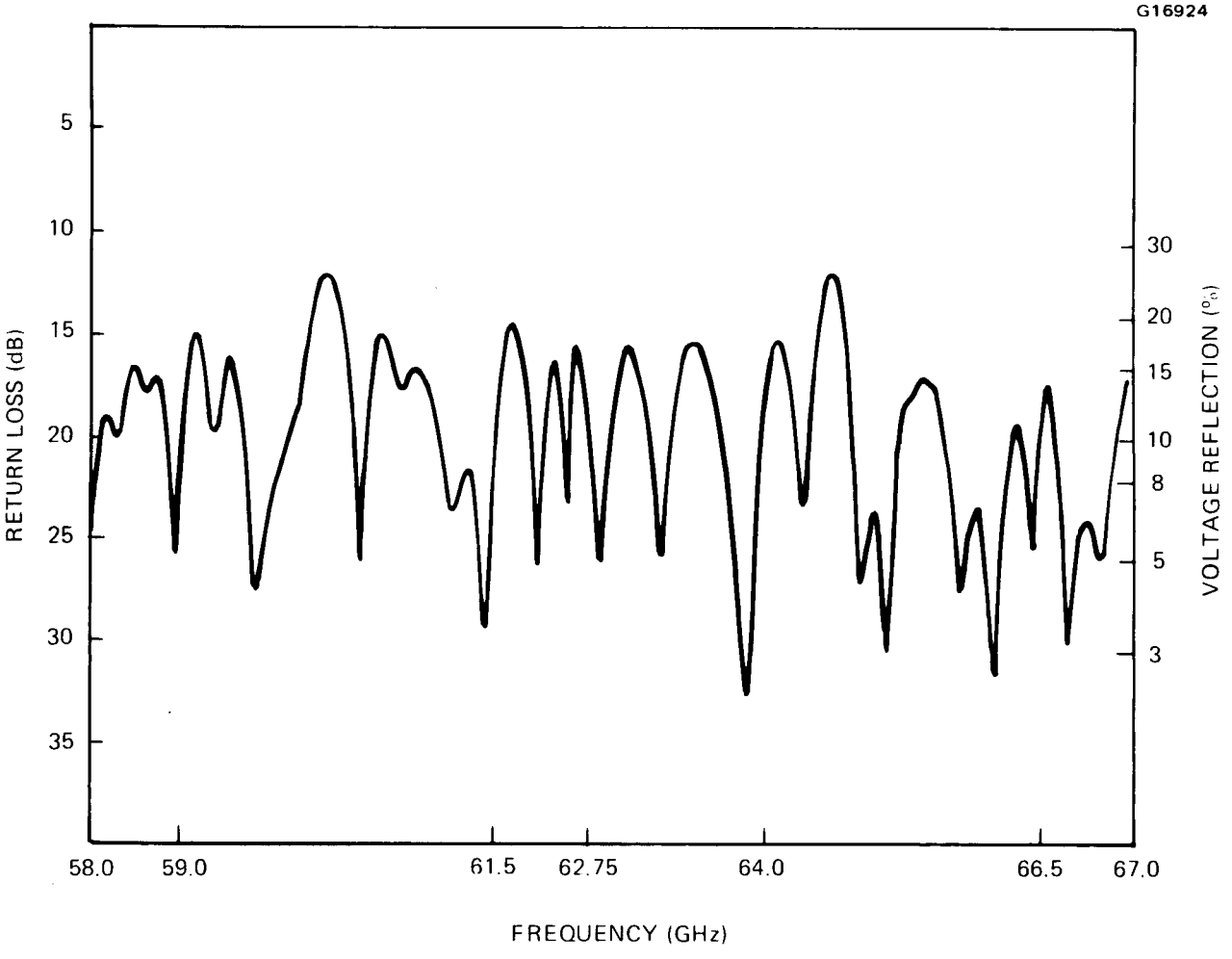

Figure 34 Final stack brazed VSWR match of output circuit of S/N 2.

3.2.2 Multistage Depressed Collector

The collector consists of four stages operating at successively higher depression voltages. The individual collector electrode stages consist of thin copper cones. The shapes of the cones were determined in the electrical design to optimize efficiency. The collector cones are brazed to the inside diameter of an alumina ceramic cylinder. The ceramic gives electrical isolation and provides a direct thermal path to the outside. A copper cylinder is brazed around the alumina ceramic to make the final vacuum seal. The copper is restrained by a molybdenum fixture during the braze to keep it in contact with the alumina ceramic. A drawing of the collector subassembly is shown in Figure 35. The electrodes are connected electrically through leads fed out through high-voltage terminals. In Figure 35, the leads are shown at the entrance end of the collector.

Figure 36 shows the collector with the end cap brazed on. Because of the high power that will be dissipated at the back of the collector when the tube is operated without RF input, the end cap is constructed of a relatively massive plate of copper and a beryllia ceramic ring to conduct the heat to the collector's external, radiating surface. External surfaces of the collector are at ground potential in this configuration. A thermal analysis of the collector is presented in Appendix A.

Some of the collector parts, including three of the electrodes, are shown in Figure 37. Four fins are brazed to the outside of the collector body to increase the radiating surface area. The wire leads have not been brazed to the electrodes at this stage. The finished collector assembly is shown in Figure 30.

One of the most difficult mechanical design problems was to locate the high-voltage collector lead terminals. Because of the high voltages required, the terminals had to be relatively large in comparison to the small millimeter-wave circuit components. The solution was to mount the terminals in a machined faceplate assembly. This assembly serves as a transition between the RF circuit and the collector. A drawing of this assembly is shown in Figure 38. The feedthrough terminals are brazed onto the iron faceplate, which is a fairly

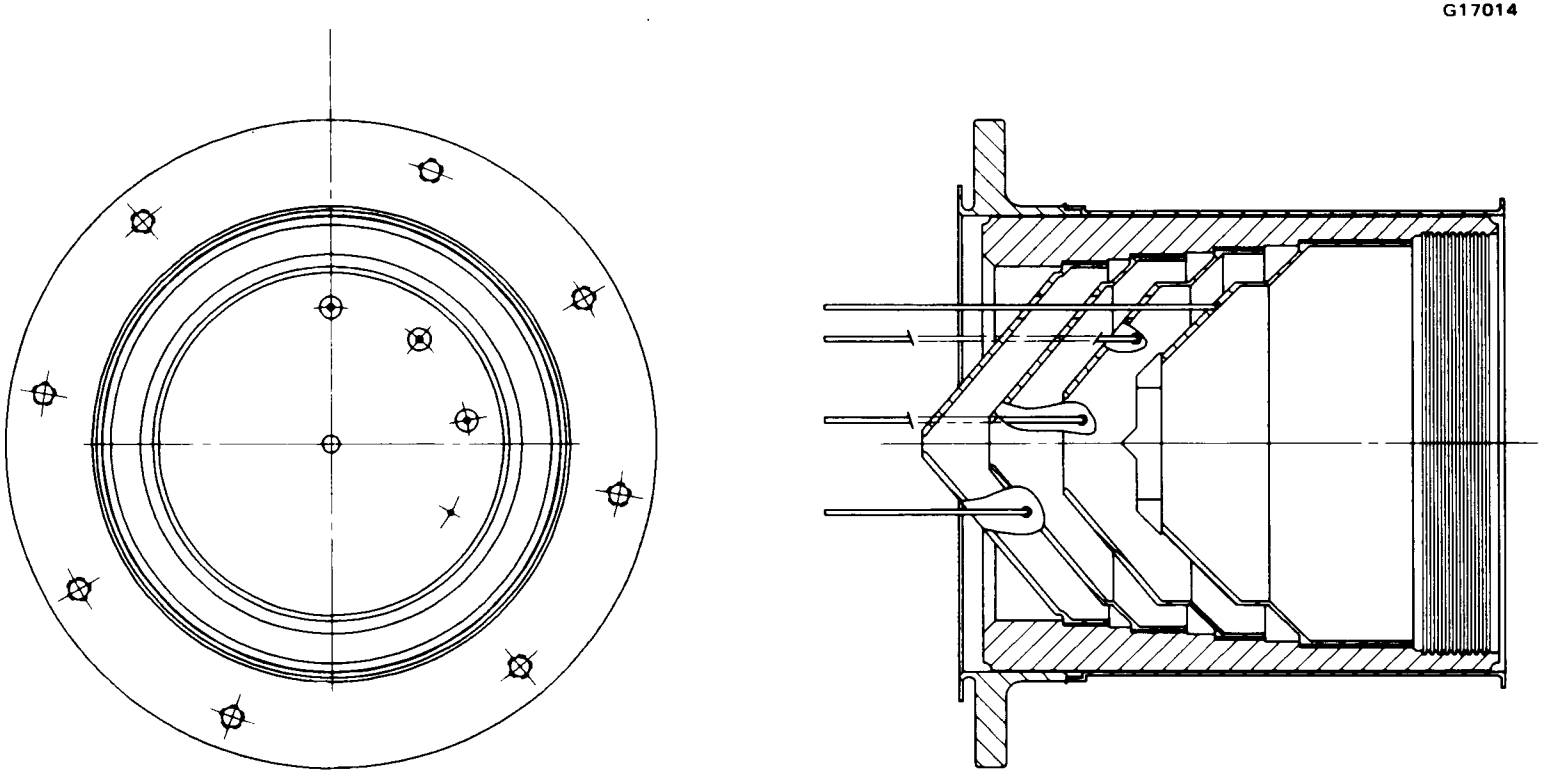

Figure 35 Multistage collector subassembly for the 961H.

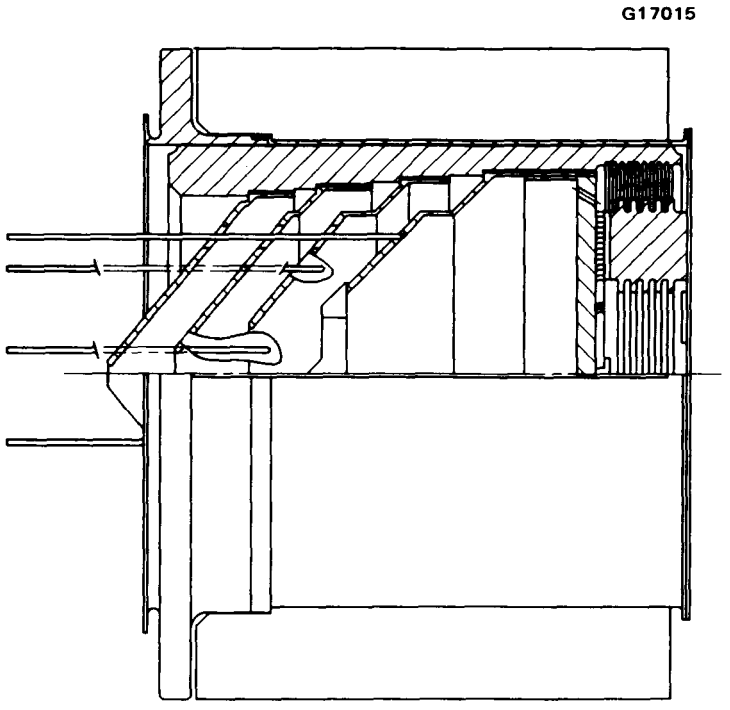

Figure 36 Collector assembly with end cap of the 961H.

E5558

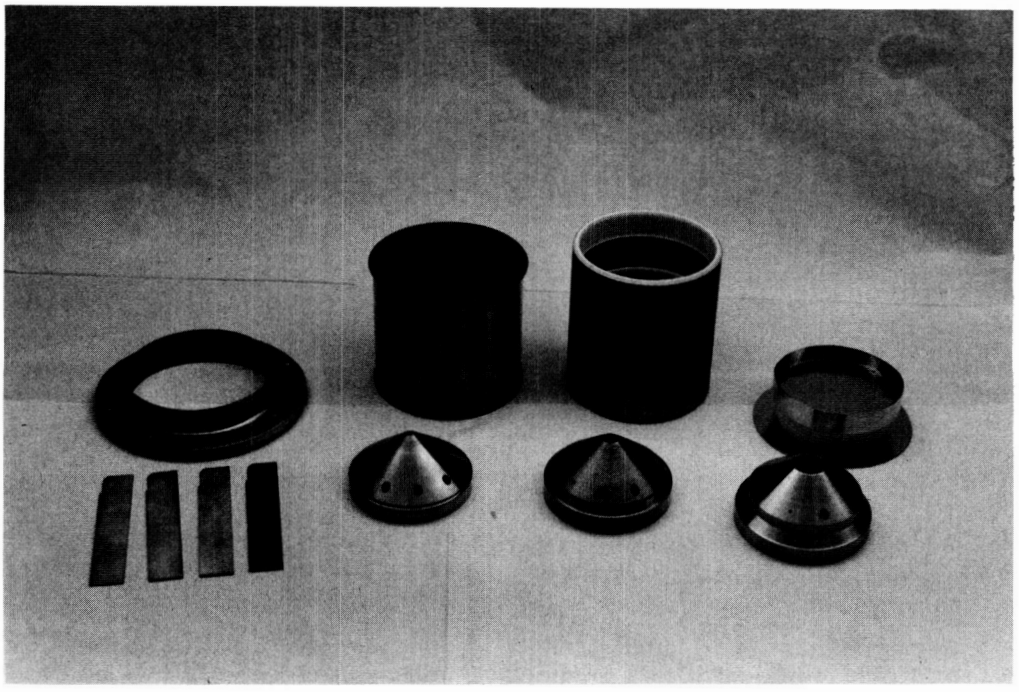

Figure 37 Collector parts for the 961H.

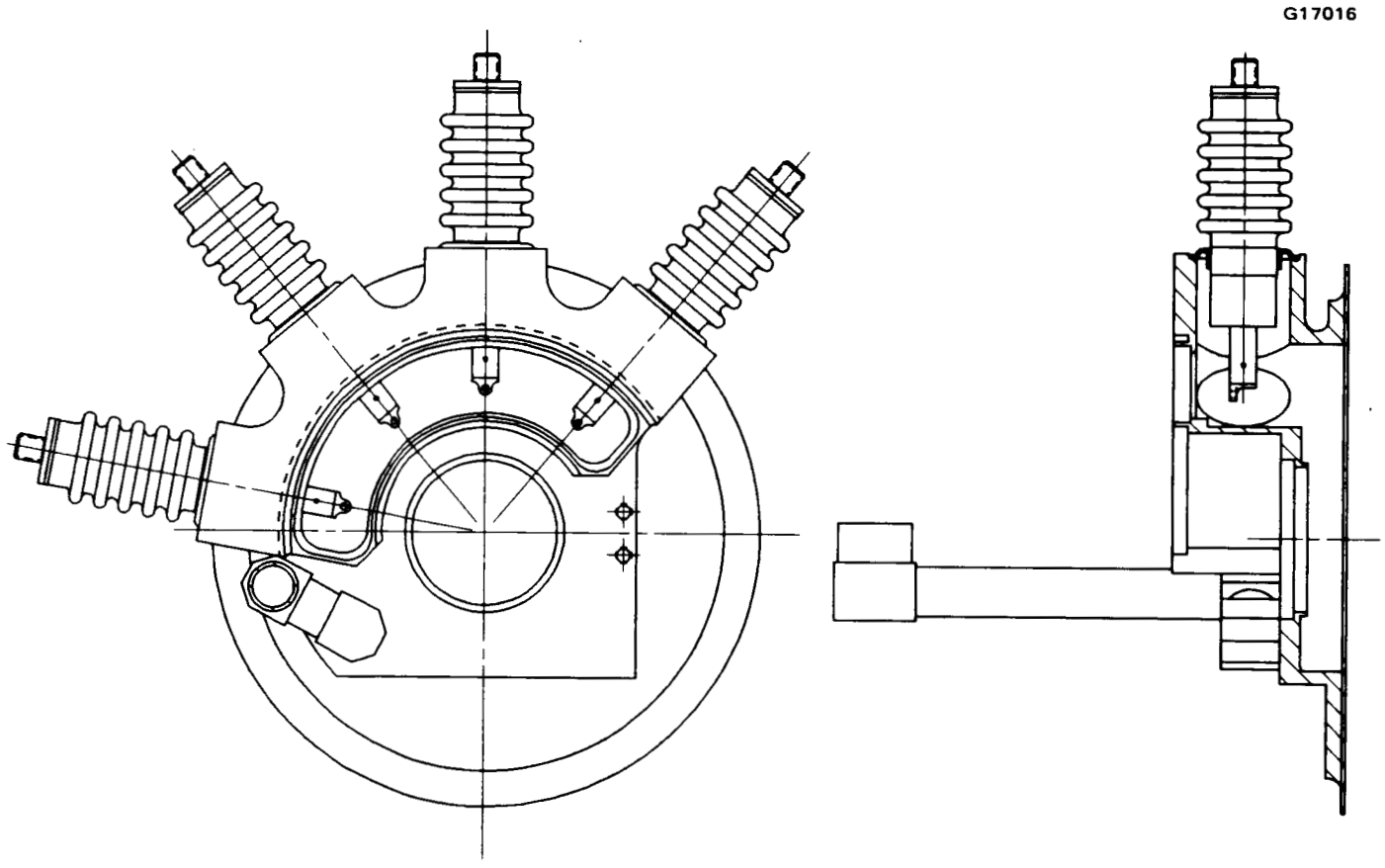

Figure 38 Collector faceplate assembly for the 961H.

complicated machined part designed to locate the terminals relative to the collector leads.

Final assembly of the circuit is accomplished by first welding the face assembly to the end of the circuit. Then, the collector is welded to the back of the faceplate at the large welding flange area. Next, the individual collector electrode leads are welded to the center pins of the feedthrough terminals. Finally, the access to the lead wires at the front of the faceplate is closed by welding on the annular segment cover. A drawing of the completed assembly including the electron gun is shown in Figure 39. Note that the drift section beyond the output circuit coupler was required to allow room for the terminals and to maintain access to the focusing magnets in that region. Although this assembly was quite complicated with several critical weld joints, the fabrication proceeded with no significant problems.

3.2.3 Electron Gun

The 262B isolated anode electron gun for the 961H is constructed in a conventional manner for high-voltage guns. A mechanical layout of the gun is shown in Figure 40. The internal gun assemblies are mounted in concentric, tapered cylinders, which are welded to the external weld flanges brazed to the ceramic insulators. The cathode and focus electrode assembly is attached at the top of the gun stem. The heater return is also run to the top through a separate weld flange. The anode is connected midway down the insulator cylinder so that it is isolated for high voltage from the tube body as well as the cathode, allowing the tube current to be completely cut off by the anode. The only unique feature of this gun is that the anode and anode support are made of iron to magnetically shield the cathode.

3.2.4 Package

As mentioned above, completion of the vacuum envelope is accomplished by welding the electron gun and collector to the RF circuit. The appendage ion pump and the exhaust tubulation are also attached by RF brazing at this final assembly. A drawing of the bakeout assembly is shown in Figure 39. The

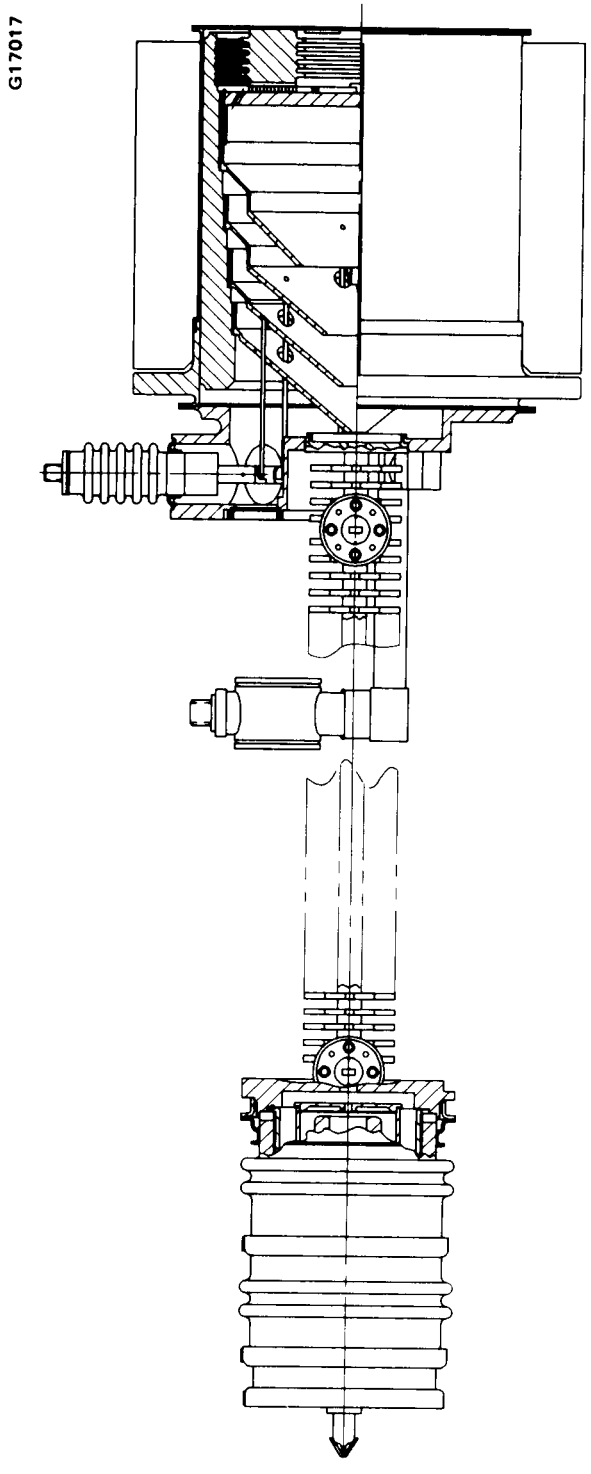

Figure 39 The 961H vacuum assembly.

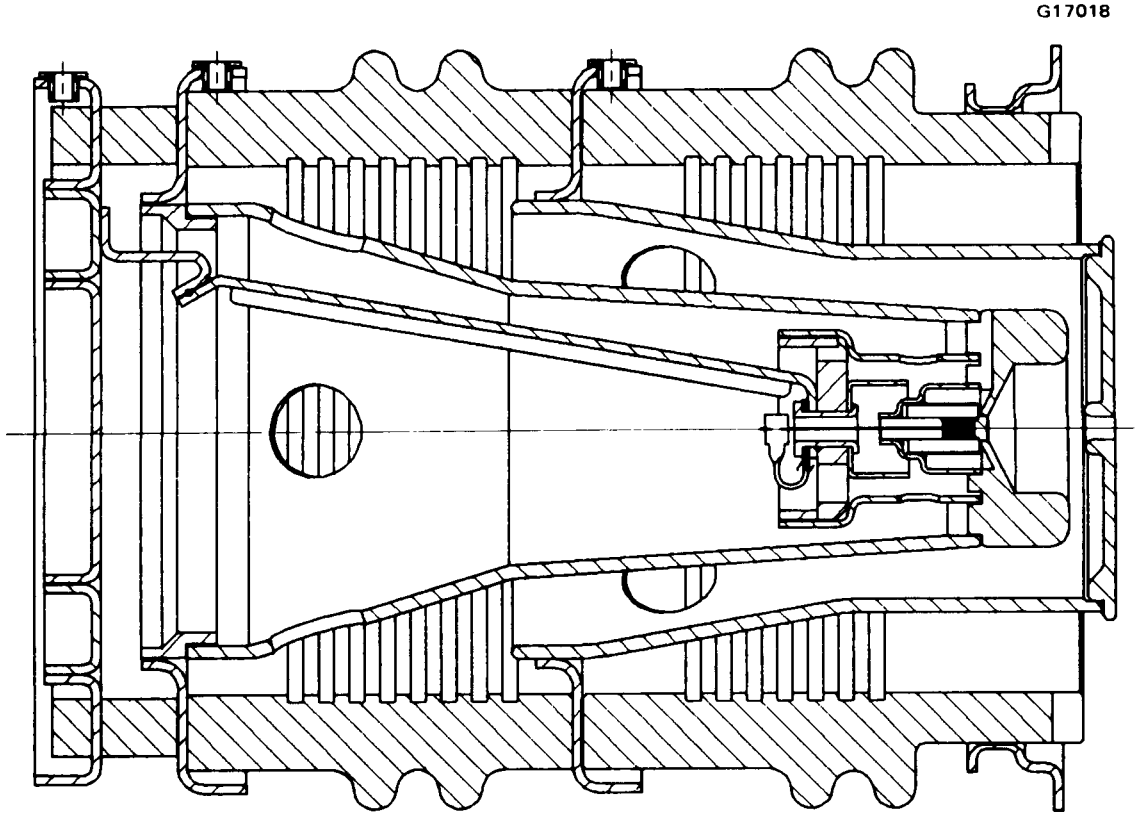

Figure 40 The 262B electron gun assembly used on the 961H.

circuit is broken away in this drawing to shown the location of the 0.2-liter/second appendage ion pump.

Figure 41 shows the completed experimental model tube prior to bakeout. The tube is resting on the collector end, and the package baseplate and window brackets are attached temporarily at this time to support the circuit structure.

After bakeout, the exhaust tubulation is pinched off and the tube is mounted in a test fixture that supports the tube while the focusing magnets are installed and during initial electrical testing. When the initial tests are completed, the tube is packaged in its final configuration for final testing and shipping. The package consists essentially of a baseplate and mounting brackets to rigidly hold the tube circuit through the various environmental requirements. The baseplate is attached to the collector through isolating standoffs to reduce the amount of heat flowing from the collector to the tube body and the spacecraft. A layout of the tube and package, with the circuit cover removed, is shown in Figure 42. A schematic of the packaged experimental TWT is shown in Figure 43. This TWT weighs approximately 15 pounds.

A photograph of the packaged tube is presented in Figure 44. The collector will be painted white to optimize the heat radiation. This package was designed for laboratory testing and handling. For a final flight model, the package design must be refined to provide support for the electron gun.

E5559

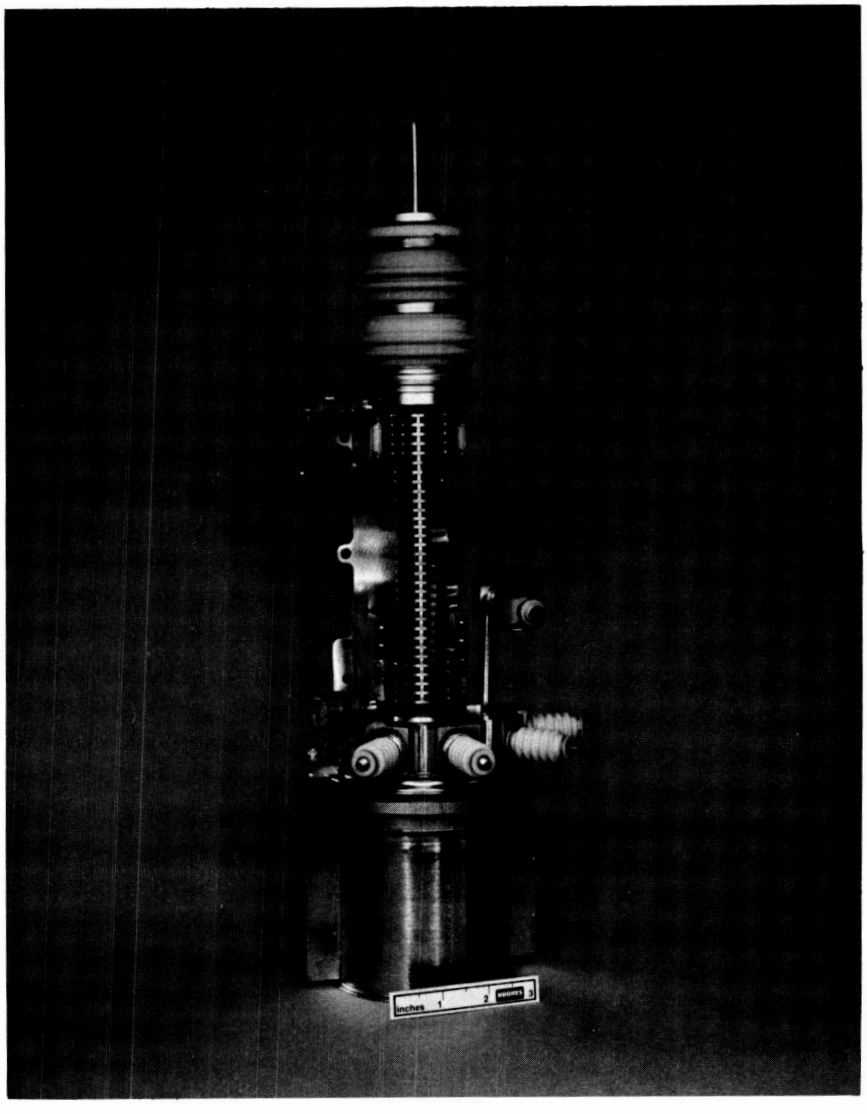

Figure 41 Experimental model prior to bakeout for the 961H.

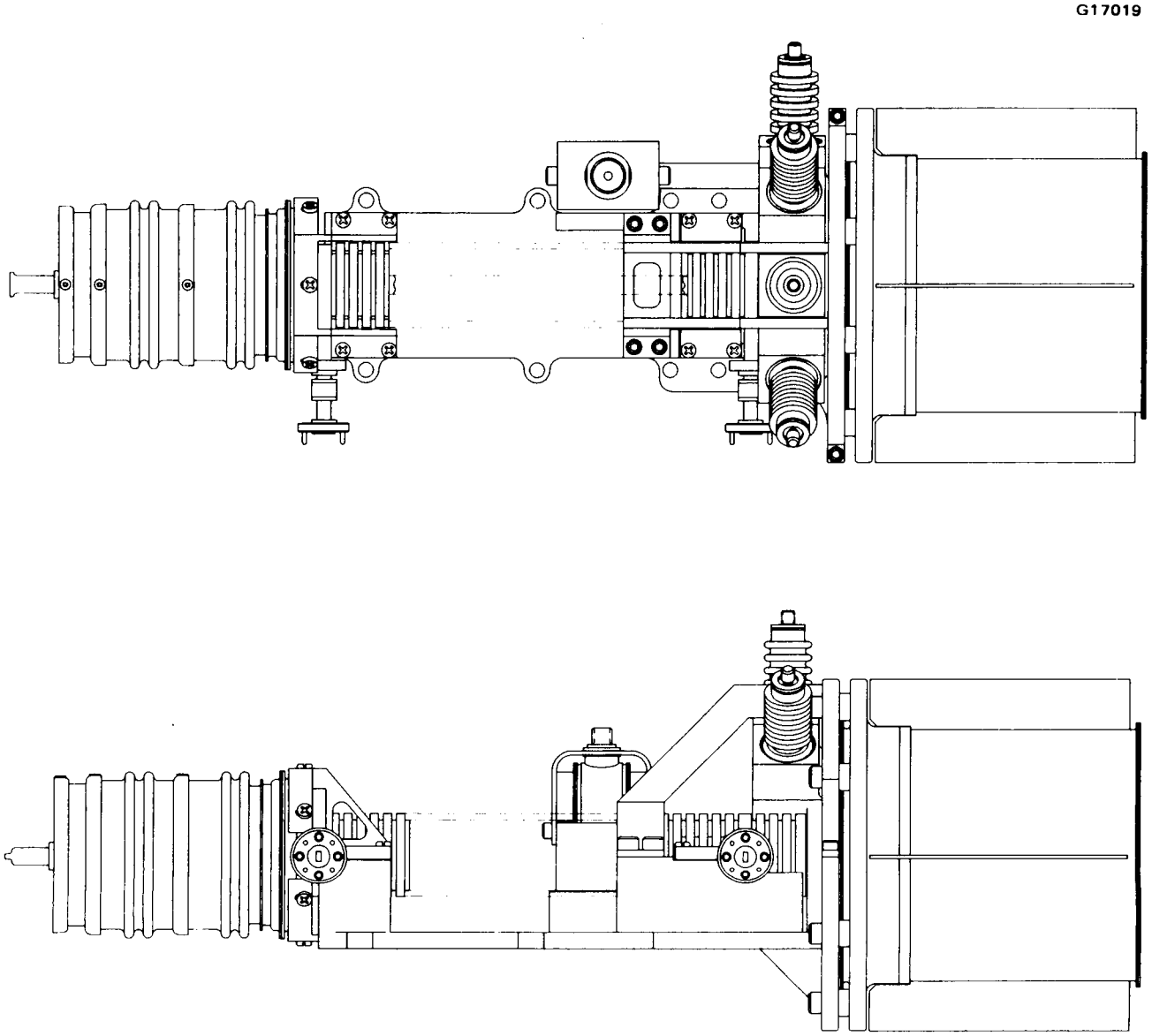

Figure 42 Layout of 961H in final package without the circuit cover.

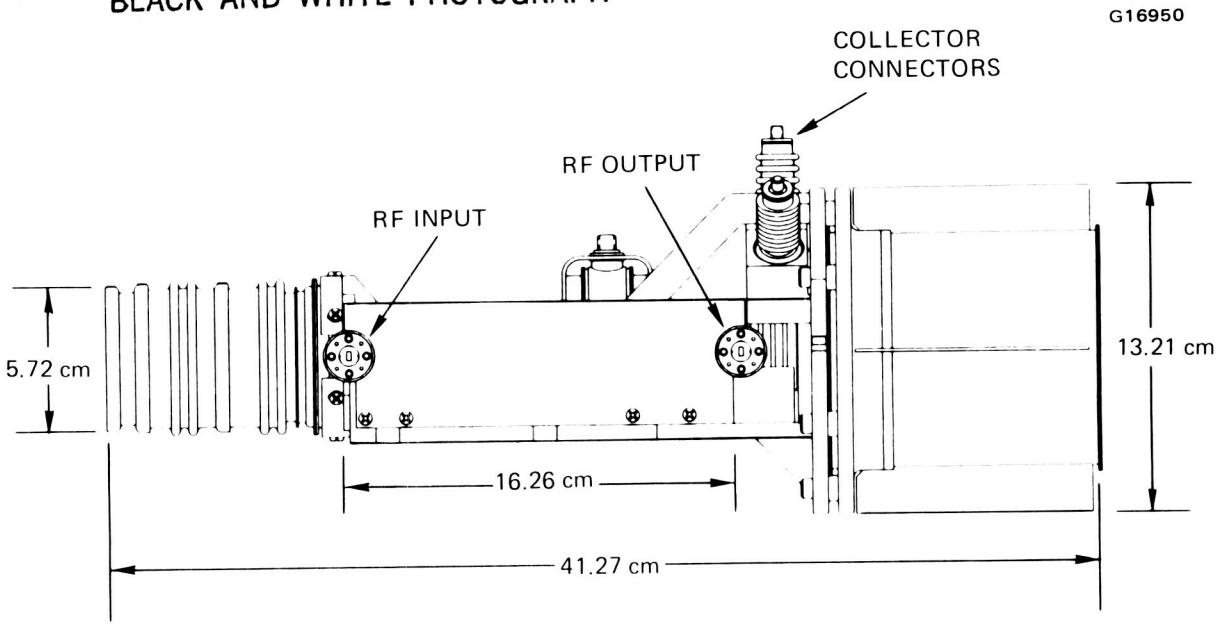

Figure 43 Schematic of packaged 961H experimental TWT.

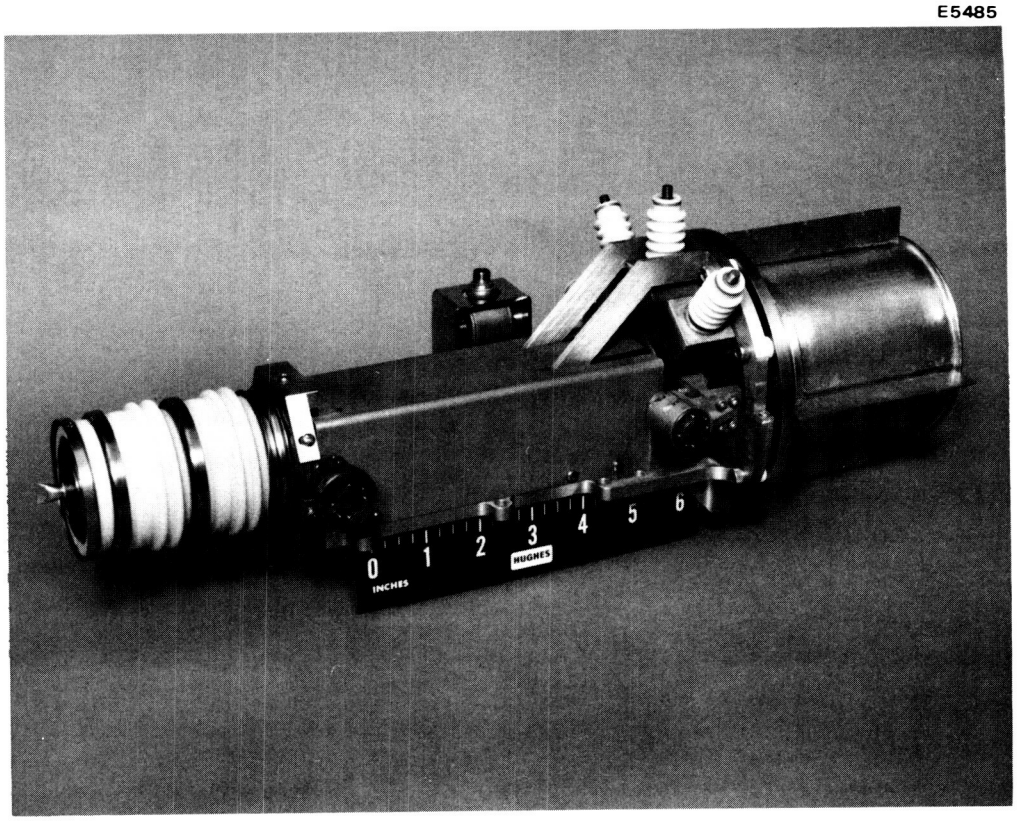

Figure 44 Photograph of conduction cooled body/ radiation cooled collector 961H TWT.

4.0 TWT PERFORMANCE

Two tubes were constructed and tested. The first tube was a feasibility model to demonstrate the basic electrical and RF design approach, and it used a single-stage collector. The second was an experimental model, based on the results of the first tube, that incorporated the multistage depressed collector. Both tubes used the identical RF circuit configuration that was designed to operate over the top half of the objective frequency band.

4.1 FEASIBILITY MODEL

Figure 45 is a photograph of the feasibility model tube mounted in a triangular handling fixture. The isolated anode electron gun is at the right; the single-stage depressed collector is at the left. The focusing magnets have not been installed in the integral pole piece circuit support structure.

Figure 46 shows the tube on the test stand with the focusing magnets and some magnetic shunts installed. The electron gun is at the bottom; the collector is at the top. Auxiliary cooling fins are attached to the collector for thermal dissipation.

Various operating data were obtained under low duty cycle pulsed conditions. The electron gun and beam focusing performance agreed well with the design parameters. At a cathode voltage of -19.5 kV, without RF drive 97 percent beam transmission to the collector was achieved (0.002 A body current out of 0.073 A total cathode current). With RF drive at saturation, the body current increased to only 0.003 A. This was with the collector voltage at body potential. This is excellent beam focusing for a high power MMW TWT.

Two problems were encountered with the 961H feasibility model that prevented it from achieving the full performance expectations. The first was an assembly problem. During the circuit braze, the RF match in the output section deteriorated. The final match of the tube was about 35 to 40 percent voltage reflection across the operating band. Consequently, the tube had relatively large fine grain gain variations and was unstable at higher cathode voltages.

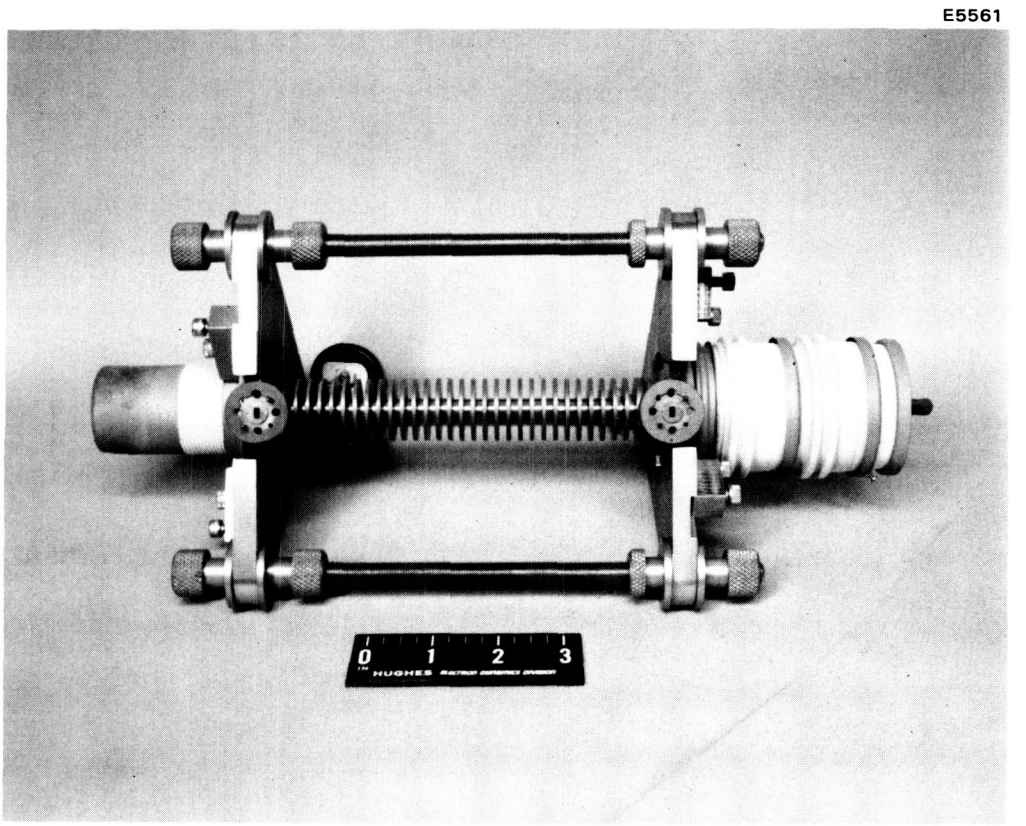

Figure 45 961H feasibility model tube without focusing magnets mounted in triangular support fixture.

E5562

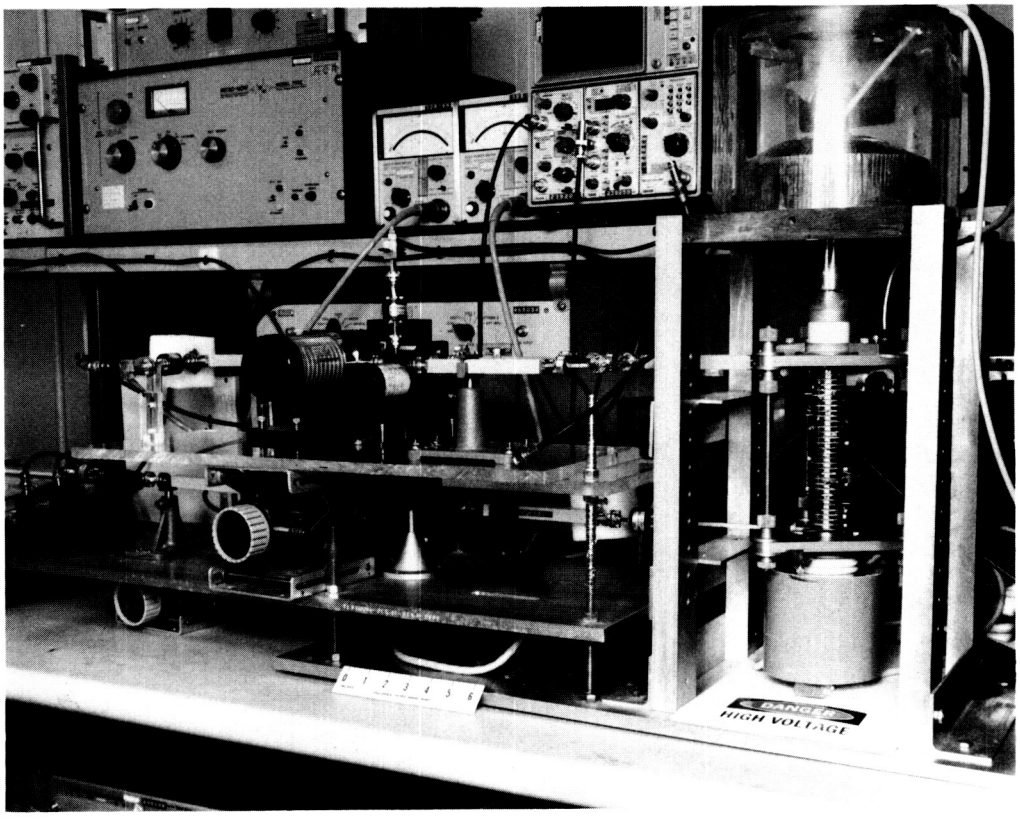

Figure 46 961H feasibility model in electrical tests.

The second problem was related to the basic circuit design. The higher order passband associated with the cavity coupling slot happened to be located in such a frequency range that the phase volocity line at the design operating voltage of 19.7 kV passed exactly through the upper cutoff of the slot mode. This is a high impedance point. Consequently, the tube oscillated (at the slot mode frequency) at the cathode voltage for which it had been designed. Figure 9 shows the phase shift-versus-frequency data for the fundamental operating mode and for the slot mode frequency band with a reference velocity line corresponding to a 19.7 kV beam.

No performance data could be obtained at the design cathode voltage of 19.7 kV because of the slot mode oscillation. Stable performance was achieved at a cathode voltage of 19.3 kV. A graph of swept output power at a constant input drive is shown in Figure 47. Saturated power output performance is shown in Figure 48. The frequency band center is higher than the design because of the lower cathode voltage. However, a very broad bandwidth of over 5 GHz was obtained. The circles indicate saturated power output.

There is a sharp dip in the passband near 65 GHz. This is due to an interaction with the slot mode, which has an upper cutoff at 130 GHz, that prevents the normal gain and efficiency to occur at this subharmonic frequency.

Body current as a function of collector depression voltage is shown in Figure 49. Curves are shown for depression without RF drive and with RF drive at saturation at 64, 66, and 68 GHz. The tube was operated at 1 percent duty cycle.

At cathode voltages above 20 kV, the tube oscillated without RF drive at an oscillation frequency of about 61.5 GHz, where the gain is very high, but it did not seem to oscillate in the slot mode. The regenerative oscillations were due to the poor output circuit match and the high gain at the higher cathode voltage. These oscillations could be driven out with RF input drive.

At a cathode voltage of -20.0 kV, a peak power of over 110 watts was obtained, and the passband shifted down in frequency compared to the -19.3 kV performance.

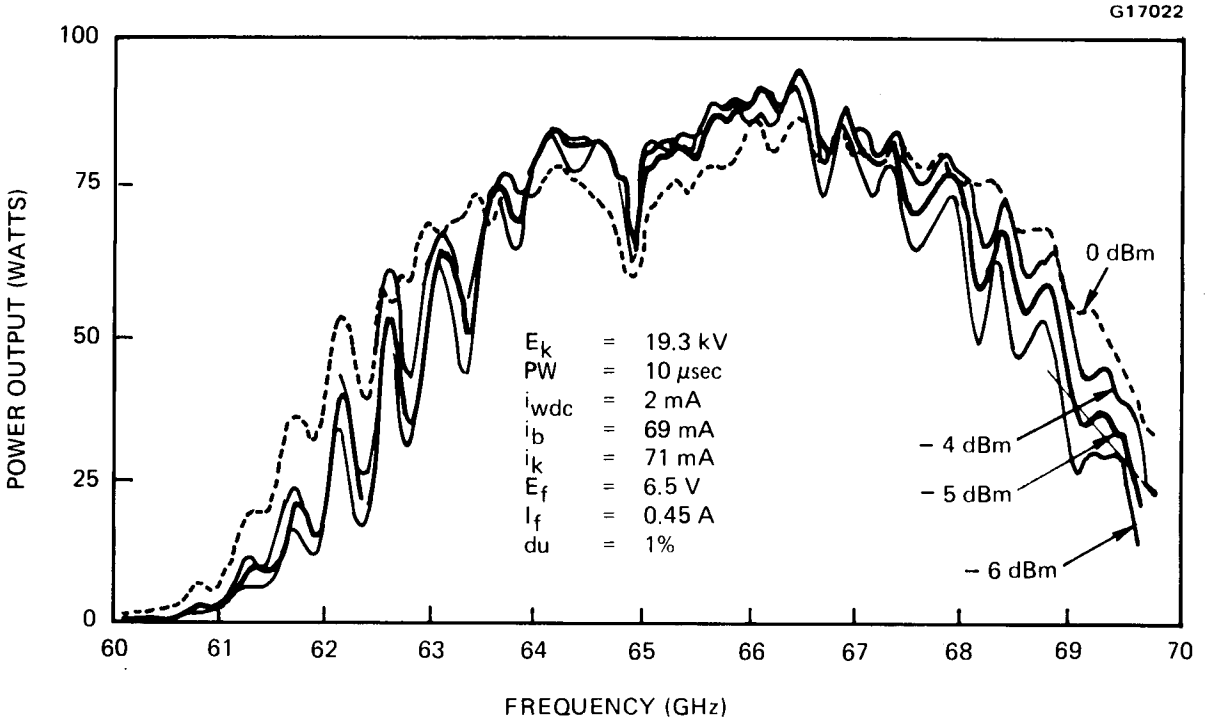

Figure 47 961H S/N 1 power output versus frequency performance.

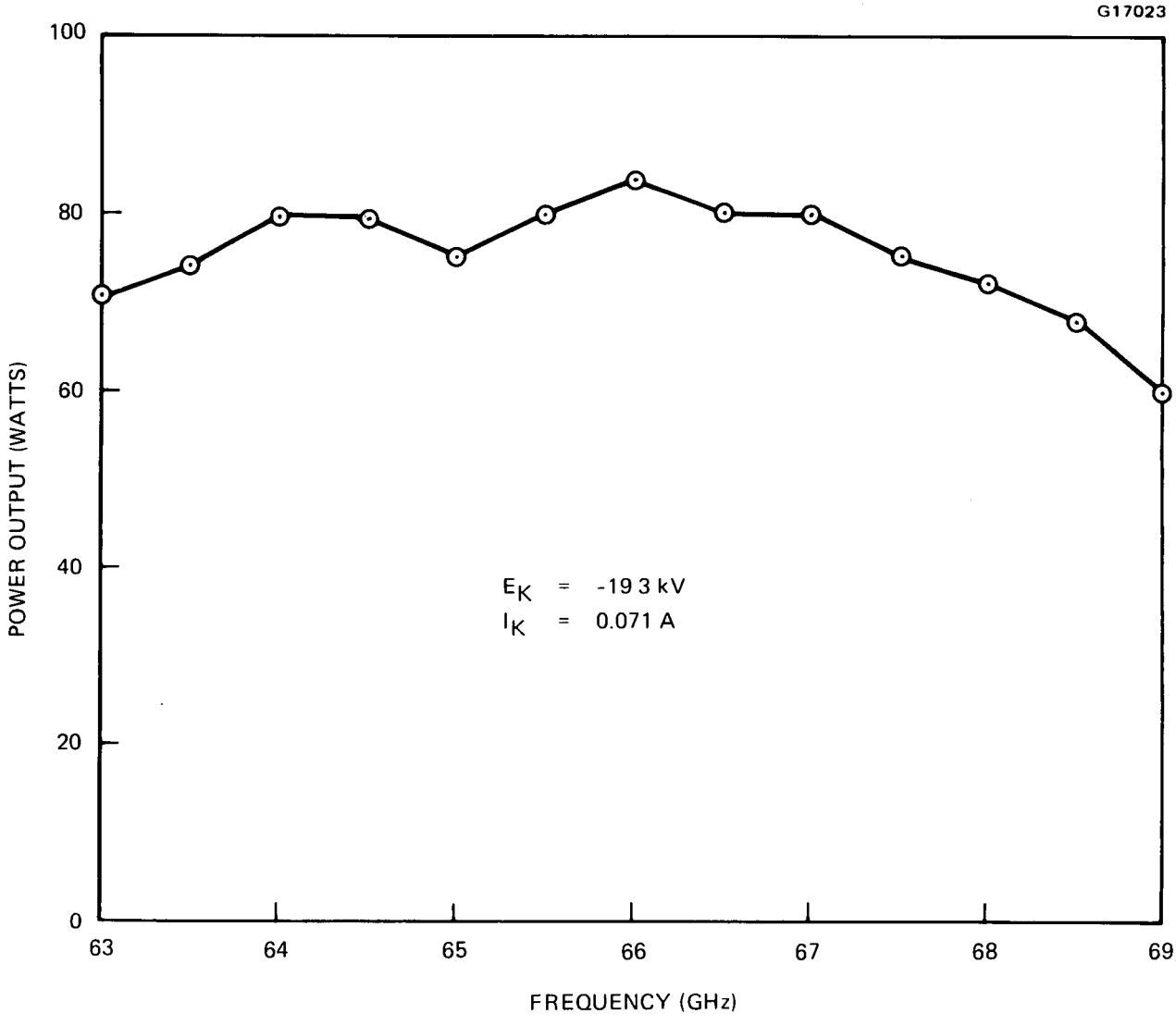

Figure 48 961H S/N 1 saturated power output versus frequency.

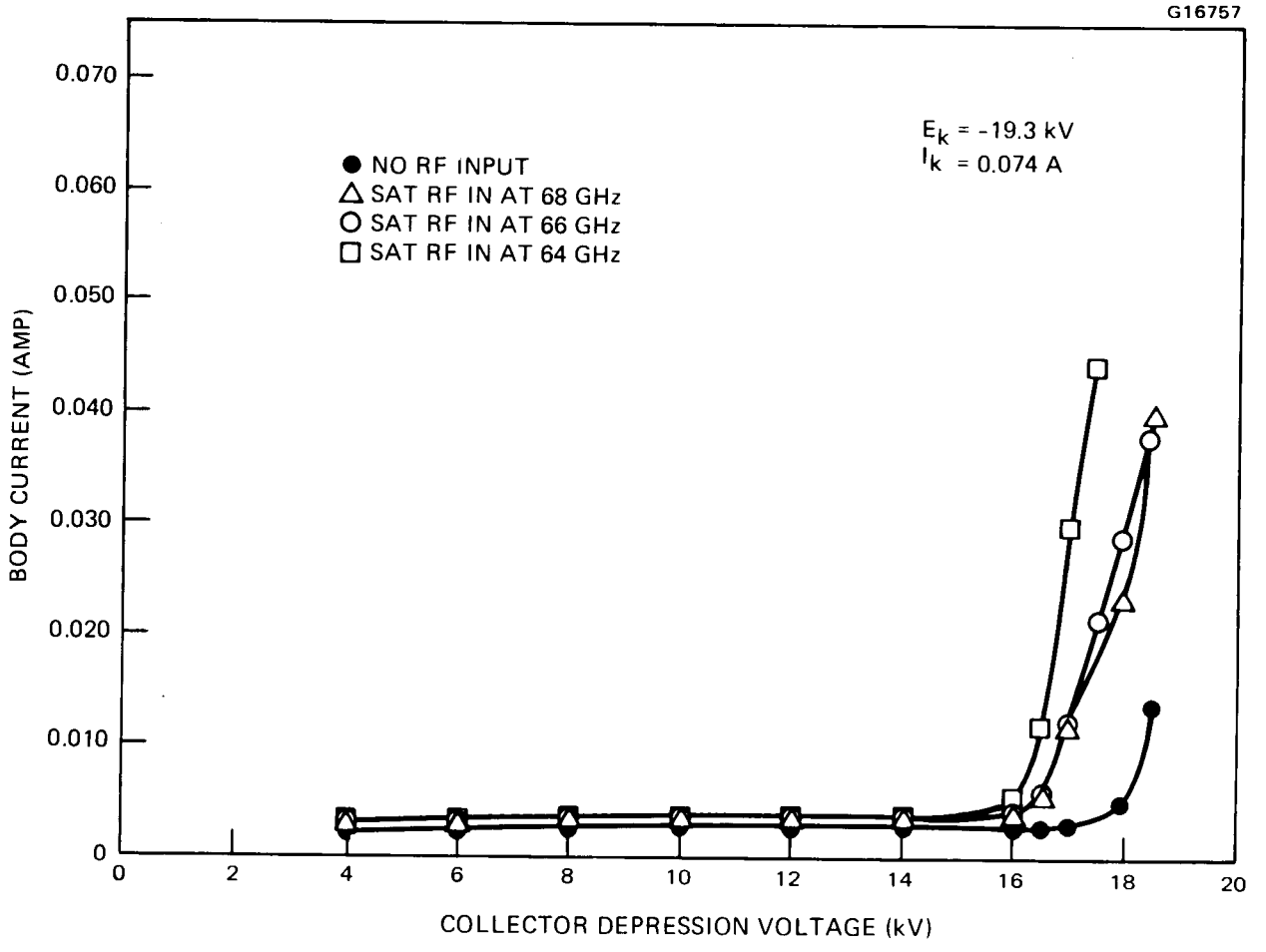

Figure 49 961H feasibility model collector depression characteristics.

Because of the poor circuit match and the high gain, there were large gain variations at this higher voltage.

After the initial low duty cycle, pulsed data were taken to characterize the basic tube performance, the duty cycle was gradually increased to process the tube toward CW operation. The tube was run for several days with the rate of increasing the duty cycle controlled so that the allowable ion pump current would not be exceeded (internal tube gas pressure). If the duty cycle increased too fast, the ion pump current and the tube body current would increase and trip the protective circuitry. The tube was processed to 85 percent duty cycle at a 500 microsecond pulse width with full cathode current at -19.3 kV cathode voltage, but without RF input. During this processing, -11 kV was applied to the collector. Additional aging was still required to allow operation with RF at these high duty cycles. At this point, the tube was turned on CW, with negative anode voltage applied to reduce the beam current and beam power. Figure 50 is a plot of cathode and body currents as a function of anode voltage taken under pulsed condition. The body current was well behaved over the full range of anode voltage from cutoff to full operating beam perveance.

After three days of aging with the anode voltage gradually reduced, the anode voltage reached -2.5 kV with a cathode current of 62 mA (compared to a full cathode current of 74 mA). At this point, the power supply shut down. The fast body current protective circuitry and the ion pump current interlock both fired. When the tube was turned back on with high anode voltage to limit the cathode current, the body current was much higher than it had been. The tube was then checked at low duty cycle pulsed conditions. The beam transmission was very poor; virtually no beam current reached the collector. The circuit had apparently melted, but it was not clear exactly what had happened. The protective circuitry on the power supply was checked and appeared to be operating properly. Since the tube had been running without RF input applied, any damage resulting from beam power interception was expected to occur on the input section of the circuit. However, the RF match of the input section was checked, and it was still very good and appeared unchanged. The RF match of the output section appeared to have degraded, but the match of the output was

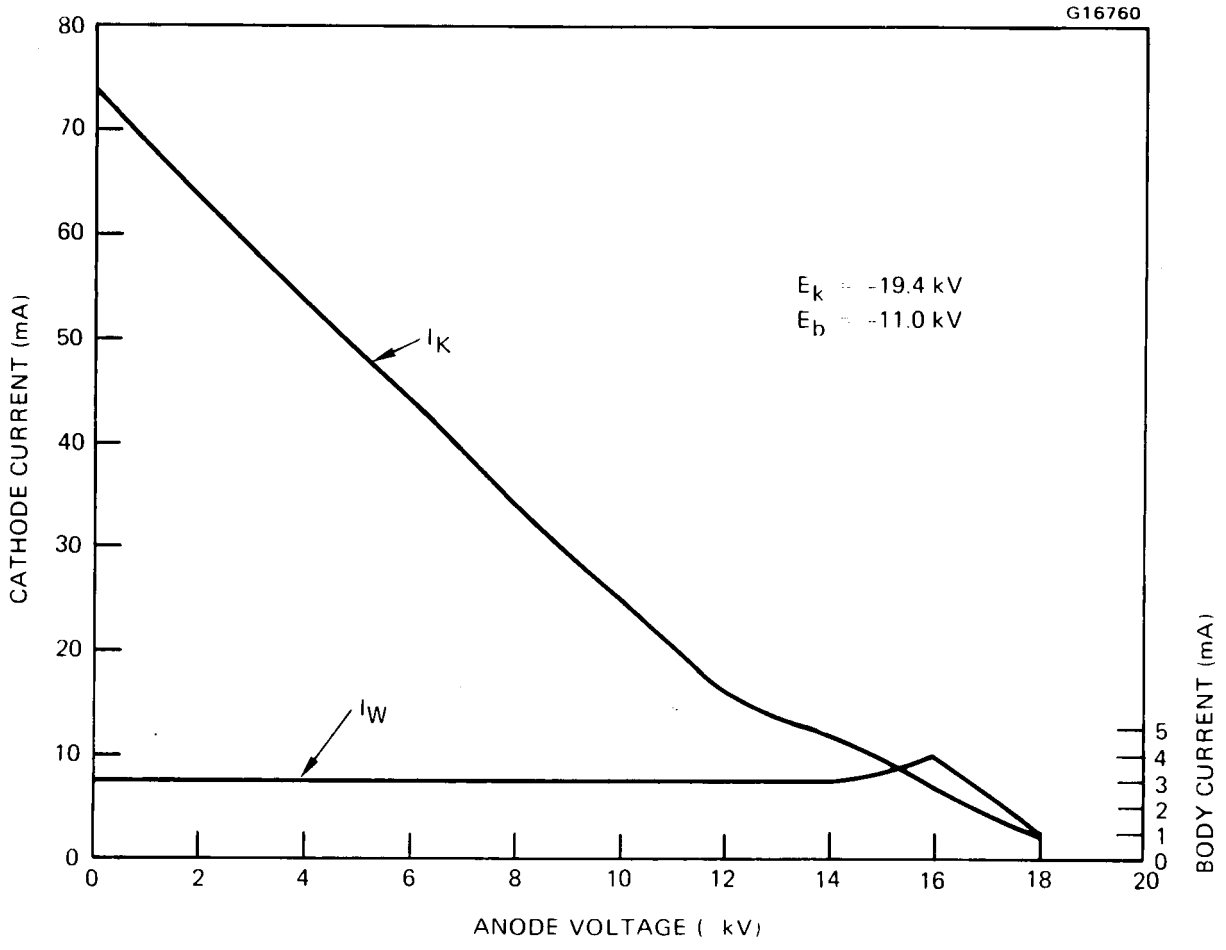

Figure 50 961H feasibility model cathode and body current as a function of anode voltage of E_k = 19.4 kV.

poor after assembly. Consequently, it is difficult to say whether the change was significant.

Attempts to refocus the beam by changing the magnet stack and shunts were unsuccessful. No additional performance data could be obtained on the feasibility mode. The collector was subsequently removed, and the circuit was found to be melted at the output end of the tube.

4.2 EXPERIMENTAL MODEL

Figure 51 is a photograph of the experimental model tube mounted in its rectangular support fixture ready for electrical tests. The focusing magnets are installed.

The circuit assembly proceeded very smoothly for this tube, even though the mechanical construction was more complicated than the feasibility model. The input and output RF matches did not exceed 20 percent voltage reflection coefficient over the operating band, and the elaborate multistage collector assembly also was fabricated with no serious problems.

The basic RF performance agreed well with the feasibility model tube. Because of the improved RF matches, the gain variations were reduced and the tube was more stable. It was stable to -21 kV cathode voltage without RF drive. At -19.7 kV, however, it exhibited the same oscillation problem associated with the slot mode. (S/N 1 and S/N 2 were built to the same RF circuit design.)

The gun perveance of the experimental tube was lower than designed and the beam did not focus as well as in S/N 1. Consequently, the power output was reduced and the depressed collector efficiency performance could not be demonstrated unambiguously. A review of the gun assembly record suggests that the perveance was low because the cathode was set slightly back behind the back edge of the suppressor (focus electrode). A recent computer study of low perveance guns indicates that the cathode to focus electrode position is a sensitive dimension in determining the gun perveance, even if the cathode-to-anode spacing is set correctly. This discrepancy might also explain the focusing difficulty.

Figures 52 and 53 show small signal gain and peak power output versus frequency for the experimental model at a cathode voltage of -19.3 kV. The data were taken at 0.5 percent duty cycle by pulsing the cathode voltage. The cathode current was only 58.8 mA, and the body current without RF input was 6.6 mA.

E5563

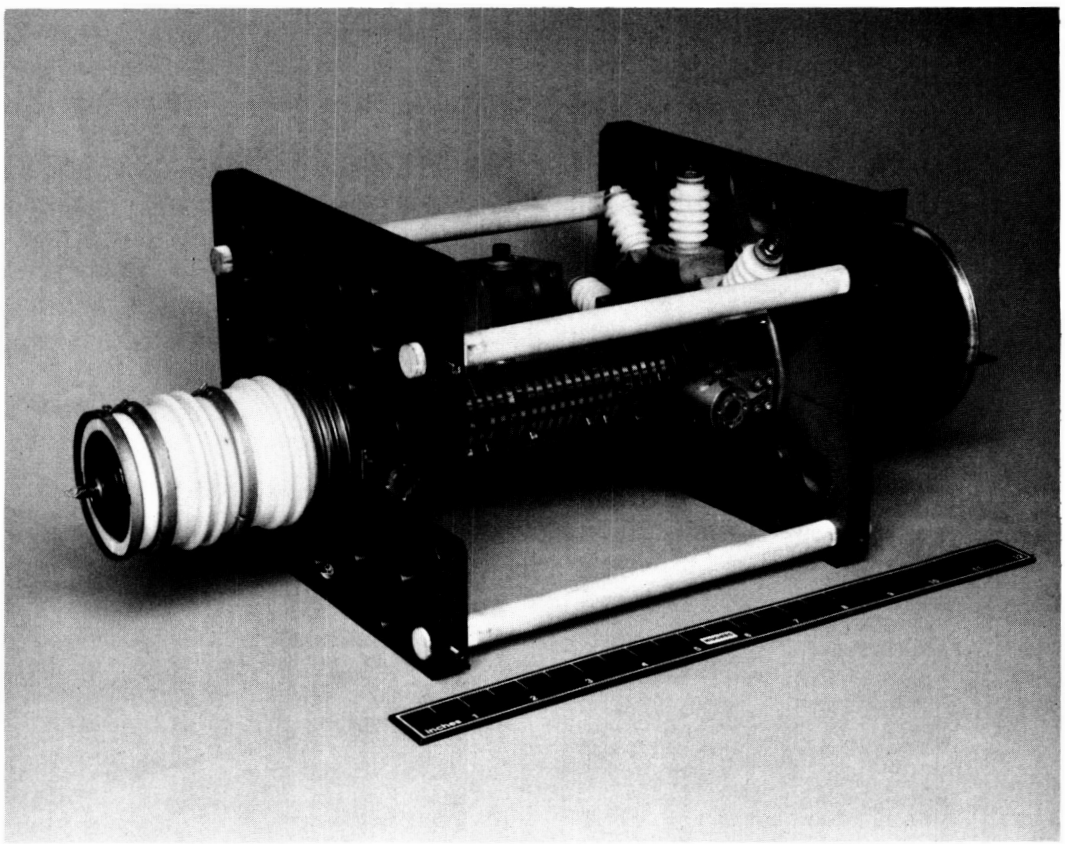

Figure 51 961H experimental model mounted in rectangular support fixture with focusing magnets installed.

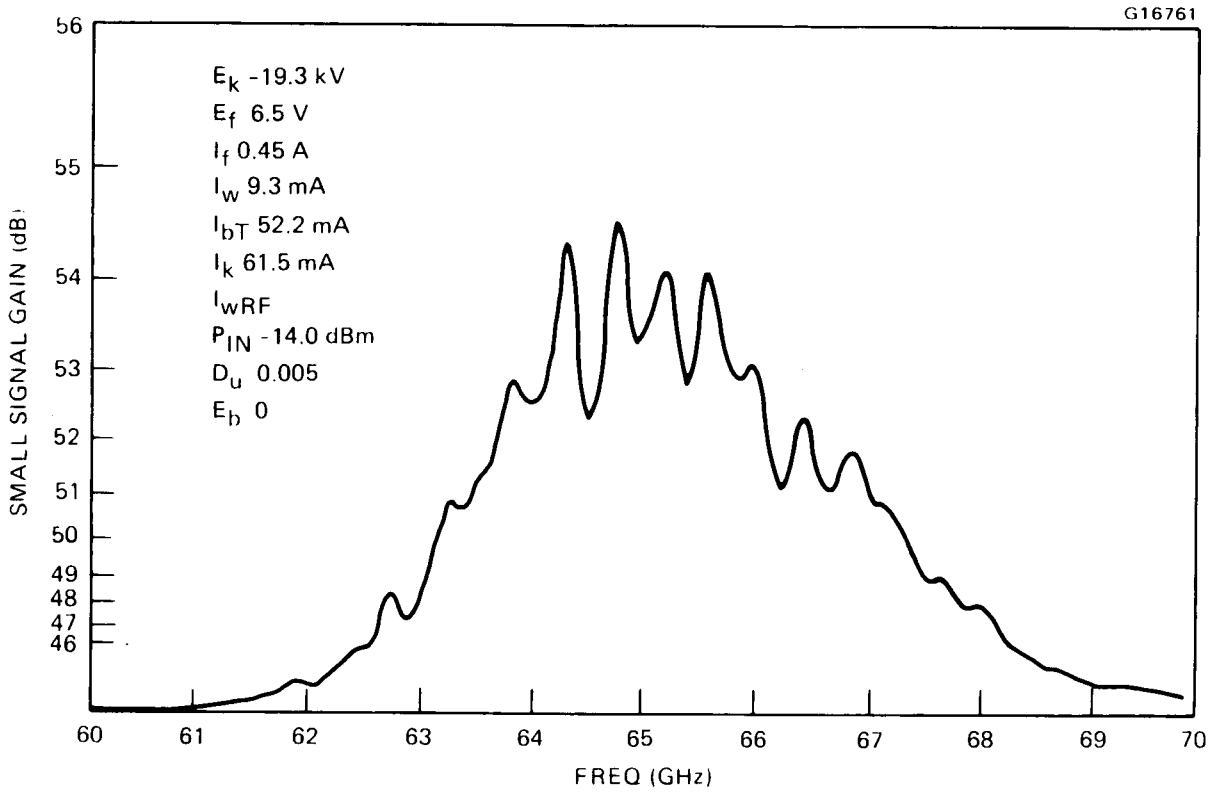

Figure 52 Small signal gain of 961H experimental model at E_k = -19.3 kV.

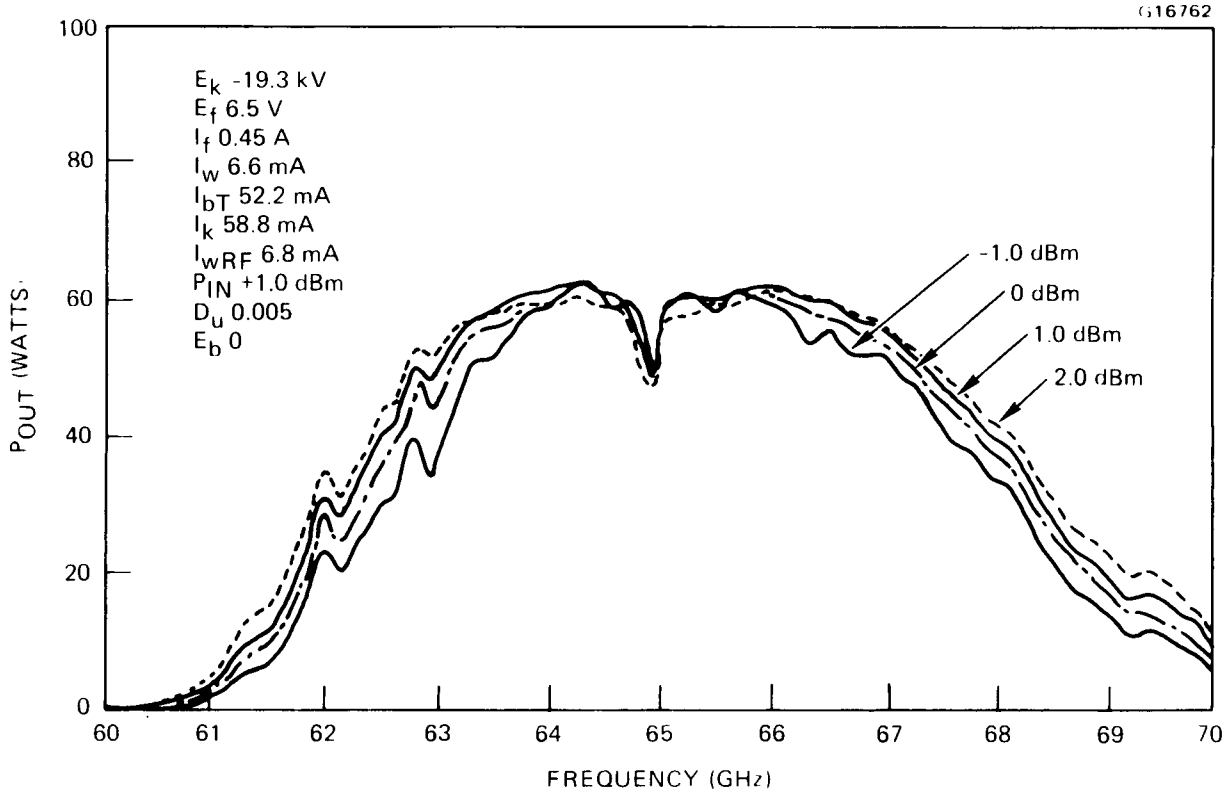

Figure 53 Power output of 961H experimental model with constant RF input at E_k = -19.3 kV.

Figures 54 and 55 show similar data at a cathode voltage of -20.3 kV. The gain is higher and the bandwidth is narrower than at a lower cathode voltage. This power was also lower than that for the feasibility model because of the low perveance and poor focusing. The cathode current was 66 mA, and the body current without RF was 9 mA with the anode at body potential.

At the lower cathode voltage of -19.3 kV, some data were taken with the anode operated at a positive voltage to increase the beam current closer to the design perveance. The transmission did not improve, but the power output increased.

Figure 56 shows power output with the anode voltage at +3000 V at a cathode voltage of -19.3 kV, with beam current of 72.8 mA. Similar data with an anode voltage of +3500 V are shown in Figure 57 with beam current of 74.8 mA.

The output power is not exactly as shown on the swept curves in Figures 52 to 57, because the loss in the test system output leg varied with frequency. Figure 58 shows the calibration correction superimposed on the linear graph, with a single swept curve at a constant RF input of -1 dBm, V_k = -19.3 kV and E_a = +3000 V.

Saturated power output data taken point by point with E_A = +3000 V and E_A = 0 V are shown in Figure 59.

Measurements of collector current distribution were made with various values of collector voltage, to evaluate the performance of the multistage depressed collector at a number of frequencies. These measurements are described at the end of this section.

All of the above tube operation was done at low duty cycle of about 1 percent. Attempts to significantly improve the beam transmission by replacing the magnetic focusing stack were unsuccessful. Since it would have been dangerous to try to run the tube CW with high body current, we decided to attempt to regun the tube using the electron gun from the feasibility model. (That gun had the correct perveance and focused well on the feasibility tube before the circuit was damaged.) Unfortunately, a vacuum leak developed in the gun stem when it was removed from the feasibility tube, so it could not be used.

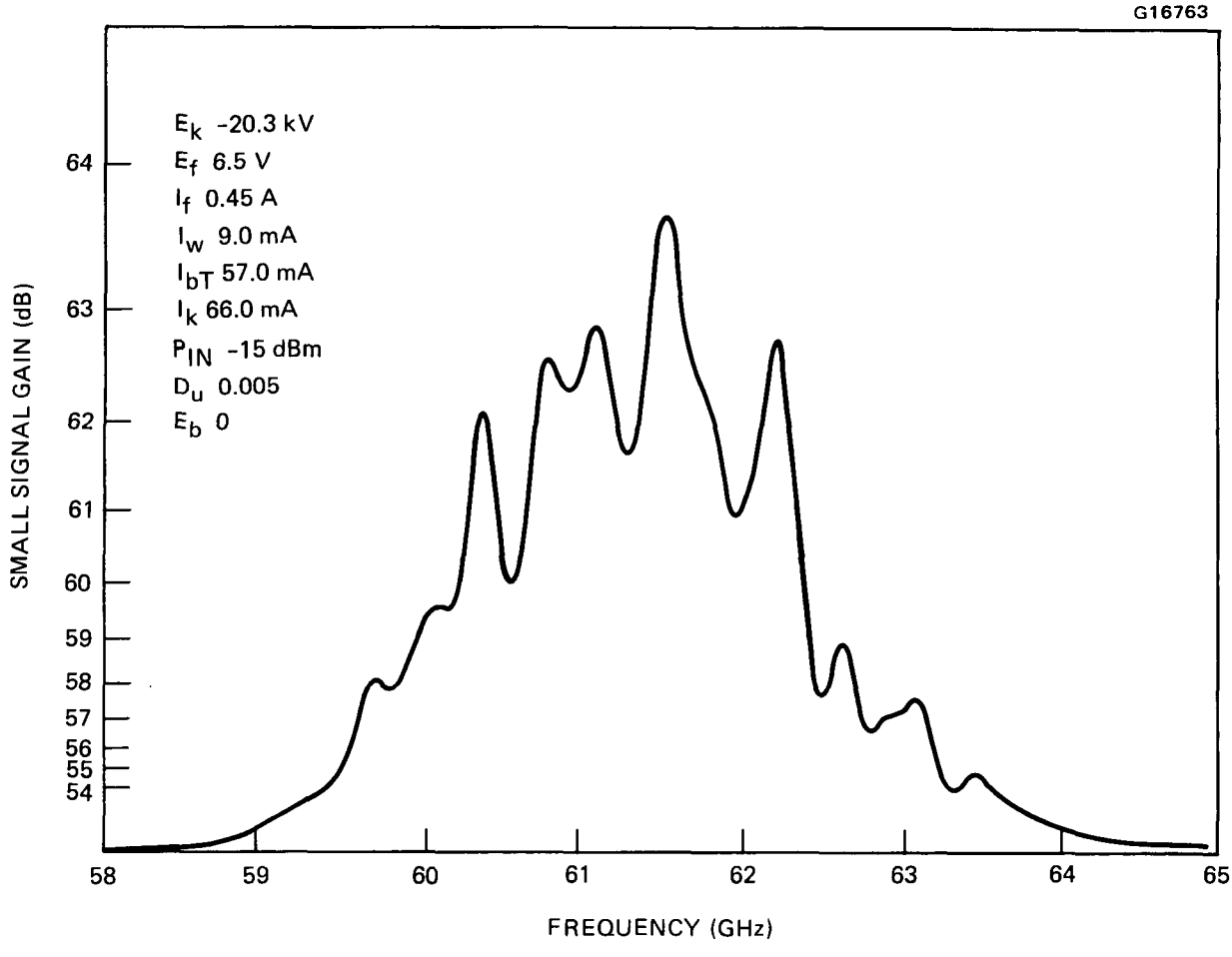

Figure 54 Small signal gain of 961H experimental model at E_k = -20.3 kV.

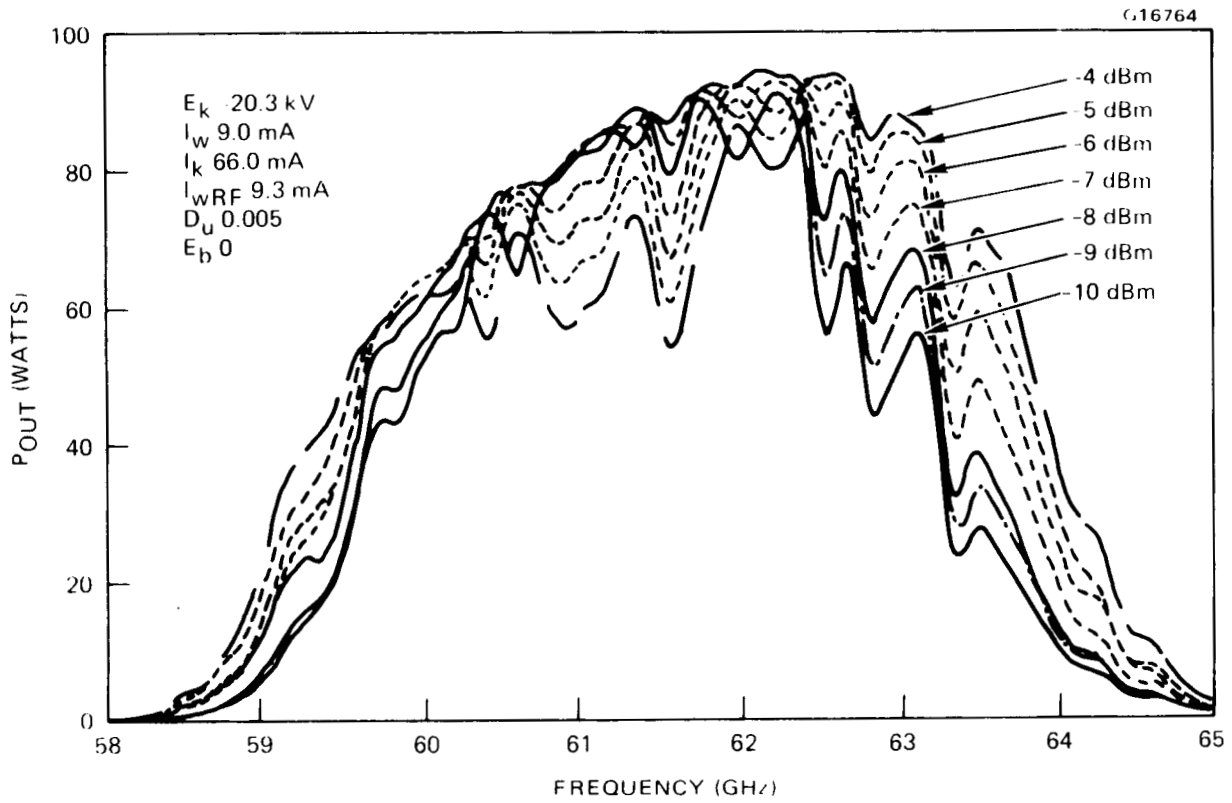

Figure 55 Swept power output of 961H experimental model at E_k = -20.3 kV.

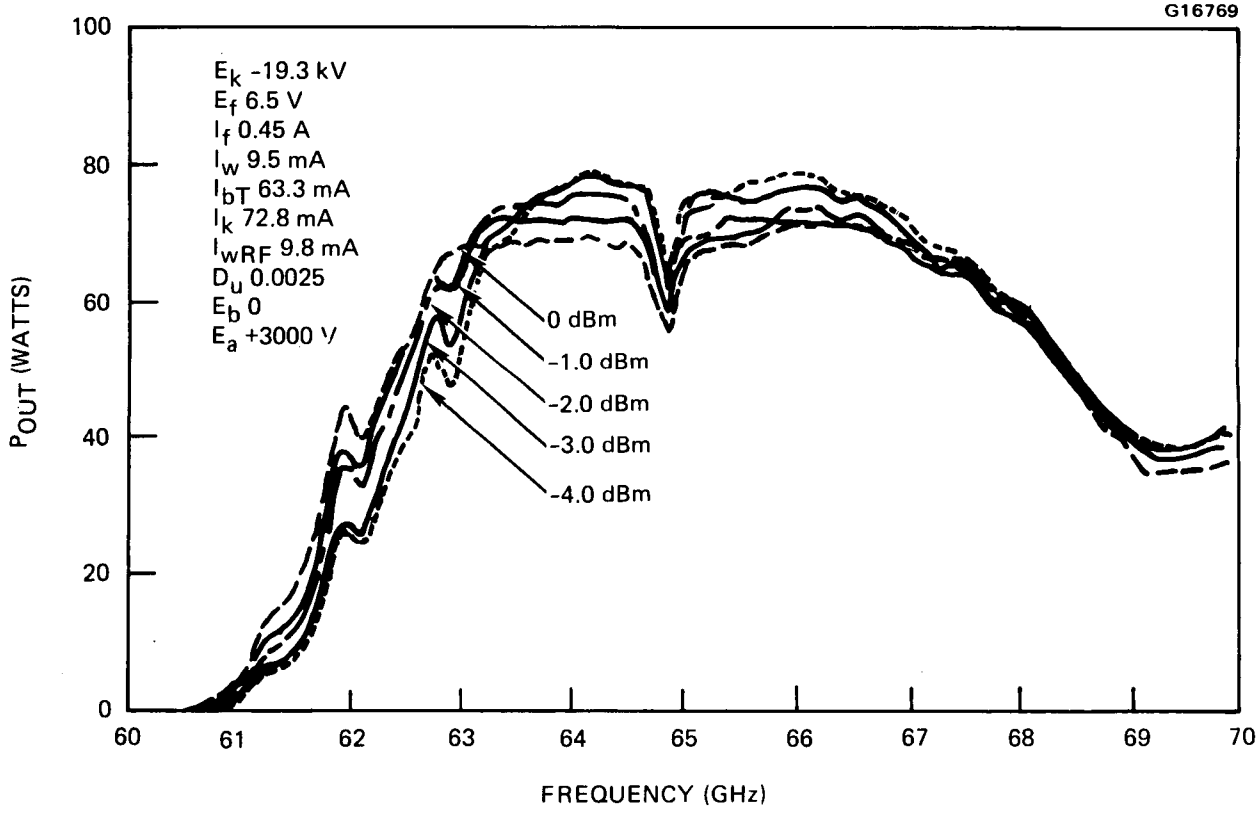

Figure 56 Swept power output at E_k = -19.3 kV, E_a = +3000 V.

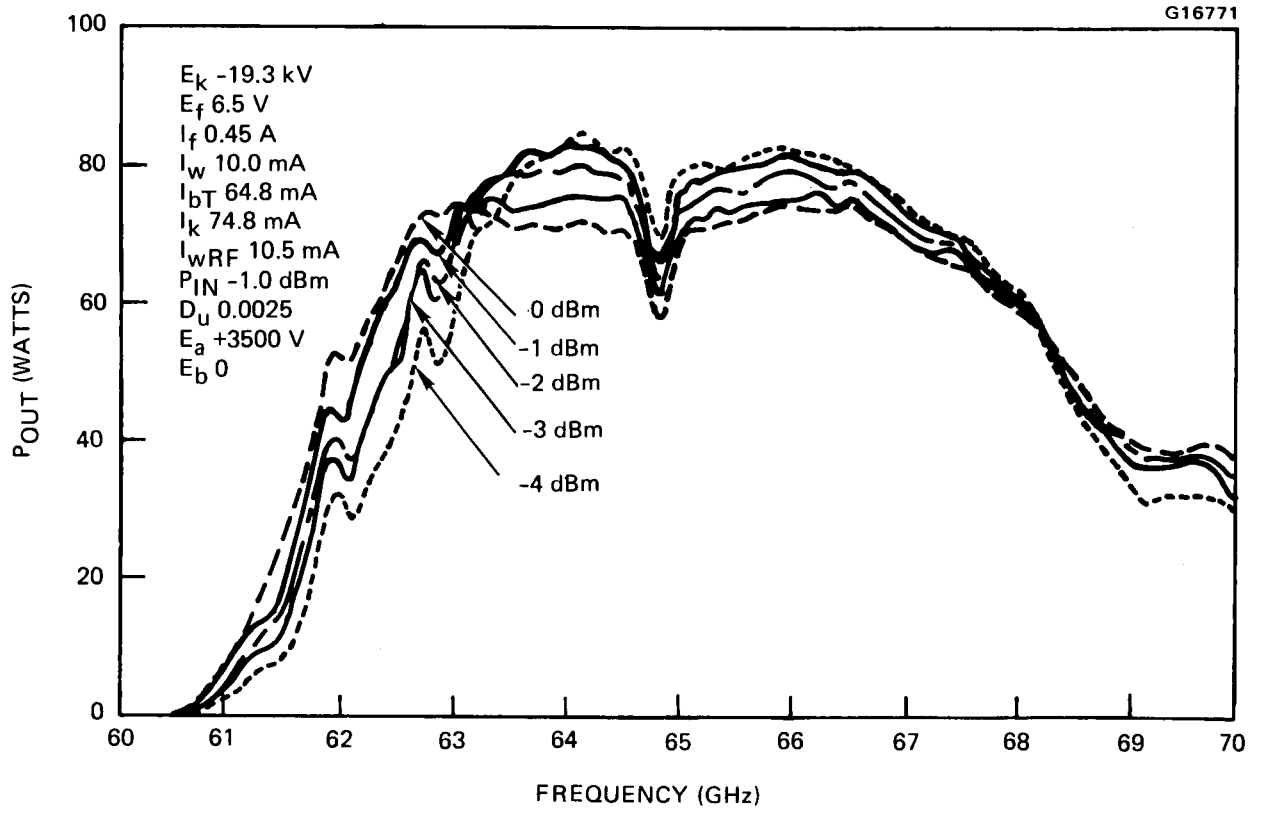

Figure 57 Swept power output at E_k = -19.3 kV, E_a = +3500 V.

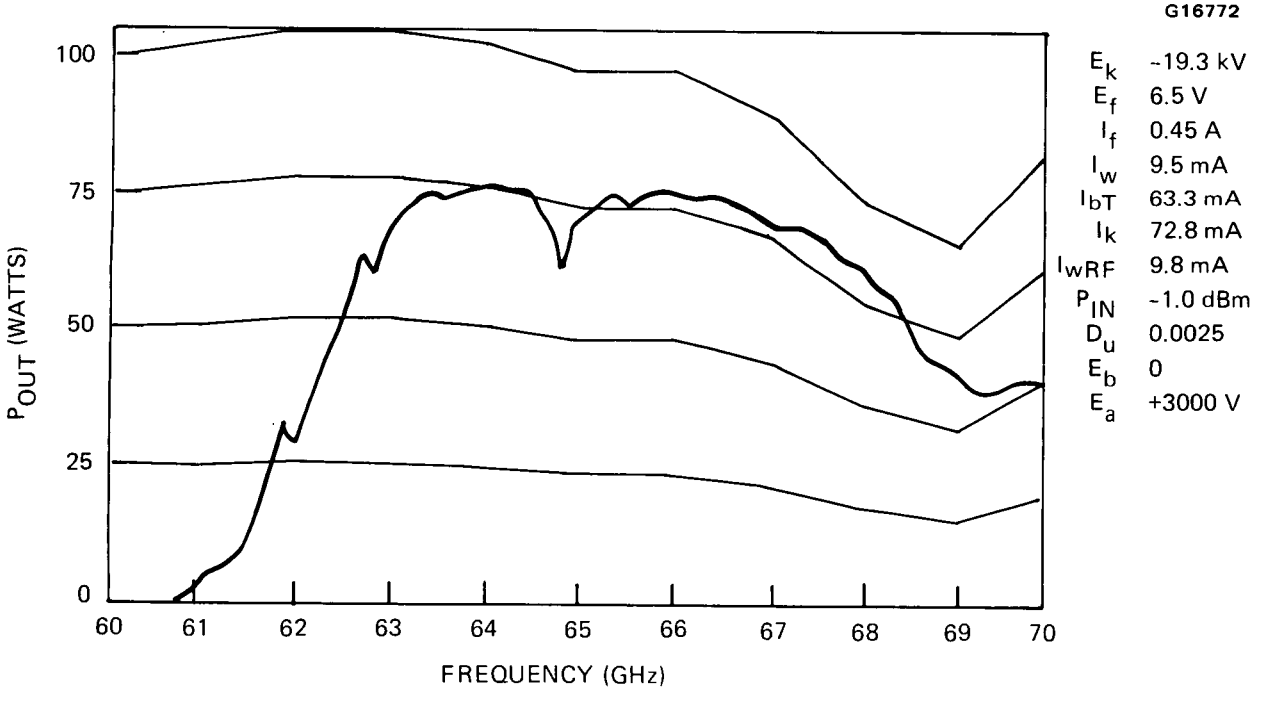

Figure 58 Swept power output at E_k = -19.3 kV, E_a = +3000 V.

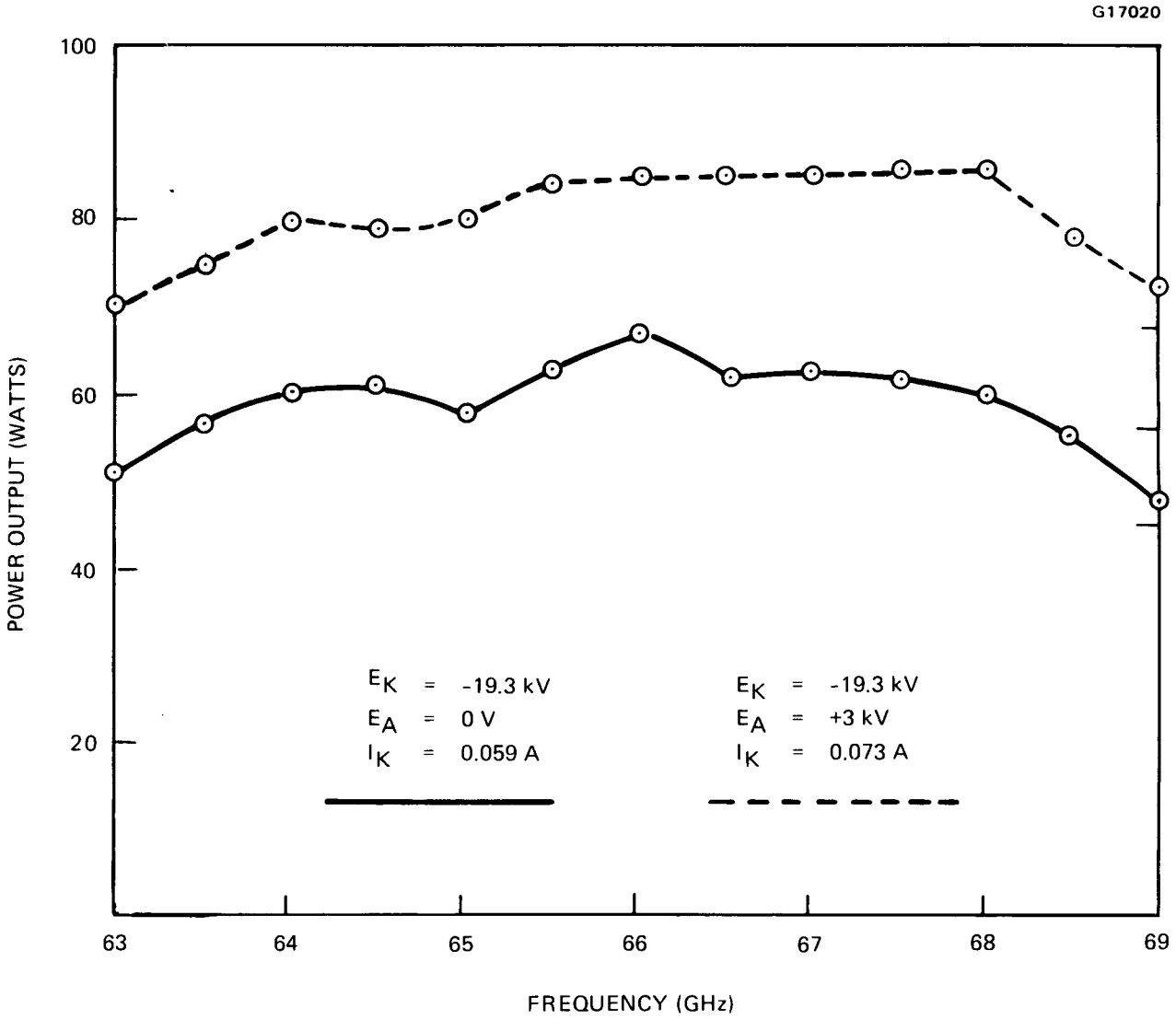

Figure 59 Saturated power output versus frequency.

Therefore, the experimental model was later regunned with a new electron gun. The new gun had higher perveance and much better focusing than the original engineering model gun. The beam transmission was very good. The body current without RF or collector depression voltages was 2 milliamperes. Figure 60 shows preliminary, low duty cycle curves of power-out versus frequency with constant input power at a cathode voltage of -19.3 kV. The collectors were tied together electrically and operated at body potential.

Only a small amount of low duty cycle data was obtained (including, however, a preliminary evaluation of the collector performance). We planned to age the tube and increase the duty to a point where the calibrations would be more accurate and we could take more extensive performance measurements.

The duty cycle was gradually raised to 30 percent by increasing the repetition rate of the cathode modulator without RF applied. The collector voltages were applied to reduce collector heating. Unfortunately, a test failure occurred at this point. At 30 percent duty cycle, one of the samarium cobalt focusing magnets at the output coupler became dislodged. The protective circuitry shut down the modulator power supply. However, this circuitry apparently did not operate fast enough to prevent circuit damage.

After shutdown, the magnet was replaced. The beam transmission had degraded; it could not be improved to the low body current that had originally been achieved (the lowest body current that could be obtained after extensive reshunting was 7 mA, compared to 2 mA before the shutdown). Also, the reflection coefficient looking into the output coupler increased to about 50 percent at one point in the passband. These changes imply that the output circuit structure had been damaged by the intercepted beam current during the shutdown.

The focusing with RF was even worse, so that no additional useful RF operating data could be obtained. Attempts were made to run the tube CW without RF. However, the duty cycle could not be operated above 25 percent without the body current running away. Therefore, tests on the tube were discontinued. It was packaged for delivery as a model.

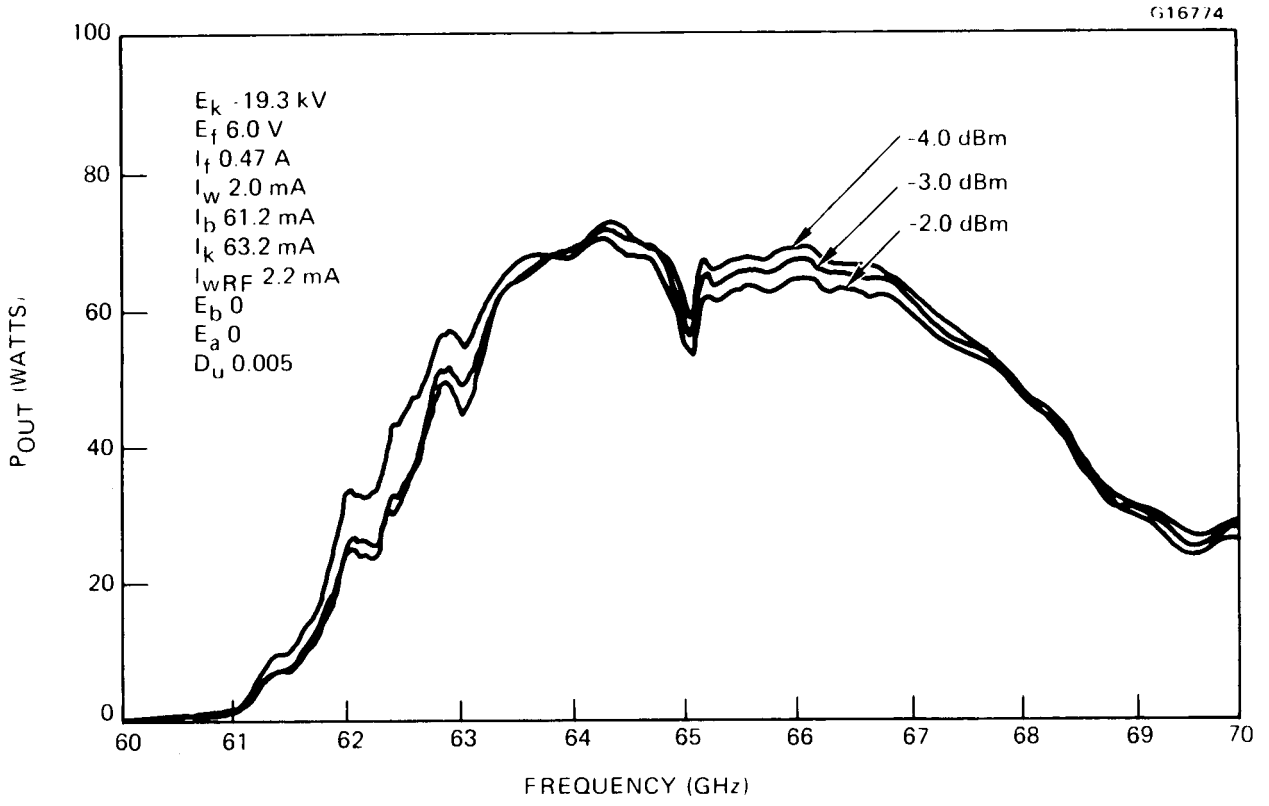

Figure 60 Regunned experimental tube swept power output versus frequency at E_k = -19.3 kV.

Multistage Collector Performance

The four-stage collector on the experimental model TWT was evaluated with two different electron guns. The first gun had poor focusing and low perveance, while the second gun had excellent focusing but was still low in perveance (although somewhat higher than the first gun). In both cases, collector data were only taken with zero anode voltage, so that the saturated output power as well as the basic efficiency were lower than could have been obtained with a positive anode voltage and higher beam current.

With the first gun, data were taken with a cathode voltage of -19.3 kV at 63, 65.5, and 68 GHz. Some effort was made to improve the basic beam transmission without depresson by focusing adjustments. As a result, the original body interception without depression of 15.8 percent with no RF and 16.3 percent with saturated RF was lowered to 11.9 and 12.4 percent, respectively.

Several sets of collector voltages were evaluated. It was found that the collector performed best when the first two stages were operated at the same potential. Table VI summarizes the best performance. The depression voltages were 77.7 percent of the cathode voltage for stages 1 and 2, 88.1 percent for stage 3, and 95.9 percent for stage 4. The body current at all three frequencies was 8.0 mA, or only 0.8 mA higher than without depression. If the second stage was depressed more than the first, the body current was typically 9.0 mA, or an additional 1 mA higher. Because of poor beam transmission, the maximum overall efficiency was only 21.7 percent, at a basic efficiency of 5.88 percent. The estimated collector efficiencies varied between 90.3 and 90.6 percent at the three frequencies.

With a second gun on the tube, and much improved beam transmission (96.6 percent dc and 96.3 percent with RF), the collector data were repeated, this time at a cathode voltage of -19.4 kV. Since the tube was operated pulsed, and we fully expected to achieve CW operation later, only a basic matrix of collector data was taken with no attempt at fine tuning the performance. Table VII shows the data, while Figure 61 displays the basic and overall efficiencies versus frequency. At 65.5 GHz, with a saturated output of 77.1 W and a basic

TABLE VI

COLLECTOR PERFORMANCE OF THE 961H S/N 2 WITH FIRST GUN

Cathode voltage, E_k (kV)	-19.3	-19.3	-19.3
Frequency, f (GHz)	63.0	65.5	68.0
Output Power, P_{out} (W)	56.4	66.4	61.2
Collector voltage, (kV)			
Stage 1	-15.0	-15.0	-15.0
2	-15.0	-15.0	-15.0
3	-17.0	-17.0	-17.0
4	-18.5	-18.5	-18.5
Collector current (mA)			
Stage 1	3.6	5.2	5.4
2	16.3	19.5	20.0
3	21.4	17.0	13.0
4	9.5	8.8	11.5
Body current[(a)], I_w (mA)	8.0	8.0	8.0
Cathode current, I_k (mA)	58.8	58.5	57.9
Beam power (W)	1135	1129	1117
Recovered power (W)	838	822	815
Basic efficiency, η_o (%)	4.97	5.88	5.48
Overall efficiency, η (%)	19.0	21.7	20.2
Collector efficiency, η_c (%)	90.5	90.6	90.3

(a) Without depression, I_w = 7.2 mA at all three frequencies.

Without RF drive, I_w = 6.9 mA without depression,

I_w = 7.9 mA with depression.

TABLE VII

COLLECTOR PERFORMANCE OF THE 961H S/N 2 WITH SECOND GUN

Cathode voltage, E_k (kV)	-19.4	-19.4	-19.4
Frequency, f (GHz)	63.0	65.5	68.0
Output Power, P_{out} (W)	68.6	77.1	60.5
Collector voltage, (kV)			
Stage 1	-15.5	-15.5	-15.5
2	-15.5	-15.5	-15.5
3	-17.0	-17.0	-17.0
4	-18.0	-18.0	-18.0
Collector current (mA)			
Stage 1	9.5	12.0	11.9
2	24.3	25.3	23.1
3	13.8	10.0	8.4
4	14.5	14.3	17.9
Body current[(a)], I_w (mA)	3.1	3.3	3.7
Cathode current, I_k (mA)	65.2	64.9	65.0
Beam power (W)	1265	1259	1261
Recovered power (W)	1020	1006	1008
Basic efficiency, η_o (%)	5.42	6.12	4.80
Overall efficiency, η (%)	28.0	30.4	23.9
Collector efficiency, η_c (%)	90.0	90.0	88.7

(a) Without depression, I_w = 2.4 mA at all three frequencies.

Without RF drive, I_w = 2.2 mA without depression,

I_w = 2.9 mA with depression.

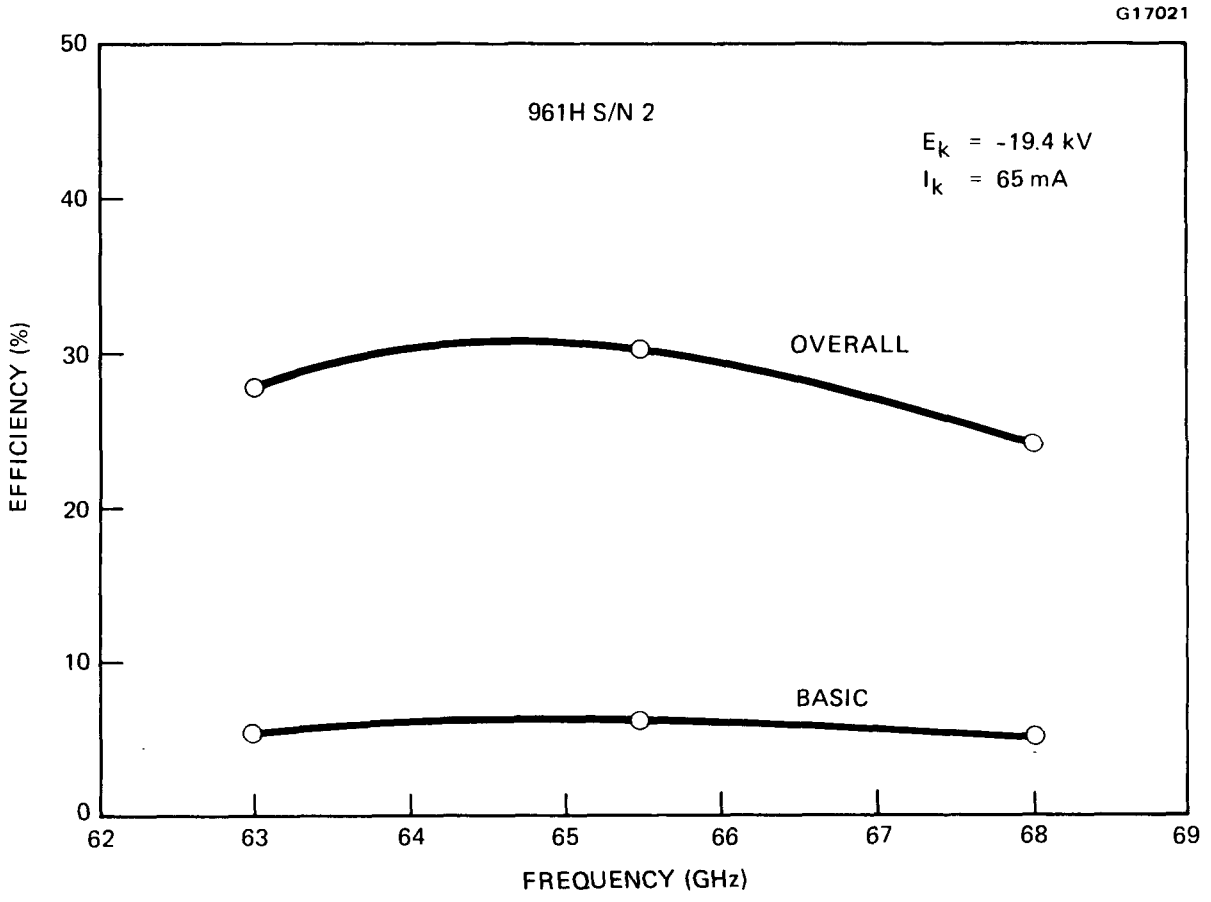

Figure 61 Efficiency at saturation of 961H S/N 2.

efficiency of 6.1 percent, the depressed efficiency was 30.4 percent. If the heater power (2.8 W) is included, the overall efficiency becomes 30.1 percent. The collector efficiency was 90.0 percent. It is likely that the collector performance would have improved by empirical adjustments of the magnetic field, both on the RF circuit and in the drift section beyond the output coupler. With the second gun, almost no adjustments were attempted.

The following commments may be made about the design and performance of the 961H collector.

1. The small aperture of the first stage, its short distance to the pole piece, and the large depression voltage create a relatively strong electric lens. The trajectory angles beyond the first stage will then depend on the first stage operating voltage. It was observed, for example, that the current to the last two stages consistently increased as the depression voltage of the first two stages was reduced from -15.5 to -14.5 kV. Ideally, these currents should not change. Furthermore, the strong lens will make the performance very sensitive to any deviation from concentricity of the first stage aperture with respect to the beam axis.

2. The lens effect at the first stage is likely to be partly responsible for the increased backstreaming to body, observed when the second stage was depressed more than the first stage. Although the calculated trajectories behaved well (Figure 22), there are always some low energy electrons that are focused toward the axis. Depressing the second stage will shorten the distance that the slow electrons travel into the collector. Consequently, they may not drift sufficiently far away from the axis to avoid falling back through the aperture.

3. There is no doubt that treatment of the active collector electrode surfaces for low yield secondary emission, such as by texturization or carbon deposition, could significantly improve the collector performance. In particular, the back plate of the last stage would benefit from such treatment.

To achieve collector efficiencies of 95 percent, the strong electrostatic lens effect at the first stage should be reduced. One possibility is to provide a shield on the front part of the first stage, in such a manner that the inactive depression region (between zero and 80 percent of the cathode voltage) can remain short and the aperture can still be made small.[6] Most likely, it will also be necessary to use low secondary yield surfaces on the electrodes. NASA has reported collector efficiencies well in excess of 90 percent with a carbon coated collector, in a tube with a beam perveance of 0.4 perv and backed off from saturation.[7] The much lower beam perveance in the 961H, and small trajectory angles, would make it easier to obtain high collector efficiency.

5.0 CONCLUSIONS AND RECOMMENDATIONS

Two 961H tubes were designed, built, and evaluated for this program consisting of a feasibility model that used a single-stage collector and an experimental model that incorporated the multistage collector. The RF performance of these tubes was in basic agreement with the electrical design calculations. This demonstrated that a V-band tube using a coupled-cavity interaction circuit could be built at this peak power level with broad bandwidth.

Numerous mechanical design features, particularly those associated with the high-power, multistage, radiation cooled collector, were developed to successfully fabricate the tubes.

There was a problem with an oscillation at the upper cutoff frequency of a higher order mode associated with the circuit coupling slot, which prevented operation at the design cathode voltage. The circuit should be modified to shift the location of the slot mode passband to a range where it cannot interact at the desired operating voltage.

The multistage depressed collector functioned fairly well, but its capability for efficiency enhancement was not fully evaluated because of low gun perveance, poor beam transmission and the limited testing time available before the circuit was damaged in test.

CW operation was not obtained. We believe this failure is related to problems in the testing equipment and procedures, and not a basic thermal limitation of the tube design.

Judging from the encouraging but incomplete test results obtained from the tubes built for this program, it is recommended that a follow-on development effort should be undertaken to refine the TWT design and build additional experimental 961H TWTs to fully demonstrate the design capability and

compliance to the NASA specification. As a minimum, the following modifications should be made to ensure a viable flight model tube:

1. The RF interaction circuit should be adjusted to move the slot mode frequency range. As has been demonstrated, this can be accomplished by changing the shape of the coupling slot.

2. The mechanical design of the electron gun should be modified so that the tube can be packaged to withstand the full space environment requirements.

3. Some modifications to the collector electrode configurations should be made, particularly on the first stage, and electrodes with low secondary emission yield should be used.

APPENDIX A

961H COLLECTOR THERMAL ANALYSIS

TABLE OF CONTENTS

LIST OF ILLUSTRATIONS

A.1 INTRODUCTION

The 961H collector is different than those on most other space-based TWTs in that it must operate at relatively high power levels and dissipate most of its heat via radiation. A thermal analysis of this collector was required to determine if the radiation cooling would be sufficient to keep key components below allowable temperature limits.

This report presents the results of the analysis for representative RF and DC thermal power dissipation levels.

A.2 ANALYSIS TECHNIQUE

The radiation view factors were determined using the RENO computer code. Figure A.2-1 shows the quarter-symmetry model and the employed boundary conditions. Radiation heat transfer between the internal components of the collector is negligible and was not considered. Large, perfectly reflective surfaces were used as boundary planes in the model. The spacecraft surface was also modeled as a large surface (compared to the collector itself) with an emissivity of 0.56. This value was used in a previous thermal analysis of the similar 899H TWT. The external collector surface emissivity level of 0.85 was also obtained from the 899H analysis. An emissivity level of this magnitude was achieved via special paint-like coatings on the exterior collector surfaces.

Although a quarter model was adequate for the radiation view factor analysis, a half model was required for the thermal analysis. A full set of view factors for the thermal model was easily obtained by reflecting the quarter model results about a lateral symmetry plane.

The thermal analysis was performed using the ANSYS finite element code. Basic hidden line views of the model are shown in Figures A.2-2 and A.2-3. Radiation view factors determined in the aforementioned RENO analysis are included in this model via two mode radiation elements (not shown for clarity).

A short section of the output circuit was modeled by computing an equivalent thermal conductivity and area for the numerous circuit components. The circuit magnets were not included in the calculations since previous correlation studies on other TWTs have shown them to be largely ineffective for heat transfer. This is due to the relatively loose fit of the magnets and the resistance of the epoxy used to bond them between the circuit pole pieces. The "free" end of the circuit (the model boundary) was left adiabatic. Leaving the free end adiabatic is a conservative assumption since some heat would probably flow down the circuit, thereby producing slightly lower temperatures than would be predicted by the finite element model. Although

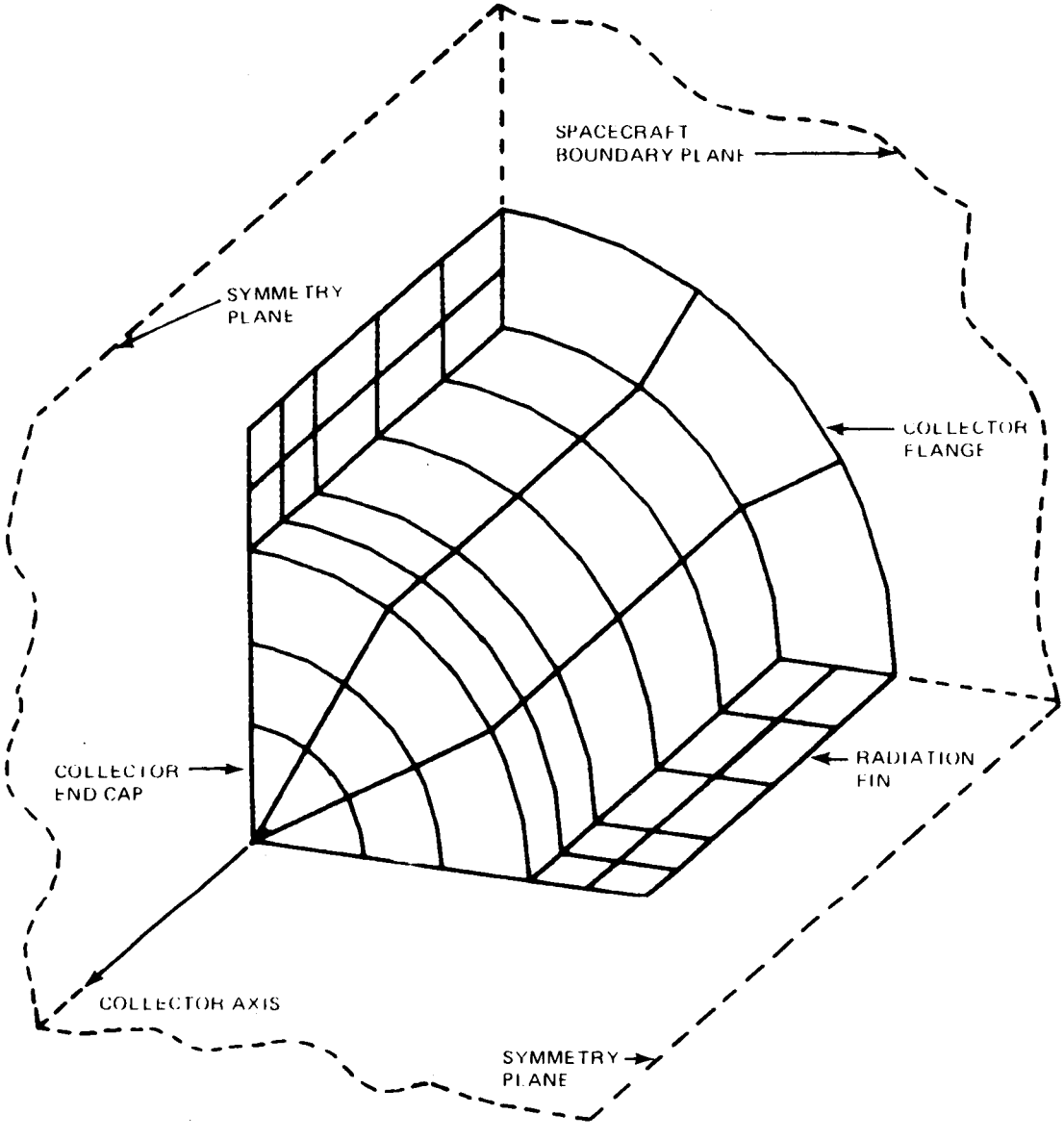

Figure A.2-1 Reno quarter symmetry radiation model.

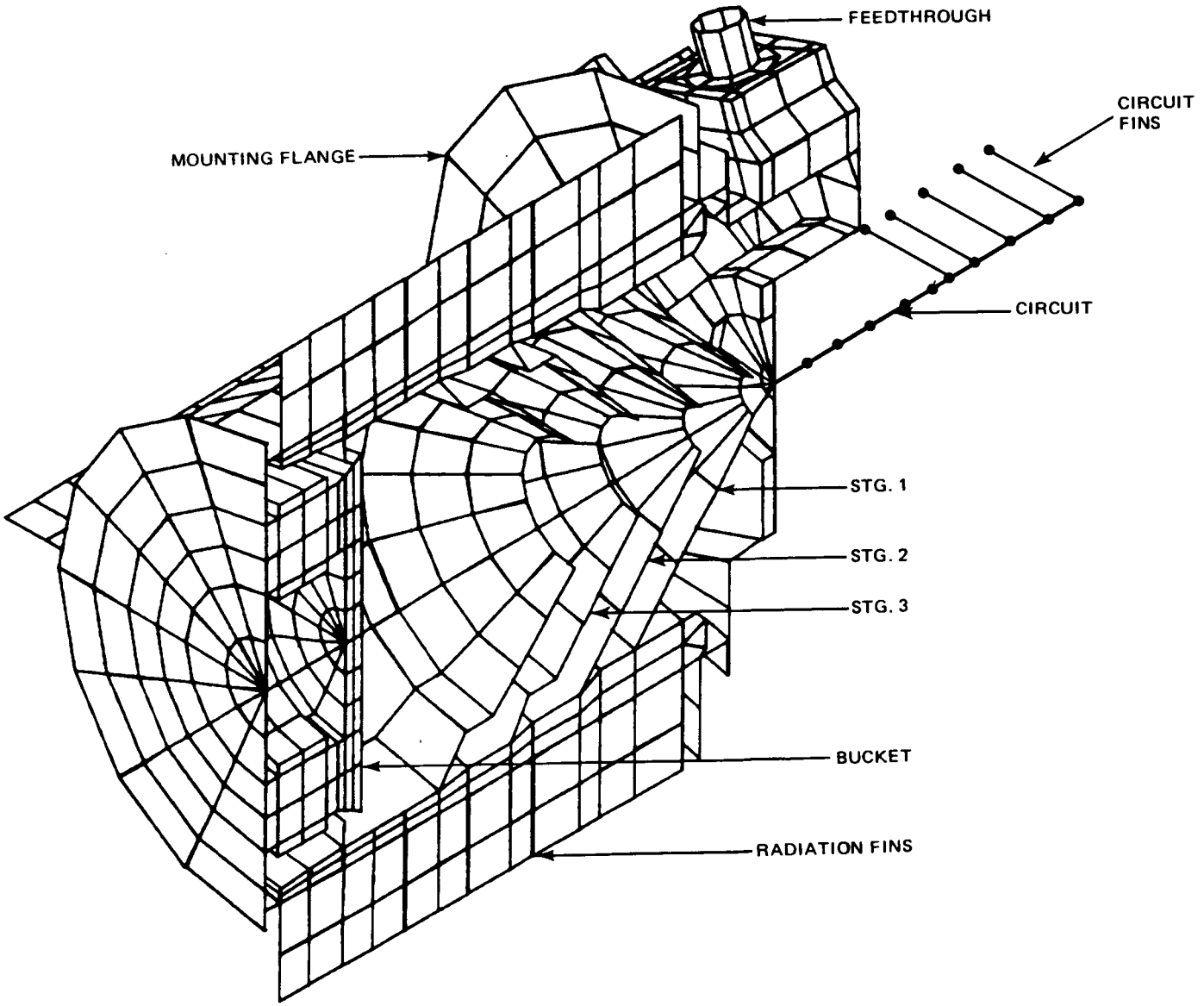

Figure A.2-2 ANSYS finite element model, inside view.

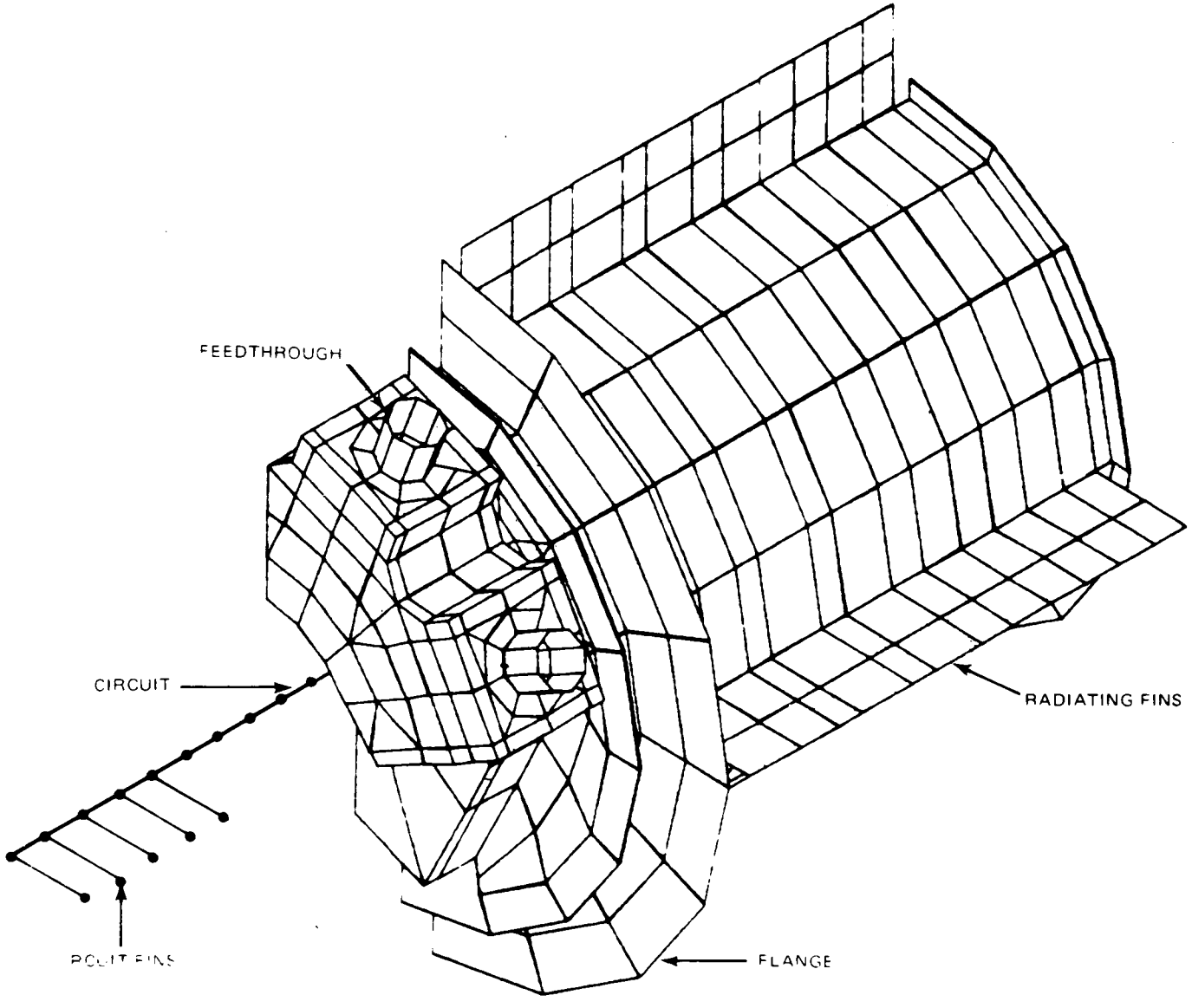

Figure A.2-3 ANSYS finite element model, outside view.

the output circuit area may also be potted with epoxy and/or adiprene, the only external heat transfer path modeled was that represented by the circuit fins. These short copper fins are brazed between pole pieces in the circuit and clamped to the baseplate.

The decision not to consider any potting was made primarily because the overall package/vacuum assembly interface was not completely defined at the time of this analysis. In any case, the circuit fins represent the major heat dissipation path, and omission of the potting is another conservative assumption.

The general temperature boundary conditions for this model are summarized in Figure A.2-4. They were obtained primarily from the previously mentioned 899H TWT thermal analysis. These temperatures were imposed on the baseplate side of the collector/baseplate interface as shown in Figure A.2-4. In the case of the circuit fins, the interface was modeled with elements representing the thermal resistance of the fin/clamp and fin/baseplate clamped joint. The thermal interface coefficient of 1.6 W/in^2-^oC was also obtained from the 899H analysis. This value is probably conservative because in previous analyses involving clamped interfaces with similar parameters, the coefficients determined were up to an order of magnitude greater. The collector flange to baseplate interface was modeled with elements representing eight Kovar bolts and Macor (insulating material) washers. The thermal interface coefficient between the washers, baseplate and flange was set at 0.8 W/in^2-^oC. Again, this value was obtained from the 899H analysis.

Radiation bulk temperature boundary conditions were set at -270C and 90^oC, respectively, for radiation to space and to the spacecraft. The space bulk temperature was initially set at -273^oC (absolute zero) but numerical problems occurred which forced a change to the slightly higher temperature. In order to check the effects of the modified boundary temperature, a solution at -250^oC was obtained. Comparison of these results indicated only very small differences, so the change from -273^oC to -270^oC would certainly be insignificant.

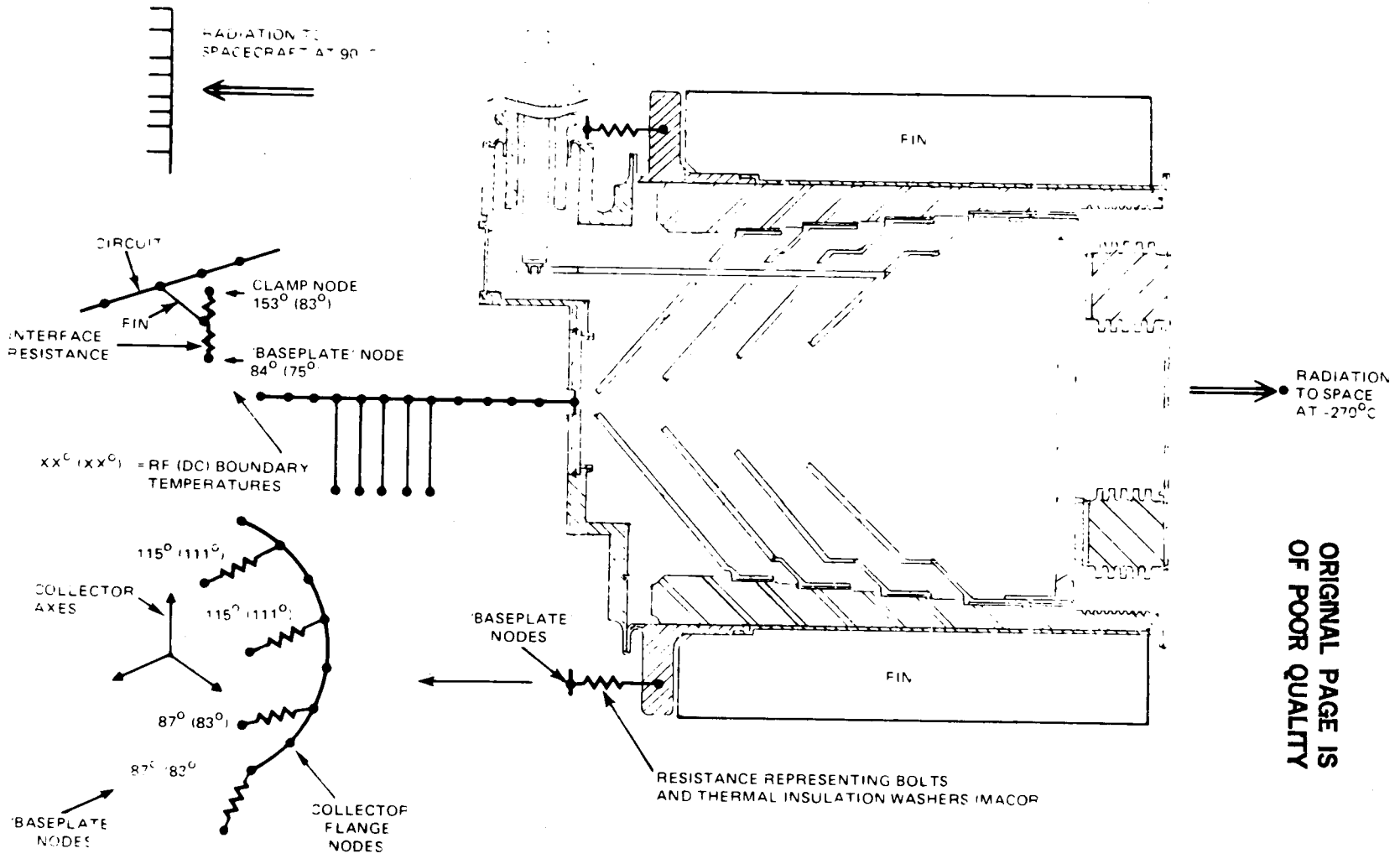

Figure A.2-4 Thermal boundary conditions, ^{o}C.

The thermal power dissipation levels obtained from the 961H Project Manager are depicted in Figures A.2-5 and A.2-6.

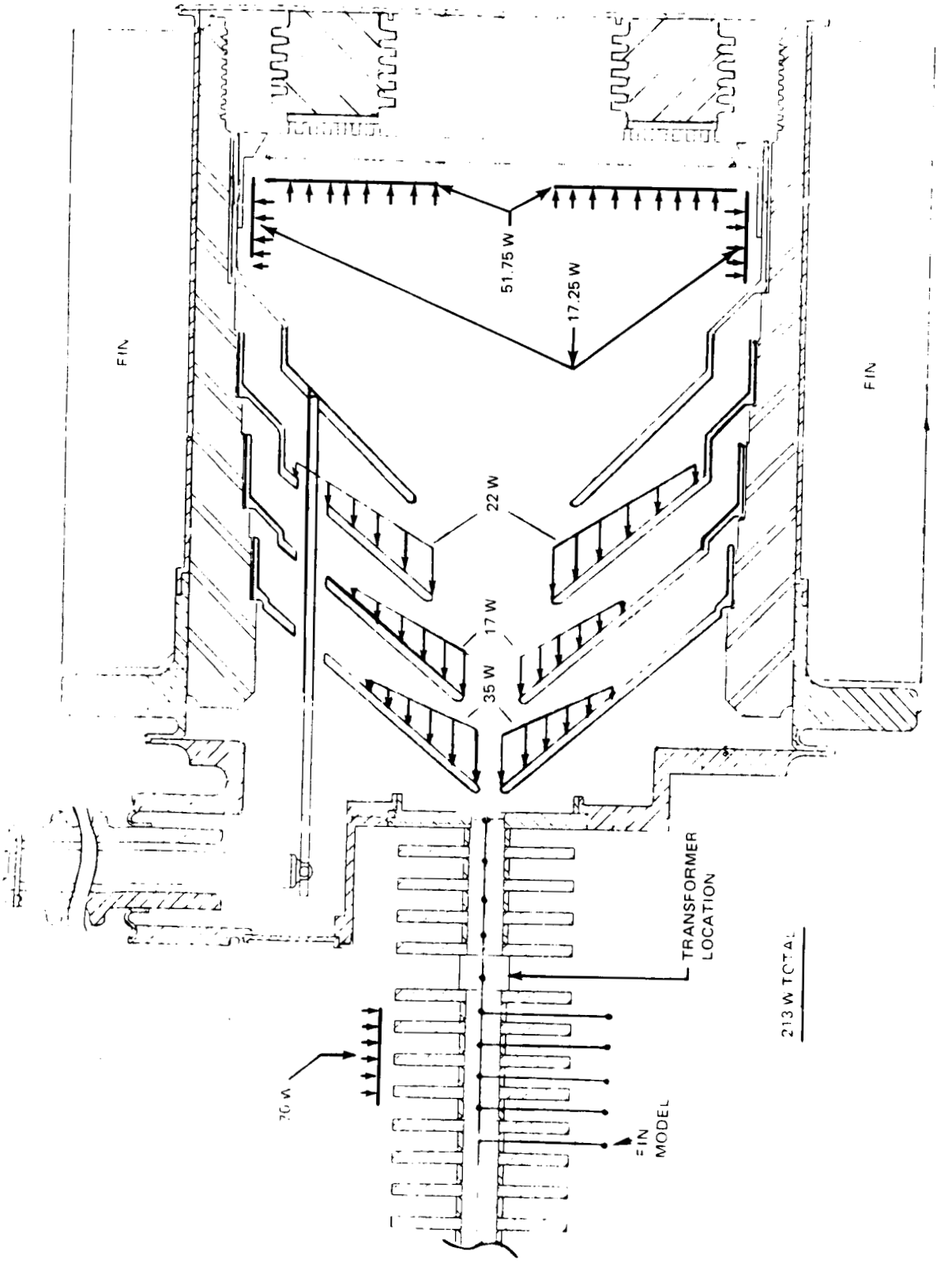

Figure A.2-5 RF power loading.

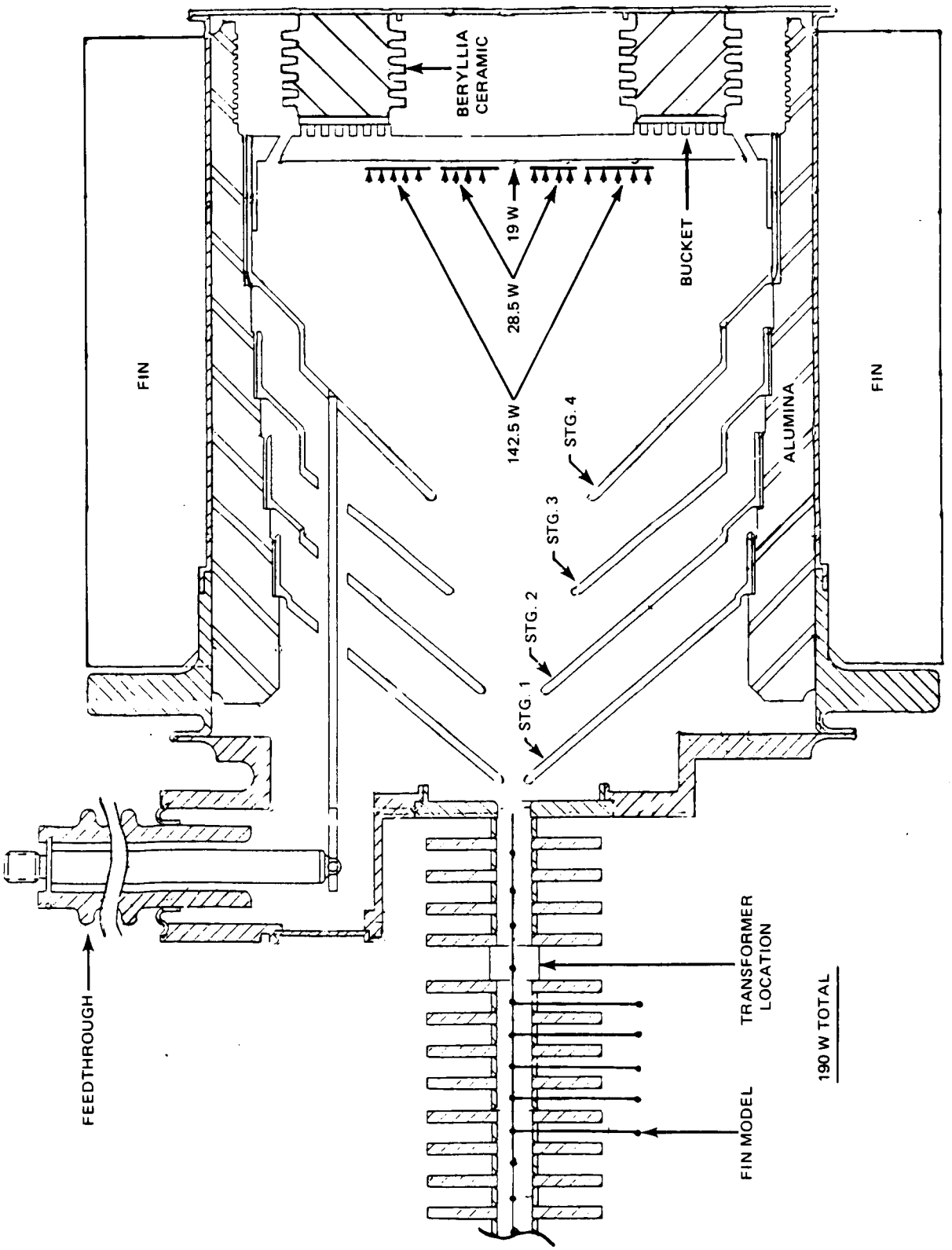

Figure A.2-6 DC power loading.

A.3 THERMAL RESULTS

Results for the RF and dc load cases are shown in Figures A.3-1 and A.3-2. The dc load case produced the maximum overall collector temperatures due to the concentrated power dissipation on the bucket. The maximum external temperatures were located on the rear closure plate, with a peak of 344°C occurring at the interface between the beryllia isolator and the plate.

The maximum output circuit temperature of 221°C occurred for the RF load case since there was no circuit power dissipation in the dc mode. This temperature cannot be associated with any particular component of the circuit as it is only an average value between the inner and outer surfaces of the circuit. The 221°C temperature is also a conservative (high) value due to the previously decribed conservative output circuit model.

Figure A.3-3 shows the resultant distribution of the RF and dc power loadings at the various thermal boundaries. The thermal power dissipations are of interest from two standpoints; the overall dissipation of total applied power and the dissipation of that portion of thermal power applied to the collector stages (internal collector power). For the latter case, of specific interest is the amount of internal collector power that is conducted and/or radiated back to the spacecraft. Overall breakdown of the thermal power dissipation for the RF and dc load cases is summaried in Table A.3-1.

The distribution of internal collector power in the dc mode is the same as that shown in the table since all of the dc power is applied internally to the collector bucket. In the RF mode, the total internal collector power can be

TABLE A.3-1

961H TOTAL THERMAL POWER DISSIPATION DISTRIBUTION

Quantity/ Load Case	Heat Radiated to Spacecraft	Heat Conducted to Spacecraft	Heat Radiated to Space
RF (213W)	18.6 W (8.7%)	84.6 W (39.7%)	109.8 W (51.6%)
DC (190W)	21.4 W (11.3%)	22.5 W (11.8%)	146.1 W (76.9%)

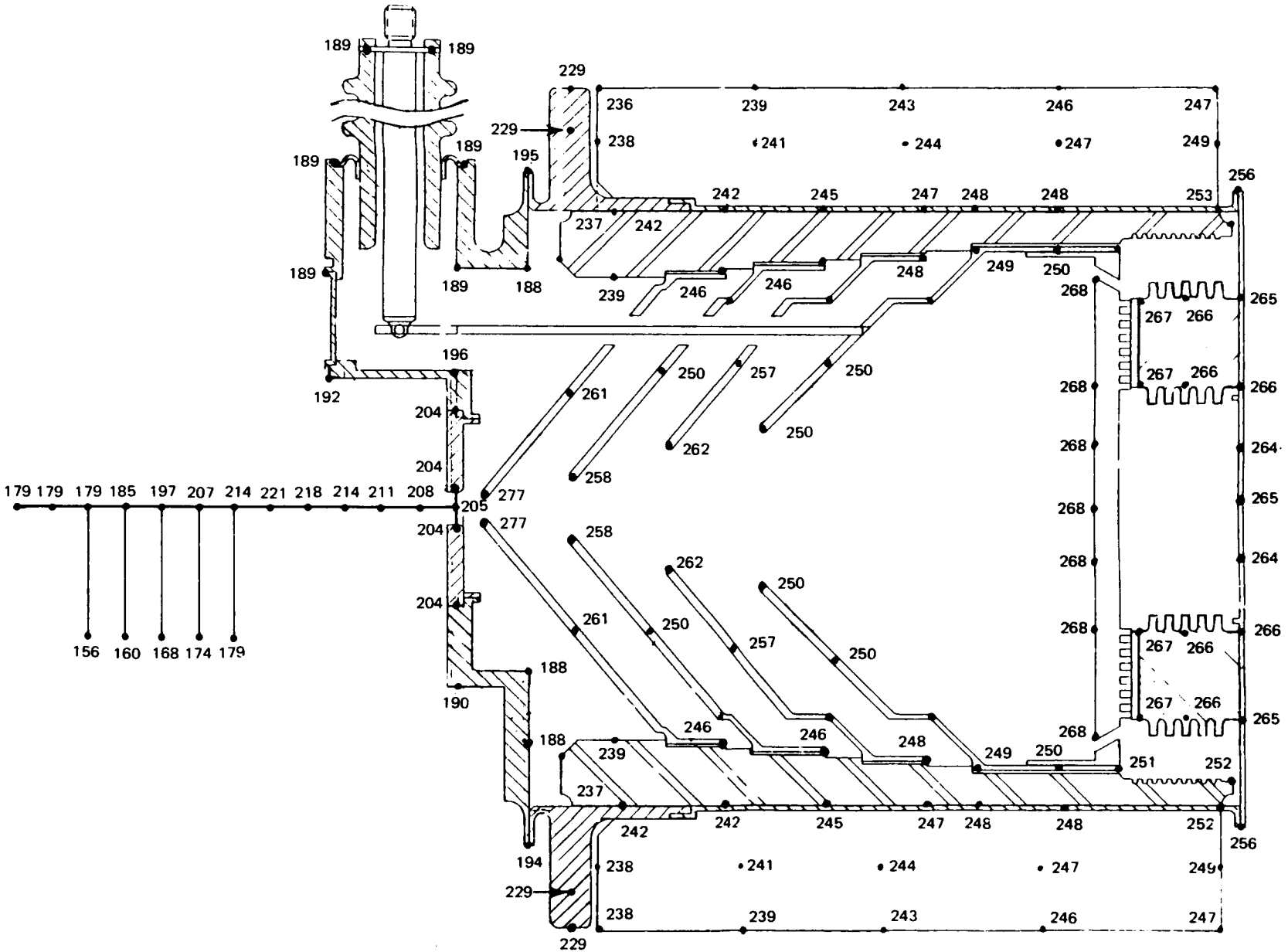

Figure A.3-1 RF temperature profile, ^{o}C.

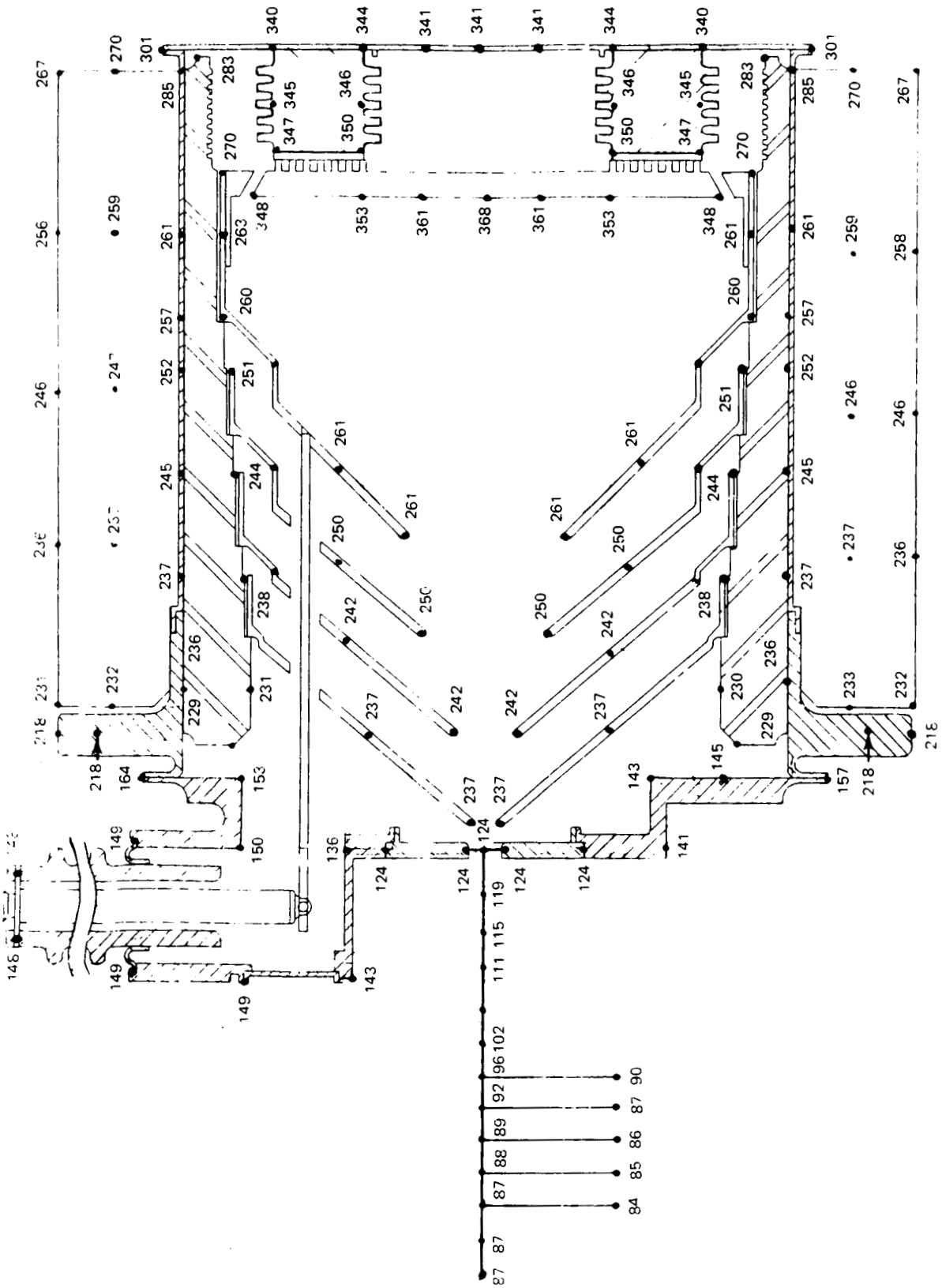

Figure A.3-2 DC temperature profile, °C.

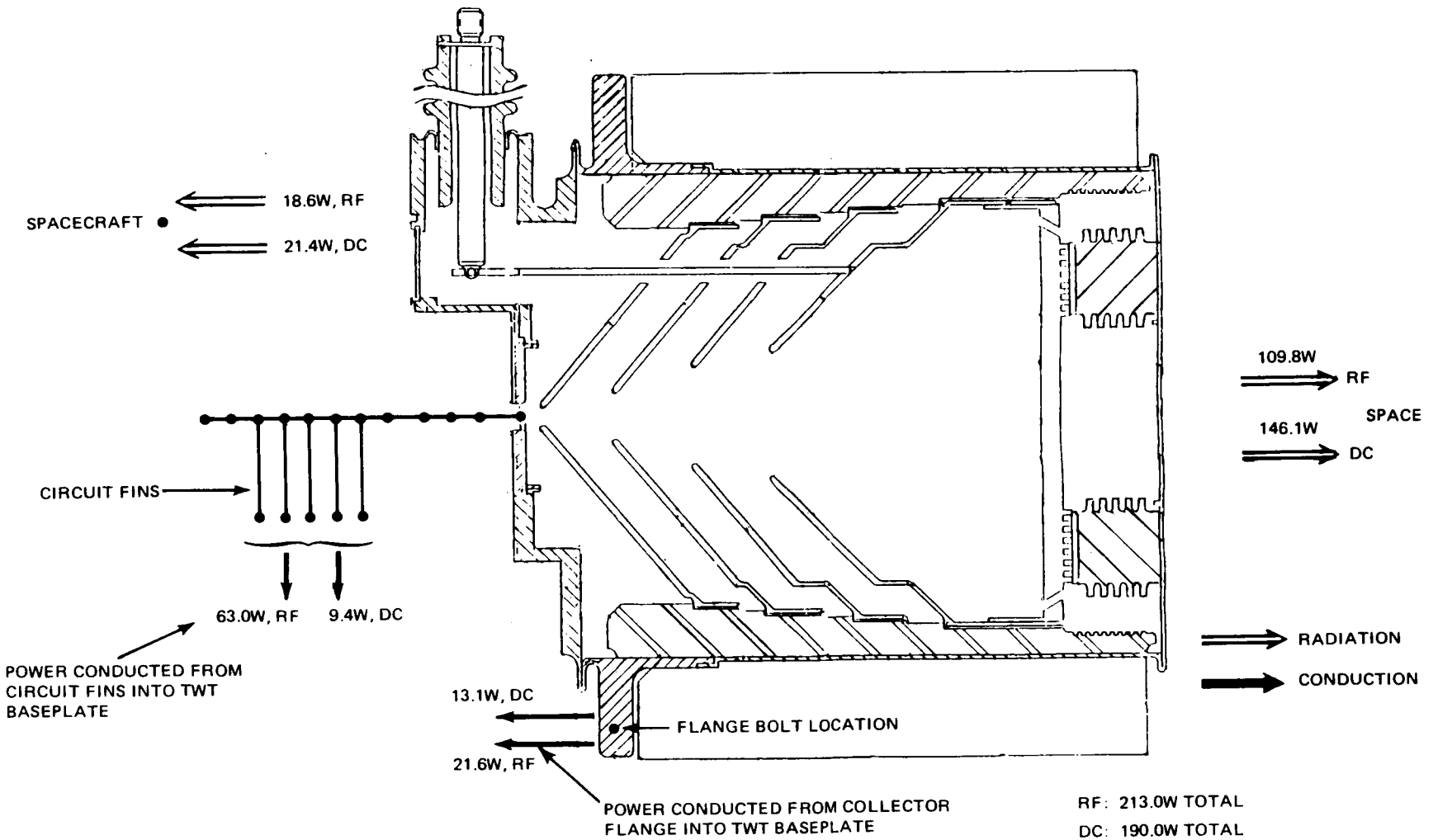

Figure A.3-3 Thermal power distributions at boundaries.

determined by subtracting from the toal amount of applied power that amount which is conducted through the circuit fins, i.e., 213.0 W - 63.0 W = 150.0 W. Thus, the small portion of applied output circuit power that is conducted through the circuit and collector face (10 percent) is treated as internal collector power for the purpose of this report. Of this 150 W, 21.6 W (14.4 percent) is conducted to the spacecraft through the flange and baseplate while 18.6 W (12.4 percent) is radiated to the spacecraft external surfaces. The remainder is radiated to space.

That only a small portion of the RF output circuit power is conducted through the faceplate is due to the relatively high resistance (thin section) thermal path at the collector face/body juncture. This was a deliberate design feature that also works well in the dc mode, as only 9.4 W or 5 percent of the internal dc mode applied power was conducted back into the output circuit.

A.4 CONCLUSION

An extensive thermal analysis of the 961H collector has been peformed. Results of the analysis indicated that all temperatures are well within acceptable limits. The analysis also proved the feasibility of using radiation heat transfer as the primary means of cooling the collector.

It was also shown that the current mechanical design of the collector minimizes the amount of heat transferred from the collector body into the output circuit. This design feature keeps the output circuit temperatures as low as possible and minimizes internal collector power backflow into the spacecraft.

Although a structural analysis was not performed, the general design of this collector appears to be adequate by virtue of its similarity to the 899H TWT collector. The 899H design has been proven by both test and analysis to be structurally sound. The fact that the 961H may be judged adequate by comparison is further substantiated by the fact that both collectors experience similar T values.

APPENDIX B
REFERENCES

1. G. Herrmann, "Optical Theory of Thermal Velocity Effects in Cylindrical Electron Beams," J. Appl. Phys., Vol. 29, p. 127 (1958).

2. C.C. Cutler and M.E. Hines, "Thermal Velocity Effects in Electron Guns," Proc. IRE, Vol. 43, p. 307 (1955).

3. H.K. Detweiler, "Characteristics of Magnetically Focused Large-Signal Traveling-Wave Amplifiers," RADC Technical Report TR-68-433, Contract No. AF 30 (602)-3569, October 1968.

4. H.K. Detweiler, "Calculation of Space-Charge Forces in the Analysis of Traveling-Wave Tubes," JPL Quarterly-Technical Review, Vol. 1, p. 106, April 1971.

5. W.B. Herrmannsfeldt, "Electron Trajectory Program," Stanford Linear Accelerator Center Report SLAC-166, September 1973.

6. J.B. Kennedy, I. Tammaru, and P.S. Wolcott, "Study of 42 and 85 GHz Coupled Cavity Traveling-Wave Tubes for Space Use," NASA Final Report CR-134670, Contract No. NAS 3-19701, June 1977.

7. P. Ramins and T.A. Fox, "90 to 93 Percent Efficient Collector for Operation of a Dual-Mode Traveling-Wave Tube in the Linear Region," IEEE Trans. Electron Devices, Vol. ED-26, p. 1662 (1979).

8. H.K. Kosmahl, "Modern Multistage Depressed Collectors - A Review," IEEE Proc., Vol. 70, November 1982.

NASA
National Aeronautics and Space Administration

Report Documentation Page

1. Report No.	2. Government Accession No.	3. Recipient's Catalog No.
CR182135		

4. Title and Subtitle
Development of a 75 Watt 60 GHz Traveling-Wave Tube for Intersatellite Communication

5. Report Date
September 1988

6. Performing Organization Code

7. Author(s)
A. L. Rousseau, I. Tammaru, and J. P. Vaszari

8. Performing Organization Report No.
W-10301

10. Work Unit No.
506-44-21

9. Performing Organization Name and Address
Hughes Aircraft Company
Electron Dynamics Division
3100 W. Lomita Blvd.
Torrance, CA 90509-2999

11. Contract or Grant No.
NAS3-23351

13. Type of Report and Period Covered
Contractor Report - Final

12. Sponsoring Agency Name and Address
Lewis Research Center

14. Sponsoring Agency Code

15. Supplementary Notes
Lewis Research Center Contract Manager, Vernon Heinen, Space Electronics Div.

16. Abstract

This program covers the initial design and development of a 75 watt, 60 GHz traveling-wave tube for intersatellite communications, to meet the requirements of NAS3-23351. The objective frequency band was 59 to 64 GHz, with a minimum tube gain of 35 dB. The objective overall efficiency at saturation was 40 percent.

The tube, designated the 961H, used a coupled-cavity interaction circuit with periodic permanent magnet beam focusing to minimize the weight. For efficiency enhancement, it incorporated a four-stage depressed collector capable of radiation cooling in space. The electron gun had a low-temperature (type-M) cathode and an isolated anode.

Two tubes were built and tested; one feasibility model with a single-stage collector and one experimental model that incorporated the multistage collector.

17. Key Words (Suggested by Author(s))		18. Distribution Statement
Traveling-Wave Tube (TWT)		Publicly Available
V-Band	Space TWT	
Coupled Cavity	Multi-stage	
High Efficiency	Collector	

19. Security Classif. (of this report)	20. Security Classif. (of this page)	21. No of pages	22. Price*
Unclassified	Unclassified	131	

NASA FORM 1626 OCT 86

*For sale by the National Technical Information Service, Springfield, Virginia 22161